Università
degli Studi
di Padova

Sede Amministrativa: UNIVERSITÀ DEGLI STUDI DI PADOVA
Dipartimento di Fisica e Astronomia "Galileo Galilei"

Scuola di dottorato di ricerca in Astronomia
Ciclo XXXIV

The chemical composition of very young open clusters

Coordinatore: Prof. Giovanni Carraro

Supervisore: Prof. Giovanni Carraro
Co-Supervisore: Dr. Valentina D'Orazi

Dottoranda: Martina Baratella

Valutatori esterni:
Dr. Tamara Mishenina
Prof. Chris Sneden

Abstract

Open clusters (OCs) are excellent tracers of the chemical properties and their evolution of the Galactic disc. These systems represent the concept of single stellar population well, that is, a group of coeval, (initially) chemically homogeneous stars. They cover a wide range in metallicity and age; crucially they are almost ubiquitous in the Galactic disc. Therefore, OCs allow us to investigate several aspects, such as e.g., stellar evolution and nucleosynthesis models, galactic chemical evolution, gradients, migration processes, and star-planet connections. However, at variance with intermediate-age and old OCs, for which a significant number of studies is now available, clusters younger than the Hyades (~600 Myr) have been mostly overlooked in terms of their chemical composition (with few exceptions). Previous investigations seem to indicate an anomalous behaviour of the youngest systems (open clusters, associations, and moving groups), and three main observational issues have been identified. (i) There is a lack of super-solar composition systems in the solar neighbourhood, at odds with predictions of the Galactic evolution models. (ii) Young and relatively cool ($T_{\rm eff} < 5400$ K) stars exhibit overabundance of different atomic species, derived either from ionised and/or from high-excitation potential lines. Finally, (iii) we detected the (in-)famous barium (Ba) puzzle: extreme, unexpectedly high Ba enhancements are found at young ages, with values up to +0.7 dex at 30 Myr. Regarding the behaviour of the other s-process elements like yttrium (Y), zirconium (Zr), lanthanum (La), and cerium (Ce), there is general disagreement in the literature. Several authors claim that they follow the same trend as Ba, while others find solar abundances at all ages. Lately, different studies agree that stellar activity (stronger at young ages than for OCs older than 600 Myr) can alter the formation of moderate and strong spectral lines (and/or it can influence the structure of the stellar atmosphere). As a consequence, lines forming in the upper layers of the photosphere are systematically stronger in young stars than in old ones (assuming the stars to have similar fundamental parameters).

Our working hypothesis is that the local anaemia, the overabundance of ionised atoms, and the Ba puzzle could be due to limitations of the standard abundance analysis when applied to young, active stars. The goal of my Thesis is to expand our understanding of this topic from an observational point of view. During the 3 years of my Ph.D., I have analysed high-resolution, high S/N spectra of solar-type stars observed by the Gaia-ESO survey and by the Global Architecture of Planetary Systems -GAPS- consortium and belonging to several young stellar systems (open clusters, moving groups and associations). My investigation points to the need to revising the spectroscopic techniques when applied to very young stars.

While waiting for a theoretical explanation, we can overcome these issues by adopting new approaches or with strategic choices of the spectral lines to use. In particular, I developed a new spectroscopic method that is based mostly on the use of Ti lines: with this, the Galactic metallicity distribution in the solar surroundings is restored and we don't have to call for complex, ad hoc explanations. The correlation of the stellar parameter with activity is also explored, as well as the dependency of overabundances. Finally, the Ba puzzle seems to be far more complex than we expected. Both form a spectral and a nucleosynthesis point of view, a solution is still missing. This Thesis deals with the spectroscopic issues of the abundance analysis of very young stars.

Riassunto

Gli ammassi aperti (OC) sono eccellenti traccianti delle proprietà chimiche e della loro evoluzione del disco Galattico. Questi sistemi rappresentano bene il concetto di popolazione stellare singola, cioè un gruppo di stelle coeve, (inizialmente) chimicamente omogenee. Essi coprono un'ampia gamma di metallicità e di età; soprattutto sono quasi onnipresenti nel disco Galattico. Pertanto, gli OC ci permettono di indagare diversi aspetti, come ad esempio l'evoluzione stellare e i modelli di nucleosintesi, l'evoluzione chimica galattica, i gradienti, i processi di migrazione e le connessioni stella-pianeta. Tuttavia, in contrasto con gli ammassi aperti di età intermedia e vecchia, per i quali è ora disponibile un numero significativo di studi, gli ammassi più giovani delle Iadi (600 Myr) sono stati per lo più trascurati in termini di composizione chimica (con poche eccezioni). Le indagini precedenti sembrano indicare un comportamento anomalo dei sistemi più giovani (ammassi aperti, associazioni e gruppi), e sono stati identificati tre principali problemi osservativi. (i) C'è una mancanza di sistemi di metallicità super-solare nel vicinato solare, in contrasto con le previsioni dei modelli di evoluzione Galattica. (ii) Le stelle giovani e relativamente fredde (sotto 5400 K) mostrano una sovrabbondanza di diverse specie atomiche, derivate da righe spettrali di ionizzate e/o ad alta eccitazione. Infine, (iii) abbiamo rilevato il (in-)famoso puzzle del bario (Ba): estremi, inaspettatamente alti potenziamenti di Ba si trovano a giovani età, con valori fino a +0.7 dex a 30 Myr. Per quanto riguarda il comportamento degli altri elementi del processo s come ittrio (Y), zirconio (Zr), lantanio (La) e cerio (Ce), c'è un disaccordo generale in letteratura. Diversi autori sostengono che seguono la stessa tendenza del Ba, mentre altri trovano abbondanze solari a tutte le età. Ultimamente, diversi studi concordano sul fatto che l'attività stellare (più forte nelle giovani età che per gli OC più vecchi di 600 Myr) può alterare la formazione di righe spettrali moderate e forti (e/o può influenzare la struttura dell'atmosfera stellare). Di conseguenza, le righe che si formano negli strati superiori della fotosfera sono sistematicamente più forti nelle stelle giovani che in quelle vecchie (assumendo che le stelle abbiano parametri fondamentali simili).

La nostra ipotesi di lavoro è che l'anemia locale, la sovrabbondanza di atomi ionizzati e l'enigma del Ba potrebbero essere dovuti alle limitazioni dell'analisi di abbondanza

standard quando applicata a stelle giovani e attive. L’obiettivo della mia Tesi è di espandere la nostra comprensione di questo argomento da un punto di vista osservativo. Durante i 3 anni del mio dottorato, ho analizzato spettri ad alta risoluzione e alto S/N di stelle di tipo solare osservate dalla Gaia-ESO survey e dal consorzio Global Architecture of Planetary Systems -GAPS- e appartenenti a diversi sistemi stellari giovani (ammassi aperti, gruppi e associazioni). La mia indagine indica la necessità di rivedere le tecniche spettroscopiche applicate alle stelle molto giovani.

In attesa di una spiegazione teorica, possiamo superare questi problemi adottando nuovi approcci o con scelte strategiche delle righe spettrali da utilizzare. Ho sviluppato un nuovo metodo spettroscopico che si basa principalmente sull’uso di righe del Ti: con questo, la distribuzione della metallicità galattica nell’ambiente solare viene ripristinata e non dobbiamo ricorrere a complesse spiegazioni ad hoc. Viene anche esplorata la correlazione del parametro stellare con l’attività, così come la dipendenza delle sovrabbondanze. Infine, il puzzle del Ba sembra essere molto più complesso di quanto ci aspettassimo. Sia da un punto di vista spettrale che di nucleosintesi, manca ancora una soluzione. Questa Tesi si occupa delle questioni spettroscopiche dell’analisi dell’abbondanza di stelle molto giovani.

Publication list

Here below you find a complete list of the papers I published during my PhD Thesis, as first author and as co-author. This Thesis work is based mainly on those pucblished as first author.

First author

- **Baratella, M.**; D'Orazi, V.; Sheminova, V.; Spina, L.; Carraro, G.; Gratton, R. and 28 more, *"The Gaia-ESO Survey: A new approach to chemically characterising young open clusters II. Abundances of the neutron-capture elements Cu, Sr, Y, Zr, Ba, La, and Ce"*, 2021, A&A, 653, A67
  DOI: 10.1051/0004-6361/202141069

- **Baratella, M.**; D'Orazi, V.; Biazzo, K.; Desidera, S.; Gratton, R.; Benatti, S. and 17 more, *"The GAPS Programme at TNG: XXV- Stellar atmospheric parameters and chemical composition through GIARPS optical and near-infrared spectra"*, 2020, A&A, 640, A123
  DOI: 10.1051/0004-6361/202038511

- **Baratella, M.**; D'Orazi, V.; Carraro, G. and 33 more, *"The Gaia-ESO Survey: a new approach to chemically characterising young open clusters. I. Stellar parameters, and iron-peak, α-, and proton-capture elements"*, 2020, A&A, 634, A34
  DOI: 10.1051/0004-6361/201937055

- **Baratella, M.**; Carraro, G.; D'Orazi, V. & Semenko, E., *"Radial Velocity and Chemical Composition of Evolved Stars in the Open Clusters NGC 6940 and Tombaugh 5"*, 2018, The Astronomical Journal, vol. 156, issue 5, article id. 244
  DOI: 10.3847/1538-3881/aae57e

Co-author

- Magrini, L. ; Smiljanic, R. ; Franciosini, E. ; Pasquini, L. ; Randich, S. ; Casali, G.; Viscasillas Vazquez, C.; Bragaglia, A. ; Spina, L. ; Biazzo, K. ; Tautvaivsiene, G. ; Masseron, T. ; Van der Swaelmen, M. ; Pancino, E. ; Jimenez-Esteban, F. ; Guiglion, G. ; Martell, S. ; Bensby, T. ; D'Orazi, V. ; **Baratella, M.** et al., *"The Gaia-ESO survey: Lithium abundances in open cluster Red Clump stars"*, 2021, A&A, in press
  DOI: arxiv:2108.11677

- Magrini, L.; Lagarde, N.; Charbonnel, C.; Franciosini, E.; Randich, S.; Smiljanic, R.; Casali, G.; Viscasillas Vazquez, C.; Spina, L.; Biazzo, K.; Pasquini, L.; Bragaglia, A.; Van der Swaelmen, M.; Tautvaisiene, G.; Inno, L.; Sanna, N.; Prisinzano, L.; Degl'Innocenti, S.; Prada Moroni, P.; Roccatagliata, V.; Tognelli, E.; Monaco, L.; de Laverny, P.; Delgado-Mena, E.; **Baratella, M.** and et al. from GES consortium, *"The Gaia-ESO survey: Mixing processes in low-mass stars traced by lithium abundance in cluster and field stars"*, May 2021, eprint arXiv:2105.04866
  Bibcode: 2021arXiv210504866M

- Spina, L.; Ting, Y. -S.; De Silva, G. M.; Frankel, N.; Sharma, S.; Cantat-Gaudin, T.; Joyce, M.; Stello, D.; Karakas, A. I.; Asplund, M. B.; Nordlander, T.; Casagrande, L.; D'Orazi, V.; Casey, A. R.; Cottrell, P.; Tepper-García, T.; **Baratella, M.** and et al. from GALAH consortium, *"The GALAH survey: tracing the Galactic disc with open clusters"*, 2021, MNRAS, 503, pp.3279-3296
  DOI: 10.1093/mnras/stab471

- Carleo, I.; Desidera, S.; Nardiello, D.; Malavolta, L.; Lanza, A. F.; Livingston, J.; Locci, D.; Marzari, F.; Messina, S.; Turrini, D.; **Baratella, M.** and et al. from GAPS consortium, *"The GAPS Programme at TNG. XXVIII. A pair of hot-Neptunes orbiting the young star TOI-942"*, 2021, A&A, 645, A71
  DOI: 10.1051/0004-6361/202039042

- Maryeva, O.; Bicz, K.; Xia, C.; **Baratella, M.**; Čechvala, P.; Vida, K., *"Flare stars in nearby Galactic open clusters based on TESS data"*
  Bibcode: 2021yCatp025005101M

- Maldonado, J.; Micela, G.; **Baratella, M.** and 27 more, *"HADES RV programme with HARPS-N at TNG. XII. The abundance signature of M dwarf stars with planets"*, 2020, A&A, 644, A68
DOI: 10.1051/0004-6361/202039478

- Gutiérrez Albarrán, M. L.; Montes, D.; Gómez Garrido, M.; Tabernero, H. M.; González Hernández, J. I.; Marfil, E.; Frasca, A.; Lanzafame, A. C.; Klutsch, A.; Franciosini, E.; Randich, S.; Smiljanic, R.; Korn, A. J.; Gilmore, G.; Alfaro, E. J.; **Baratella, M.** and more, *"The Gaia-ESO Survey: Calibrating the lithium-age relation with open clusters and associations. I. Cluster age range and initial membership selections"*, 2020, A&A, 643, A71
DOI: 10.1051/0004-6361/202037620

- Casali, G.; Spina, L.; Magrini, L.; Karakas, A. I.; Kobayashi, C.; Casey, A. R.; Feltzing, S.; Van der Swaelmen, M.; Tsantaki, M.; Jofré, P.; Bragaglia, A.; Feuillet, D.; Bensby, T.; Biazzo, K.; Gonneau, A.; Tautvaišienė, G.; **Baratella, M.** and more, *"The Gaia-ESO survey: the non-universality of the age-chemical-clocks-metallicity relations in the Galactic disc"*, 2020, A&A, 639, A127
DOI: 10.1051/0004-6361/202038055

- Spina, L.; Nordlander, T.; Casey, A. R.v Bedell, M.; D'Orazi, V.; Meléndez, J.; Karakas, A. I.; Desidera, S.; **Baratella, M.**, Yana Galarza, J. J.; Casali, G.; *"How Magnetic Activity Alters What We Learn from Stellar Spectra"*, 2020, The Astrophysical Journal, Volume 895, Issue 1, id.52
DOI: 10.3847/1538-4357/ab8bd7

Conference posters

- Biazzo, K.; **Baratella, M.** ; Benatti, S. ; Carleo, I.; Damasso, M. ; Desidera, S.; Mancini, L. ; GAPS-YO team@INAF, *"Searching and characterizing young planets with the GAPS2 project"*, The 20.5th Cambridge Workshop on Cool Stars, Stellar Systems, and the Sun (CS20.5), virtually anywhere, March 2-4, 2021. Online at `http://coolstars20.cfa.harvard.edu/cs20half`, id.89
DOI: 10.5281/zenodo.4562832

Contents

List of Figures

List of Tables

CHAPTER 1

Scientific background

Besides the natural curiosity to know what stars are made of, the determination of the stellar parameters and chemical composition is important in several astrophysical fields.

First, stars are the main site for nucleosynthesis to take place: the creation of chemical elements through nuclear reactions occurs in stellar cores, where sufficiently high temperatures can be reached (see e.g., the seminal paper by Burbidge et al. 1957). Initially, all stars are mainly composed by hydrogen (H) and helium (He), and then during the entire evolution, elements from lithium (Li) to lead (Pb) are produced through a complex chain of nuclear reactions. Essentially, all the elements in the Periodic Table that we know are produced in stars, which are the best laboratories to test the nucleosynthesis theories.

At the end of the stellar evolution, the elements are released into the interstellar medium (ISM) through a variety of processes, depending on the initial stellar mass. The iron-peak elements (such as iron Fe, manganese Mn, chromium Cr, and nickel Ni) are mainly released at the end of the evolution of low- and intermediate-mass stars ($M \lesssim 10\,\mathrm{M}_\odot$) through type-Ia supernovae (SN Ia) events on long timescales ($\sim$1-2 Gyr). The α-elements (like silicon Si, calcium Ca, oxygen O, and titanium, Ti) are instead produced by massive stars ($M \gtrsim 10\,\mathrm{M}_\odot$) with type-II supernovae (SN II) events on rapid timescales of the order of $\sim$ few Myr. On the other hand, the neutron-capture elements -beyond the iron-peak (like e.g., barium Ba, lanthanum La, cerium Ce, and Pb)- are produced in different environments: low- and intermediate mass asymptotic giant branch (AGB) stars are the main source of the slow (s) neutron-capture process (Käppeler et al. 2011), whereas explosive environments are deemed to be the site for the rapid (r) process (Cowan et al. 2021). From the gas subsequently enriched in heavy elements, a new generation of stars can form, which carries the imprint of the parental molecular cloud, i.e., of the previous generation of stars. Thus, we can investigate formation and evolution mechanisms of our Galaxy by deriving detailed chemical composition, age and kinematic of single stars.

In exoplanetary science, the determination of the chemical composition of planet-host stars plays an important role as to probe the main observational correlations between substellar companions and their host stars. This includes the giant planet-metallicity correlation (Adibekyan 2019; Turrini et al. 2021), according to which giant planets are mainly formed around more metal-rich stars. Trends of different abundance ratios ([X/Fe][1]) with condensation temperature (T_C) have been observed over the years: all of these are important in particular for the planet formation theories (core accretion and the recent tidal downsizing models *vs*. gravitational instability, Pollack et al. 1996; Helled et al. 2014; Nayakshin 2017).

The most powerful tool that allows us to gather detailed information on the chemical composition of stellar systems is (high-resolution) spectroscopy. From stellar spectra, a variety of additional information can be also determined, such as e.g., atmospheric parameters (effective temperature, $T_{\rm eff}$, and surface gravity, $\log g$.) By including atomic physics and model atmospheres, we then derive the abundance of each element. Thanks to the advent of large spectroscopic surveys, we are obtaining a huge amount of high quality (high resolution and high signal-to-noise ratio, S/N) stellar spectra. We are now able to study the different components of our Galaxy with extreme precision and homogeneity on industrial scale (see e.g., Jofré et al. 2019, for a complete review). However, in the last decade several authors have pointed out important limitations of the classical spectroscopic analysis, especially when applied to very young stars (that is younger than the Hyades, age ~ 600 Myr). The times are ripe to tackle these issues that cannot be overlooked in this new era of big data.

In my Ph.D. thesis three main issues concerning the chemical composition of young stars will be address. The current state of the art for these topics is presented in this introductory Chapter that is organised as follows: in Sec. 1.1 I briefly discuss the (apparent) slight metal-poor nature of the young stellar systems in the solar vicinity. The second issues of young stars, i.e. the anomalous overabundances of solar-type stars, are discussed in Sec. 1.2. In Sec. 1.3 I present the curious time evolution of the *s*-process elements.

1.1 The young open clusters and their metallicity distribution

Among the most efficient objects used to probe the chemical properties of galaxies and their time evolution and/or to test the nucleosynthesis theories, star clusters indeed play a key role. By definition, a star cluster consists of stars that were born from the same molecular cloud at (roughly) the same time. Thus, they share age, distance, kinematics and the initial chemical composition (some peculiar species such as e.g., Li, and C might

---

[1] Abundance scales: $\log(X)_\star = \log(N_X/N_H) + 12$; $[X/H] = \log(X)_\star - \log(X)_\odot$; [X/Fe]=[X/H]-[Fe/H]

be altered during the stellar evolution). The determination of the chemical composition of clusters of different ages and locations in our Galaxy is then crucial for reconstructing its formation and evolution.

In this thesis, the focus will be on open clusters (OCs), as they offer a unique opportunity to study the chemical patterns of the Galactic thin disc (see e.g., Friel 1995, Jacobson et al. 2016, Reddy et al. 2016, Magrini et al. 2017). Some of the most predominant features of OCs are: i) the large range of metallicity covered, between -0.5 and $+0.5$ dex (Netopil et al. 2016; Donor et al. 2020); ii) ages from few Myr to several Gyr, which is determined with a precision by far better than field stars (Bossini et al. 2019); iii) they are ubiquitous in the disc. An extremely detailed census of roughly 1900 OCs observed all over the Galactic disc is given by Cantat-Gaudin et al. (2020). At variance with the old globular clusters (see e.g., Gratton et al. 2019, for a recent review), OCs represent well the concept of single stellar populations: high levels of chemical homogeneity are observed in OCs, reaching values of the abundance scatter of the order of 0.02-0.03 dex (Bovy 2016; Casamiquela et al. 2020).

In recent years, the number of studies focused on OCs and their characterisation has enormously increased thanks to several large multi-object spectroscopic surveys (such as, e.g., the *Gaia*-ESO public spectroscopic survey, Gilmore et al. 2012 and Randich et al. 2013; the Apache Point Observatory Galactic Evolution Experiment, APOGEE, Cunha et al. 2016; Donor et al. 2020; the Open Clusters Chemical Abundances from Spanish Observatories, OCCASO, Casamiquela et al. 2016, 2019; GALactic Archaelogy with HERMES, GALAH, De Silva et al. 2015; Spina et al. 2021). In addition, there are other smaller collaborations, like Stellar Population Astrophysics (SPA, Origlia et al. 2019) that are producing interesting results and completing the large survey results. In this framework, OCs covering a large range of ages from few Myr to several Gyr, are observed with multi-object spectrographs, so many targets per cluster are observed simultaneously. All of them are then analysed within the consortium in a highly homogeneous way. Hence, the spectroscopic surveys data offer the opportunity to derive the metallicity and the abundances of a significant number of targets. However, the majority of the studies about the chemical analysis of OCs is focused on intermediate-age and old clusters ($t > 300$ Myr) (for example, Magrini et al. 2009; Carrera & Pancino 2011; Heiter et al. 2014; Carraro et al. 2016; Baratella et al. 2018; Reddy & Lambert 2019; Casamiquela et al. 2020; Casali et al. 2020a, to cite a few). Less attention has been payed to the chemical composition of young OCs (YOCs), in particular those with ages $t \lesssim 200$ Myr, and star forming regions (SFRs), with ages $t \lesssim 10$ Myr, with few exceptions, such as James et al. (2006); Santos et al. (2008); Biazzo et al. (2011a,b); Spina et al. (2014a,b, 2017).

There has been a growing body of evidence in the last 15 years that no metal-rich

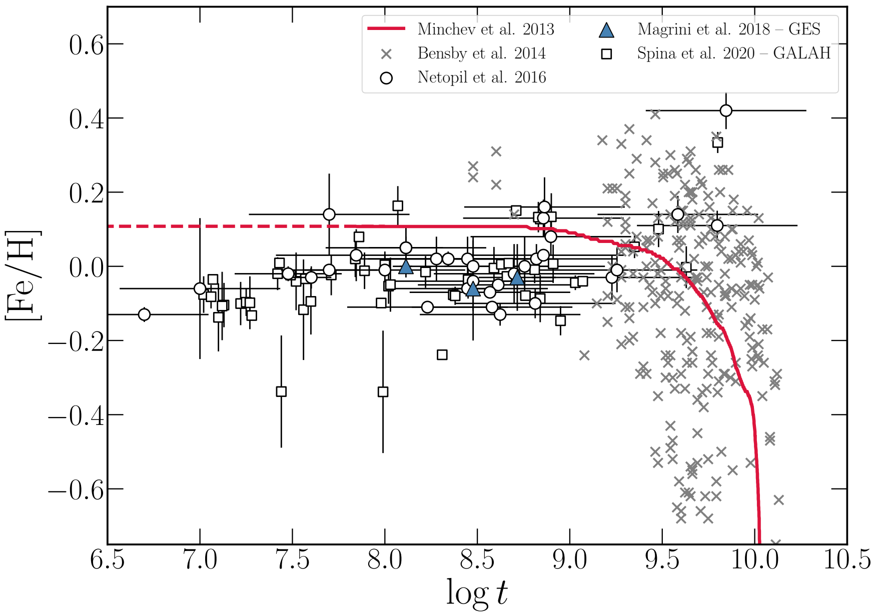

Figure 1.1: Age-metallicity distribution in the solar neighbourhood for the cluster sample of Netopil et al. (2016) (empty circles) for which high-resolution metallicity determinations are available; for field stars taken from Bensby et al. (2014) (grey crosses); for the *Gaia*-ESO clusters analysed in Magrini et al. (2018) (filled triangles); for the GALAH clusters taken from Spina et al. (2020). The red line represents the model by Minchev et al. (2013) for 7.5< $R_{\rm Gal}$ < 9 kpc.

YOCs, SFRs, young moving groups and associations exist in the solar neighbourhood (7.5 < R_{GC} < 9 kpc), at odds with the predictions of the Galactic chemical evolution (GCE) models (Minchev et al. 2013). James et al. (2006) analysed a sample of solar-type T-Tauri stars in 3 SFRs (Lupus, Chamaeleon I & II, and Corona Australis, $t \lesssim 10$ Myr): the authors found the mean metallicities (in particular [Fe/H]) to be equal to −0.10 ± 0.04, −0.11 ± 0.14 (individual values from −0.26 to +0.12) and −0.04 ± 0.05, respectively. In a following paper by the same group, Santos et al. (2008), Rho-Ophiuchus, Taurus and Orion Nebula Cloud (ONC) were added to the list of analysed SFRs: again, sligthly subsolar [Fe/H] values were found (averages of −0.08 ± 0.12, −0.05 ± 0.11 and −0.13 ± 0.06). Similar results have been reported by other independent studies: for the ONC, D'Orazi et al. (2009b) reported a metallicity of −0.01 ± 0.04 dex; D'Orazi et al. (2011) found that the Taurus-Auriga association has a mean [Fe/H] of −0.01 ± 0.05 dex. The ONC was re-analysed by Biazzo et al. (2011a), who found a metallicity of −0.11 ± 0.08 dex: in the same work, the authors analysed also the OB1b group in the Orion complex that has [Fe/H] of −0.05 ± 0.05 dex. Biazzo et al. (2011b) analysed K-type stars in the 25 Orionis and λ Orionis young clusters (ages less than 10 Myr) and reported an average metallicity of −0.05 ± 0.05 and 0.01 ± 0.01. The Chamaeleon I SFR was re-analysed by Spina et al. (2014a) within the *Gaia*-ESO survey: the authors found a mean metallicity of -0.08 ± 0.04 dex. Similarly, Spina et al. (2014b) reported an average metallicity for Gamma Velorum pre-main sequence cluster of -0.06 ± 0.02 dex. Recently, Spina et al. (2017) analysed YOCs and SFRs spanning an age range between 1 and 80 Myr, with a mean metallicity of -0.06 ± 0.02 for the SFRs and -0.02 ± 0.02 for the YOCs. And so on, several other authors reached the same conclusions.

Indeed, it seems that all the young populations within 500 pc from the Sun have a slightly lower metal content with respect to the Sun, being on average 15% lower than the solar metallicity (Spina et al. 2020). This is clear when looking at the metallicity distribution of OCs with $7.5 < R_{\rm Gal} < 9$ kpc (taken from Netopil et al. (2016), Magrini et al. (2018) and Spina et al. (2020)), as represented in Figure 1.1. In this Figure the grey crosses are the field stars from Bensby et al. (2014). All the values of [Fe/H] till very recent epochs falls below the expectations of the GCE model (Minchev et al. 2013) (red line), which predicts an enrichment of 0.1-0.15 dex in the last 4-5 Gyr (the model does not extend to ages lower than 60 Myr, but we expect it keeps a flat, continuous trend, which is represented by the dashed line in Fig.1.1). Such young stars did not have enough time to disperse in the Galactic disc through radial migration. Thus, their metallicity is representative of the chemical composition of the ISM at their birthplace. A possible explanation for the local anaemia could be considering a complex combination of star formation, gas inflows and outflows, or a different composition of the parental molecular cloud (Spina et al. 2017).

It is important to address whether the local young stellar systems have [Fe/H] slightly lower than the Sun, also for the implications in exoplanetary science. It is well established that giants planets are found mostly around metal-rich stars (Santos et al. 2004). At least the 25% of stars with detected Jupiter-like planets have $[\mathrm{Fe/H}] \geq +0.3$ dex (see e.g., Fischer & Valenti 2005; Adibekyan 2019; Turrini et al. 2021). This suggests that giant planets has mainly formed through core-accretion mechanism (Pollack et al. 1996; Alibert et al. 2004) or tidal downsizing (Nayakshin 2017), as these models predict the observed correlation giant planet-metallicity relation. On the contrary, models based on gravitational disc instabilities do not predict a dependency from the metallicty of the host star. Therefore, the lack of metal enriched population would imply that in these systems it is less favorable to find giant planets, or that they have formed through disc instabilities.

1.2 The over-ionisation and over-excitation effects in young stars

Another issue emerges from the standard spectroscopic analysis of young stars, in particular the young cool ($T_{\rm eff} < 5400$ K) dwarf stars. There has been mounting evidence that in

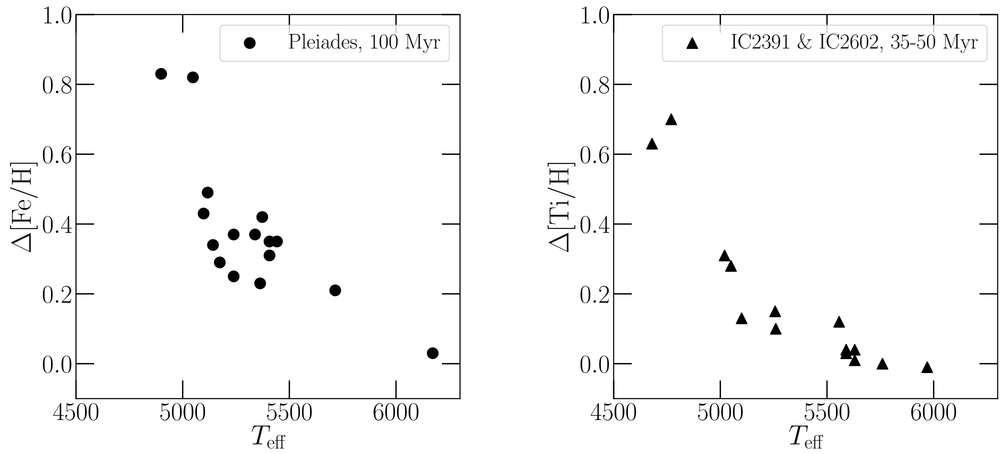

Figure 1.2: Examples of the ionisation balance problem. The differences between ionised and neutral Fe (left, taken from Schuler et al. 2010) and Ti (right, taken from D'Orazi et al. 2009a) are plotted as a function of $T_{\rm eff}$.

these stars abundances of neutral atoms are systematically lower than the abundances of ionised atoms of the same species. As a consequence, the ionisation equilibrium, which is imposed to derive $\log g$, is not satisfied under LTE assumption.

Schuler et al. (2003) analysed a set of GK type dwarfs observed in M 34 cluster (age $\sim 200-250$ Myr) and reported that Fe I is systematically under-abundant with respect to Fe II in the coolest stars ($T_{\rm eff} < 5400$ K), labelling this as non-LTE over-ionisation. Similar results have been reached by other authors as well by Yong et al. (2004), who analysed a sample of FGK stars in the Hyades cluster (age 600 Myr). The authors found that the difference between Fe II and Fe I is +0.3 dex at $T_{\rm eff}$ = 4700 K, but reaches +1.2 dex at 4000 K. The authors proposed that the over-ionisation of Fe could be mainly due to more intense UV radiation field that increases the population of the ionised levels causing the derived overabundances, since non-LTE corrections alone cannot explain such discrepancies. This is true if we consider the relatively young age of the Hyades and other previous studies (see e.g., Reid et al. 1995) that confirmed that the Hyades stars are chromospherically active. Although in Yong et al. (2004) no direct measurement of the activity levels of the stars have been measured, this explanation seems promising.

As it can be seen in Figure 1.2, the difference between ionised and neutral Fe (left panel) for a sample of dwarf stars observed in the Pleiades (age $\sim$ 100 Myr) is +0.8 dex at $T_{\rm eff}$ =5000 K (Schuler et al. 2010). A similar behaviour is also found by D'Orazi et al. (2009a) for Ti in dwarf stars observed in IC 2391 and IC 2602 clusters (50 and 30 Myr, respectively) even though to a smaller extent. Clearly, if $\log g$ is derived spectroscopically, such differences will have a great impact on it: once the $T_{\rm eff}$ is fixed according to the excitation equilibrium, the log g must be decreased to satisfy the ionisation equilibrium, reaching often un-physical values. Tsantaki et al. (2013) argued that beside the limitations to model the atmosphere of cool stars in LTE, the presence of undetected blends in the Fe II lines that becomes important in stars at low temperatures cannot be excluded. Similar conclusions have been reached also by Aleo et al. (2017), and later corroborated by Takeda & Honda (2020). Interestingly, Tsantaki et al. (2019) showed that the effect might be more dramatic for Fe lines than for Ti, and that the log g derived by using Ti lines is more reliable.

Similarly, overabundances of some elements derived from high-excitation potential energy (χ) lines have been reported over the years. King et al. (2000) analysed dwarf stars in the Pleiades (100 Myr) and NGC 2264, and found that the O abundance (derived from O I triplet at 777nm with χ = 9.15 eV) is +0.9 and +0.4 dex respectively. Such enhancements do not reflect the real O abundance of these clusters, as they are expected to have solar metallicity. The overabundance of O was observed also in the Ursa-Mayor (UMa, $\sim$ 500 Myr) moving group by King & Schuler (2005) and in the Hyades ($\sim$ 600 Myr, Schuler et al. 2006, for example. Later, overabundances of other elements, such as Si, C, Ca, Ni have been reported, with all of them derived with lines with large χ, both in OCs and also in cool dwarf field stars (see e.g., Ramírez et al. 2007; Schuler et al. 2010, 2015; Delgado Mena et al. 2021).

There is general consensus that these overabundances are not real and they are generally due to undetected blends, even if other explanations (e.g., the link with stellar activity) seems promising. Given the importance to determine accurately the individual abundances of stars (for instance, the C/O ratios give clues on planet formation mechanisms and migration process across the protoplanetary disc), we should find other means to obtain more reliable measurements, while waiting to find a theoretical explanation.

1.3 The Galactic evolution of the *s*-process elements

Although OCs exhibit solar-scaled abundances as far as light and α elements are concerned (Casamiquela et al. 2020; Spina et al. 2021), they present peculiar chemical composition in those elements produced via the slow (s) neutron-capture process (hereafter the s-process elements; see Käppeler et al. 2011, and references therein).

D'Orazi et al. (2009a) derived Ba abundances for a sample of dwarfs and giants observed in 20 OCs spanning a range of ages from 30 Myr to 8 Gyr, a range of Galactocentric distances from 7 to 22 kpc and metallicities from −0.3 to +0.4 dex. As it can be seen in Figure 1.3, for the first time it was shown a sharp increase of [Ba/Fe] at decreasing ages. Quantitatively, this anti-correlation with age can be reproduced with GCE models up to 1

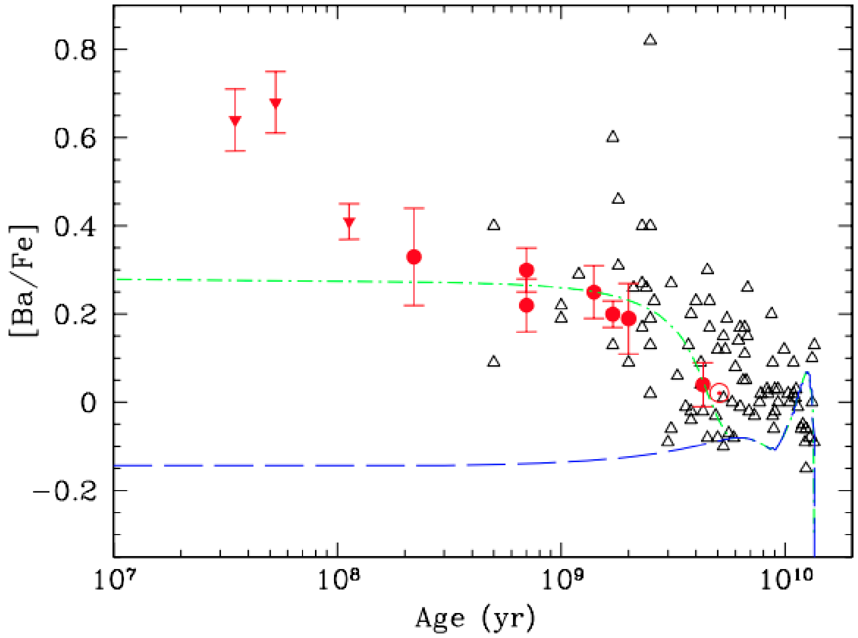

Figure 1.3: Average [Ba/Fe] as a function of age, taken from D'Orazi et al. (2009a). The comparison between the results obtained in OCs (filled symbols) and field stars (empty symbols) is shown, together with the prediction of GCE models with standard stellar yields (blue line) and modified yields (green line).

Gyr (Travaglio et al. 1999; Busso et al. 2001). However, when moving to young ages (below 500 Myr, and especially at 50 Myr) the overabundances cannot be reproduced either by standard models (blue line) or by ad hoc models with enhanced stellar yields (green line). In the following years, different authors began investigating on this topic, extending the analysis to the other *s*-process elements in young clusters, associations, and field stars.

Maiorca et al. (2011) investigated the behaviour of yttrium Y, zirconium Zr, lanthanum La, and cerium Ce in order to look for over-solar abundances (similar to Ba). An enhancement in the Ba content should also be accompanied by similar trends in La and Ce. According to nucleosynthesis theoretical models, since these three elements belong to the second-peak of the s-process reactions they should be produced together. Enhancements of Y and Zr, which belong to the first-peak, could be possible as well, although to a different extent (because they depends on details of masses and reactions involved). The authors analysed a sample of dwarf stars observed in 8 OCs (ages from 110 Myr to 4.3 Gyr) and a sample of giants in 11 OCs (ages from 180 Myr to 8.4 Gyr). Surprisingly, they confirmed that all the *s*-process elements have a steep growth between 1.5 and 0.5 Gyr, and are consistent, if not lower, with solar values at ages larger than 1.5 Gyr. However, the number of clusters for which La and Zr have been measured is small, thus making the correlation not statistically meaningful. This is not the case for Ba, for which they confirmed the trend with time. Later, Maiorca et al. (2012) found that the *s*-elements abundances can be reproduced, within the uncertainties, by suitably fixing the parameters controlling the neutron source in low-mass stars, without invoking other ingredients. However, as shown in their Figure 4, those models still fail at explaining the higher values observed at very young age (around 50 Myr), especially for Ba.

The Ba overabundance is not exclusive of OCs, but it is found in all the youngest components of the Milky Way. D'Orazi et al. (2012) investigated the distribution of *s*-process element abundances in 3 local young associations (AB Doradus - $\sim$ 100 Myr; Carina-Near - $\sim$ 200 Myr; UMa - $\sim$ 500 Myr). They found that Ba is over-abundant by +0.2 dex on average with respect to the solar composition, while Y, Zr, La and Ce are solar at all ages, at variance with what was previously reported by Maiorca et al. (2011). De Silva et al. (2013) confirmed Ba to be over-abundant (+0.5 dex) in the Argus association (age similar to IC 2391, $\sim$ 50 Myr).

Different authors agree on the Ba overabundance, but there is no general consensus regarding the behaviour of the other *s*-process elements. Several possible explanations have been investigated trying to shed light on the true nature of the Ba enhancements: is it due to local enhancement? Is it due to chromospheric activity? Is it a manifestation of NLTE? Mishenina et al. (2013) analysed in detail the behaviour of Y and Ba in intermediate age and old OCs ($t > 200$ Myr) and found that Y abundances exhibit a slight trend, from −0.2 to +0.2 dex, as a function of the increasing age, while for Ba they reported a significantly larger trend, with a large spread of measurements at a given age. However, while the moderate trend of Y might be explained with enrichment of the ISM due to AGB low mass ($M < 1.5\,\mathrm{M}_{\odot}$) stars, this is not the case for Ba. The authors took into account NLTE effects in their analysis, so this explanation was excluded from the possible solutions to the Ba puzzle.

Jacobson & Friel (2013) investigated the efficiency of the *s*-process relative to the *r*-process enrichment in OCs, deriving abundance for Zr, Ba, La and Eu (a proxy typically used to trace the *r*-process). They found that the [s/r] ratios are enhanced at young ages (even though the sample of OCs they analysed is limited to 700 Myr). Instead, no clear correlation is found with metallicity, suggesting that age play a significant role in the anomalous abundances.

Still, the problem to reconcile the GCE models with the observations remains: apparently, the *s*- or the *r*- processes alone (or even a combination of both) are not able to predict the enhancements of Ba. In a further attempt to understand this, Mishenina et al. (2015) investigated the possibility that another process can contribute to the observed Ba overabundances. Indeed, they found that to reproduce the large [Ba/Fe] values at young ages (and to reproduce the large spread of measurements) without involving La, the intermediate neutron-capture process (*i*-process) should be invoked (Cowan & Rose 1977).

However, there are large uncertainties on what is the main site of activation of this process.

Given the difficulty of reproducing the Ba enhancements disentangled from La without invoking exotic processes, a possible solution can be found in alterations of the standard model atmospheres or line formation, investigating the link with age, or better the stellar activity. This is what has been explored in Reddy & Lambert (2015) and Reddy & Lambert (2017), since the most commonly used Ba II line (at 5853.7 Å) is near the flat part of the curve of growth. Thus, it is very sensitive to the adopted microturbulence velocity parameter. This Ba II line is used to derive the abundance because it is the strong (but not as saturated as the Ba II resonance line at 4554 Å), it is not heavily blended and it has small NLTE corrections. Reddy & Lambert (2015) demonstrated that by changing the ξ value by 0.5 $\mathrm{km\,s^{-1}}$, the abundance of Ba is lowered by 0.3 dex, with La abundance remaining nearly constant (since La lines are significantly weaker than Ba lines). So, apparently, the anomalously large values of [Ba/Fe] reflect the limitations of the currently adopted model atmospheres and line formation theories when applied to very young stars. This idea was enforced by Reddy & Lambert (2017) who showed a correlation between larger [Ba/Fe] and stronger activity levels, even though both measurements were not synchronous.

The Ba abundance has been derived for other pre-main sequence clusters, in an attempt to increase the number of observations and finally solve the Ba puzzle. D'Orazi et al. (2017) analysed a sample of FGK dwarfs in young cluster with ages less than 50 Myr; Biazzo et al. (2017) reported over-solar [Ba/Fe] for the Lupus T association; Magrini et al. (2018) exploited the *Gaia*-ESO internal data release (iDR) 5 results homogeneously determined for a large sample of clusters, however, limited to $t > 100$ Myr. However, each group analysed different stars with different techniques contributing to the complexity of the Ba puzzle. A direct comparison of the measurements and further investigations may be difficult and for this reason, a new study where abundances are derived in an homogeneous way for a large sample of stars is needed to shed light on this unsolved mystery.

1.4 Aims of the thesis

It is clear from the previous Sections that the standard spectroscopic analysis of young stars exhibits some limitations. What is/are the main mechanism/s behind all these remains unknown. However, the key to understand this seems to be the young age of the stars.

Globally speaking, young stars are characterised by intense levels of activity (Skumanich 1972). Stellar activity manifests as star-spots, faculae, pladges, intense photospheric magnetic fields, hot chromosphere emission and magnetic flux tubes (Wright et al. 2011; Shkolnik & Barman 2014; Vidotto et al. 2014; West et al. 2015; Davenport et al. 2019). The effects of each are shown in stellar spectra, for example, as emissions in the cores of the strongest lines (H_α) or the flux variability of the Ca II H&K lines. Over the years, the effects of the activity on the formation of spectral lines have been investigated. Flores et al. (2016) studied the active star HD 45184 and found that some Fe II lines forming in the upper layers of the photosphere show a modulation over the stellar activity cycle. Interestingly, Reddy & Lambert (2017) found that Fe I lines are systematically stronger in a young solar analog than in the quiet Sun, especially those forming at small optical depth. More recently, Yana Galarza et al. (2019) reported modulation of the stellar parameters of star HD 59967, in particular $T_{\rm eff}$ and ξ, with the largest variations observed at the maximum of the activity cycle. Spina et al. (2020) confirmed this scenario for a larger sample of solar twins (211 in total).

Even though these studies are mainly focused on stars with ages over $\sim$ 400 Myr, the situation might be more complex and dramatic at 50 Myr, with stronger effects on the line formations and/or on the structure of the atmosphere itself. From this evidence, we introduce our working hypothesis that the local anaemia of YOCs/SFRs, the overabundances of ionised atoms, and the Ba puzzle, could be the results of the limitations of the standard abundance analysis when applied to very young (active) systems.

My Ph.D. thesis is focused on the analysis of FGK dwarf stars observed in the YOCs IC 2391, IC 2602, IC 4665, NGC 2516 and NGC 2547 and the SFR NGC 2264. These clusters have been observed and already analysed by the *Gaia*-ESO consortium. In addition, I was also involved in the Global Architecture of Planetary Systems (GAPS) program (Covino et al. 2013), in particular in the Young Object (YO) working package as a member of the stellar characterisation team. Within the program, I have analysed several young and intermediate-age stars belonging to young associations (e.g., Ursa Major, Hercules-Lyrae and Coma Berenices) monitored to search for radial velocity exoplanets. I analysed high resolutions spectra obtained with UVES spectrograph (*Gaia*-ESO) and with HARPS-N (GAPS-YO), coupled with GIANO-B in the near infrared.

The main goals of my thesis are to investigate the issues related to the young stars and eventually to answer the following still open questions (from an observational point of view):

- Is the metal-poor nature of nearby YOCs and SFRs intrinsic or related to analysis techniques? What are the implications for the search of Jupiter-like planets in these systems, in light of the giant planet-metallicity relation?

- What is the reason for the overabundance of ionised atoms?

- How can we explain the observed overabundance of Ba? Do the other s-process elements behave like Ba?

In Chapter 2 I address the first issue presented above by analysing the clusters selected from the *Gaia*-ESO archive. I present a new spectroscopic approach developed to obtain more reliable atmospheric parameters. All the results obtained have been published in Baratella et al. (2020b).

In Chapter 3 several targets observed by GAPS-YO group are analysed and the main strategy of the stellar characterisation team is presented. Moreover, I investigate the connection of the overabundances of ionised atoms with stellar activity. The results have been published in Baratella et al. (2020a).

In Chapter 4 the time evolution of different neutron-capture process elements (in particular Cu and the *s*-elements Sr, Y, Zr, Ba, La and Ce) is explored. The behaviour of spectral lines and the possible explanations in the Galactic framework (with GCE models) are extensively investigated. The results have been published in Baratella et al. (2021).

Finally, the main conclusions of this Ph.D. thesis are drawn in Chapter 5, where the future perspectives are also presented.

CHAPTER 2

The *Gaia*-ESO Survey: a new approach to chemically characterising young open clusters

I. Stellar parameters, and iron-peak, α-, and proton-capture elements

Based on:
Baratella M., D'Orazi V., Carraro G., et al., 2020, A&A, Volume 634, id.A34, 15 pp

Open clusters are recognised as excellent tracers of Galactic thin-disc properties. At variance with intermediate-age and old open clusters, for which a significant number of studies is now available, clusters younger than $\lesssim$ 150 Myr have been mostly overlooked in terms of their chemical composition until recently (with few exceptions). On the other hand, previous investigations seem to indicate an anomalous behaviour of young clusters, which includes (but is not limited to) a slightly sub-solar iron (Fe) abundances of systems in the solar vicinity. The hypothesis that these chemical peculiarities are related to abundance analysis technique seems promising and it is explored in this Chapter. I present a new determination of the atmospheric parameters for 23 dwarf stars observed by the Gaia-ESO survey in five young open clusters (IC 2391, IC 2602, IC 4665, NGC 2516 and NGC 2547, τ <150 Myr) and one star-forming region (NGC 2264). The new method I propose is based on titanium (Ti) lines to derive the spectroscopic surface gravity, and most importantly, the microturbulence parameter. A combination of Ti and Fe lines is used to obtain effective temperatures. The abundances of iron-peak, α- and proton capture elements (Fe, Ti, Na, Mg, Al, Si, Ca, Cr and Ni). My findings are in fair agreement with Gaia-ESO iDR5 results for effective temperatures and surface gravities, but suggest that for very young stars, the microturbulence parameter is over-estimated when Fe lines are employed. This affects the derived chemical composition and causes the metal content of *very young clusters to be under-estimated. The considered clusters display a metallicity [Fe/H] between +0.04±0.01 and +0.12±0.02; they are not more metal poor than the Sun. Although based on a relatively small sample size, this explorative study suggests that we may not need to call for ad hoc explanations to reconcile the chemical composition of young open clusters with Galactic chemical evolution models.*

2.1 Introduction

As already mentioned in Chapter 1, somewhat at odds with the predictions of Galactic chemical evolution models, several authors found that no YOCs and SFRs with over-solar metallicities exist within 500 pc from the Sun (e.g., James et al. 2006; Santos et al. 2008; D'Orazi et al. 2011; Biazzo et al. 2011a,b; Spina et al. 2017). The presence of these systems might be explained with a complex combination of star formation, gas inflows and outflows, radial migration or different composition of the parent molecular cloud (Spina et al. 2017). The lack of young, metal-enriched stellar populations might also imply that these systems do not present favorable conditions for hosting giant planets (because of the well established correlation between the frequency of gaseous giant planets and the metallicity of their host stars; see the recent review by Adibekyan 2019 and reference therein).

However, there are reasons to believe that the sub-solar metallicity of young stars is not intrinsic (real), but mostly related to analytical/theoretical issues. In fact, young stars have higher levels of activity, which manifest themselves both at chromospheric and at photospheric level (Folsom et al. 2016). The active layers/regions can alter the formation of spectral lines at a particular optical depth, which can impact the derived stellar parameters and abundances.

This has been recently demonstrated by Reddy & Lambert (2017), who have shown a possible correlation between Fe I abundance and their optical depth of formation (taken from Gurtovenko & Sheminova 2015). These authors found that in a young and active star, those lines forming in the upper layers of the photosphere provide larger abundances than those forming in deeper layers, when compared to a similar, but old and quiet, star. This observed trend could affect the derivation of the stellar parameters when using Fe lines in the *standard* spectroscopic analysis. Typically, the standard analysis consists in measuring the EWs of Fe lines (that are the most numerous spectral lines in a stellar spectrum) and by imposing simultaneously the excitation and the ionisation equilibrium, the $T_{\rm eff}$ and $\log g$ are determined, respectively (in the so-called equivalent width method). In addition to these, the microturbulence velocity (ξ) parameter is derived: this is a free, fictitious parameter introduced in 1D analysis to account for small-scale motions of matter in the photosphere that act as Doppler shifts in addition to the thermal and damping broadening. This parameter affects mostly saturated lines: as a consequence of these small-scale motions, the absorbers might be red-shifted or blue-shifted with respect to the central (at rest) wavelength, and therefore absorb light in the wings of the spectral line. The result is that the total light absorbed in the line is increased, and consequently the empirical curve-of-growth will be different than the theoretical. Micorturbulence velocity accounts for this discrepancy. Weaker lines are almost independent on this parameter, as they are more sensitive to the number of absorbers: so a change of ξ does not alter the line profile, at variance with strong lines that are insensitive to the number of absorbers, but they change at varying ξ. Then ξ is computed by forcing weak and strong lines to have the same abundance.

However, if strong lines (typically forming in the upper photospheric layers) yield anomalously larger abundances than weaker lines (as demonstrated in Reddy & Lambert 2017), the ξ parameter needs to be increased in order to remove the slope between individual abundances and EWs. For instance, in James et al. (2006) and Santos et al. (2008) the derived values of ξ are most probably extremely large (up to $\sim 2.5\,\mathrm{km\,s^{-1}}$), along with substantial star-to-star variation (apparently unrelated to the other stellar parameters). A similar pattern is also seen in (Viana Almeida et al. 2009), who analysed stars in 11 young associations, and found ξ values up to $\sim 2.6\,\mathrm{km\,s^{-1}}$ (which are typical values of a giant stars; Gray 2005).

These large values of ξ have two main effects. On one hand, the synthetic profile computed with such ξ fails at reproducing the observed spectral lines. In Figure 2.1 an example of the synthesis (red line) of different Fe I lines of a young star (black dot-dashed line) observed in IC 2391 ($t \sim 50$ Myr) is shown. According to the *standard* spectroscopic analysis, the derived stellar parameters are: $T_{\mathrm{eff}} = 5215 \pm 100\,\mathrm{K}$, $\log g = 4.35 \pm 0.1$ dex and $\xi = 1.75 \pm 0.15\,\mathrm{km\,s^{-1}}$ (the rotational velocity is $v \sin i = 9.88\,\mathrm{km\,s^{-1}}$). The synthetic profile obtained with this anomalous value of ξ (at this T_{eff} we would expect a value of $\sim 1.0\,\mathrm{km\,s^{-1}}$ or lower) does not reproduce the observed line profile. On the other hand, an overestimation of this parameter leads to an under-estimation of the abundances, in particular [Fe/H] and with the various abundance ratios [X/Fe] that re-scale accordingly. Then, the question arises whether the lack of metal-enriched young stars near the Sun is genuine or alternatively a consequence of the overestimated ξ.

In the following, a new spectroscopic approach to characterise and perform chemical analysis of young stars is presented. I analyse *Gaia*-ESO Survey iDR5 spectra of 23 stars observed in five YOCs plus one SFR. The data-set is described in Section 2.2, together

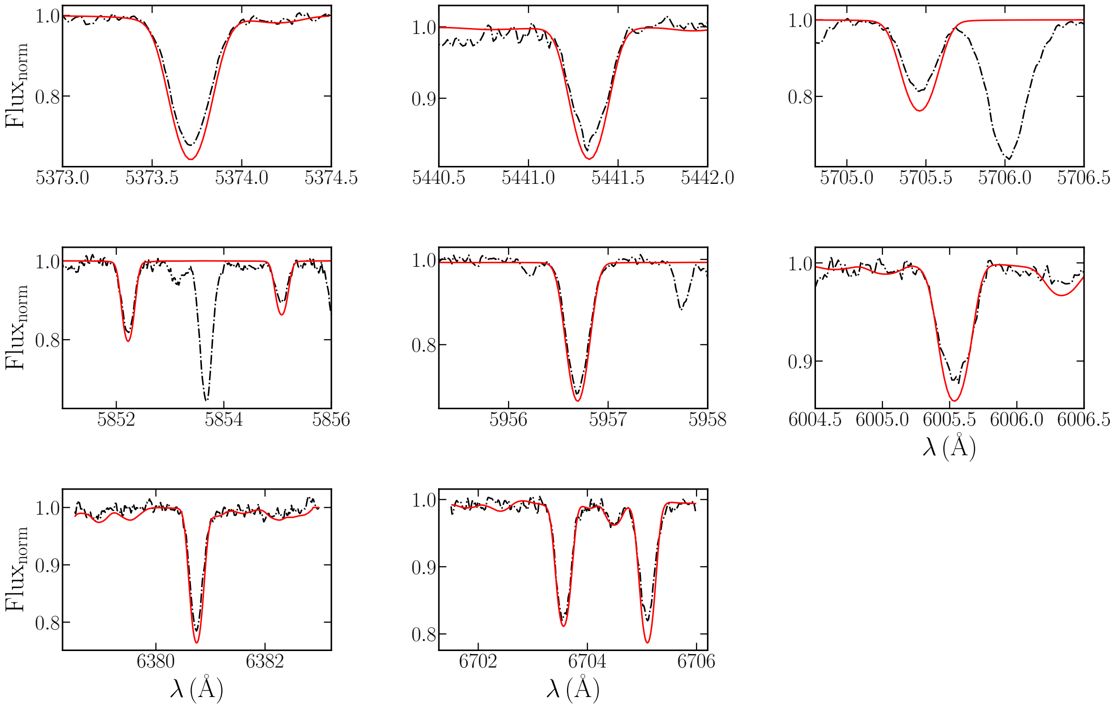

Figure 2.1: Examples of the synthesis of several Fe I lines of star 08365498−5308342 (IC 2391, $t \sim 50$ Myr, $v \sin i = 9.88$ km s^{-1} as the recommended value given in the *Gaia*-ESO iDR5) for which the observed profile is not fitted when we adopt the ξ value obtained from the Fe lines ($T_{\rm eff}$ =5215±100 K, log g =4.35±0.1 dex, ξ = 1.75 ± 0.15 km s^{-1}; red line).

Table 2.1: Basic information of the SFR and YOCs investigated in this work.

Cluster	RA (J2000)	Dec (J2000)	Age* (Myr)	Distance (pc)	$R^{*}_{\rm Gal}$ (kpc)	$E(B-V)$ (mag)	Ref.
IC 2391	08 40 32.00	−53 02 00.00	50±30	151±2	8.00±0.01	<0.05	1,2
IC 2602	10 42 58.00	−64 24 00.00	30±20	152±3	7.95±0.01	0.02-0.04	3
IC 4665	17 46 18.00	+05 43 00.00	40±10	345±12	7.72±0.01	0.16-0.19	4
NGC 2264	06 40 58.00	+09 53 42.00	3-5±4**	723±57	8.66±0.13	0.075	5,6
NGC 2516	07 58 04.00	−60 45 12.00	130±60	409±18	7.98±0.01	0.11	7
NGC 2547	08 10 25.70	−49 10 03.00	50±20	387±15	8.05±0.01	0.12	8

References: 1) Barrado y Navascués et al. (1999); 2) Barrado y Navascués et al. (2004); 3) van Leeuwen (2009); 4) Cargile & James (2010); 5) Sung et al. (2004); 6) Turner (2012); 7) Bailey et al. (2018); 8) Naylor & Jeffries (2006)

Notes: The clusters are sorted by name. The distances (fifth column) are from Cantat-Gaudin et al. (2018). The asterisk indicates ages and Galactocentric distances ($R_{\rm Gal}$) from Netopil et al. (2016). We adopted $R_{\rm Gal,\odot}$=8.00 kpc. The double asterisk indicates the age value from Venuti et al. (2018).

with the derivation of the input values of the atmospheric parameters from photometry. In Section 2.3 I present the determination of the stellar parameters by employing the new method that is almost entirely based on the use of *titanium* lines. I also derive abundances for different α-, proton-capture, and iron-peak elements, namely Fe I, Fe II, Ti I, Ti II, Na I, Mg I, Al I, Si I, Ca I, Cr I, and Ni I. In Sections 2.4 and 2.5 I present my results and discuss the scientific implications.

2.2 Data-set and input values of the atmospheric parameters

2.2.1 The UVES spectra

I analysed high-resolution (R∼47000) spectra of 23 dwarf stars with spectral type from F9 to K1, observed in five YOCs and one SFR in the *Gaia*-ESO Survey. The selected targets are IC 2391 ($t\sim50$ Myr), IC 2602 ($t\sim30$ Myr), IC 4665 ($t\sim40$ Myr), NGC 2264 ($t\sim3-5$ Myr), NGC 2516 ($t\sim150$ Myr), and NGC 2547 ($t\sim50$ Myr). Some information on these objects are reported in Table 2.1.

The spectra of the target stars were acquired with the high-resolution Fiber Large Array Mulit-Element Spectrograph and the Ultraviolet and Visual Echelle Spectrograph (FLAMES-UVES) (Pasquini et al. 2002a) and have been reduced by the *Gaia*-ESO consortium in a homogeneous way. The data reduction of UVES spectra was carried out using the FLAMES-UVES ESO public pipeline (Modigliani et al. 2004; Sacco et al. 2014).

The observations were performed with the UVES-580 nm setup for FGK type stars, with the spectra covering the 4800-6800 Å wavelength range. In particular, this spectral range contains the 6708 Å line of ^{7}Li, which is an important diagnostic of stellar age. I did not consider the GIRAFFE spectra because their spectral range is limited and they have a lower resolution.

Different Working Groups (WGs) of *Gaia*-ESO contribute to the spectrum analysis: for the stars considered here, the analysis was performed by WG11 and WG12. The details of the procedures are described in Smiljanic et al. (2014) and Lanzafame et al. (2015). The recommended parameters produced by this analysis are reported in the iDR5 catalogue and are used as comparison for the results I obtained with my new approach.

Of all the available spectra, I selected only stars with rotational velocities $v \sin i <$ 20 km s^{-1} to avoid significant or heavy line blending, with signal-to-noise ratios (S/N) per pixel higher than 50. Cool ($T_{\rm eff} < 5200$ K) dwarf stars are affected by the so-called overionisation effect (Schuler et al. 2010). It has been confirmed by different studies (Schuler et al. 2006; D'Orazi et al. 2009a; Schuler et al. 2010; Tsantaki et al. 2013, 2019) that differences of abundances between neutral and ionised species of the order of +0.8 dex are found in cool dwarf stars. Such differences increase dramatically as the age of the star decreases, and affect the $\log g$ determination through the ionisation equilibrium, for which one gets un-physical values.

All selected stars are confirmed members of the corresponding clusters through radial velocities (RVs) and the strength of the ^{7}Li absorption line at 6708Å, according to the *Gaia*-ESO iDR5 measurements.

Together with the cluster stars, I also analysed the Sun and 4 Gaia Benchmark stars (GBS) whose atmospheric parameters cover the parameter space of the cluster stars. The selected GBS are α Cen A, τ Cet, β Hyi, and 18 Sco, for which the spectra were taken from Blanco-Cuaresma et al. (2014b).

2.2.2 Initial guess estimates

Initial $T_{\rm eff}$ estimates were obtained using photometry from the Two Micron All-Sky Survey (2MASS) (Cutri et al. 2003) with the calibrated relation by Casagrande et al. (2010), valid for $(J-K)$ de-reddened colours in the range $0.07 < (J-K)_0 < 0.80$ mag. I used this photometry because it provides homogeneous data for the stars in this study.

The following classical equation was used to derive the initial values of $\log g$:

$$\log g_{\rm phot} = \log g_\odot + \log\left(\frac{m_\star}{m_\odot}\right) + 4\cdot\log\left(\frac{T_{\rm eff}}{T_{\rm eff,\odot}}\right) + 0.4\cdot(M_K + BC_K - M_{BC,\odot}), \qquad (2.1)$$

where $T_{\rm eff,\odot}$=5771 K, $\log g_\odot$=4.44 dex, and $M_{BC,\odot}$=4.74. $T_{\rm eff}$ is the $T(J-K)$ estimate and M_K is the absolute magnitude in K band, calculated with the distance estimates reported in Table 2.1. BC_K is the bolometric correction in K band, calculated as in Masana et al. (2006).

The values of $m_\star$ were estimated using the Padova suite of isochrones (Marigo et al. 2017). From these, I inferred the mass to be equal to 1 $M_\odot$ for the five YOCs, while $m_\star$=2-3 $M_\odot$ for the stars in the SFR.

The input ξ values were derived using the *Gaia*-ESO relation calibrated for warm main-sequence stars:

$$\begin{aligned}\xi_{\rm phot} =&1.10 + 6.04\,10^{-4} \cdot (T_{\rm eff} - 5787) + 1.45\,10^{-7} \cdot (T_{\rm eff} - 5787)^2 - \\ &- 3.33\,10^{-1} \cdot (\log g - 4.14) + 9.77\,10^{-2} \cdot (\log g - 4.14)^2 + \\ &+ 6.94\,10^{-2} \cdot ([{\rm Fe/H}] + 0.33) + 3.12\,10^{-2} \cdot ([{\rm Fe/H}] + 0.33)^2,\end{aligned} \tag{2.2}$$

which is valid for stars with $T_{\rm eff} \geq 5200$ K and $\log g \geq 3.5$ dex. In all the calibrated relations used to derive $T_{\rm eff}$, the bolometric correction, and ξ, the input metallicity was assumed to be solar (later confirmed by the chemical abundances analysis).

The basic information on the individual targets are reported in Table 2.2: the *Gaia*-ESO iDR5 identifier are in Column 1; the corresponding SIMBAD name in Column 2; the celestial coordinates Ra and Dec are in Column 3 and 4, respectively; V magnitudes form APASS (with the exception of 4 stars, whose valeus are taken from NOMAD catalogue) and J,H,K form 2MASS are reported in Column 5, 6, 7, and 8, respectively; $v \sin i$ from the GES iDR5 catalog (measured by the *Osservatorio Astrofisico di Catania* (OACT) Node of the *Gaia*-ESO consortium, measured using the routine ROTFIT; see, e.g., Frasca et al. 2015, and references therein, for more details) are in Column 9; initial guess of temperature, gravity and microturbulence (namely $T_{\rm eff\ phot}$, $\log g_{\rm\ phot}$, and $\xi_{\rm phot}$) are in Column 10, 11, and 12.

2.3 The new approach: Ti+Fe

To derive spectroscopic atmospheric parameters and element abundances of the target stars, I used the lines analysis and synthetic spectra code MOOG[1] (version 2017, Sneden 1973; Sobeck et al. 2011). Abundances of Fe I, Fe II, Ti I, Ti II, Na I, Mg I, Al I, Si I, Ca I, Cr I, and Ni I were estimated using the EW method with the *abfind* driver.

The 1D model atmospheres linearly interpolated from MARCS grid (Gustafsson et al. 2008) were used, in the assumption that local thermodynamic equilibrium (LTE) and plane-parallel geometry, which is valid for dwarf stars. I chose these atmosphere models

---

[1] https://www.as.utexas.edu/ chris/moog.html

Table 2.2: Basic information on individual stars and initial guesses of atmospheric parameters.

GES cName	SIMBAD	Ra (J2000)	Dec (J2000)	V (APASS)	J	H	K	$v \sin i$ (km s^{-1})	$T_{\mathrm{eff\ phot}}$ (K)	$\log g_{\mathrm{phot}}$	ξ_{phot} (km s^{-1})
				IC 2391							
08365498-5308342	Cl*IC2391 PMM3359	08:36:54.99016	-53:08:34.2712	11.533	10.119	9.734	9.616	8.5 ± 0.8	5215±118	4.47±0.06	0.70±0.03
08440521-5253171	V*V376 Vel	08:44:05.22238	-52:53:17.1917	10.746	9.603	9.258	9.165	16.7 ± 0.8	5471±103	4.28±0.06	0.88±0.04
				IC 2602							
10440681-6359351	V*V558 Car	10:44:06.81054	-63:59:35.0568	11.260^{a}	9.727	9.356	9.311	12.2 ± 0.7	5600±162	4.46±0.07	0.92±0.07
10442256-6415301	V*V559 Car	10:44:22.55146	-64:15:30.1163	10.897	9.687	9.372	9.322	10.9 ± 0.8	5825±117	4.49±0.07	1.04±0.06
10481856-6409537	V*V567 Car	10:48:18.34247	-64:09:53.1409	10.276^{a}	8.886	8.541	8.505	14.4 ± 0.8	5753±114	4.18±0.06	1.09±0.05
				IC 4665							
17442711+0547196	Cl*IC4665 P173	17:44:27.10591	+05:47:19.5724	13.468	11.816	11.39	11.267	14.5 ± 1.0	5397±103	4.43±0.03	0.80±0.04
17445810+0551329	2MASSJ17445810+0551329	17:44:58.10225	+05:51:32.8689	13.444	11.828	11.43	11.34	10.0 ± 0.9	5650±118	4.49±0.03	0.91±0.06
17452508+0551388	V*V2318 Oph	17:45:25.07245	+05:51:38.8712	13.825	12.004	11.52	11.436	13.5 ± 0.7	5321±108	4.48±0.03	0.75±0.04
				NCG 2264							
06405694+0948407	NGC2264 125	06:40:56.95085	+09:48:40.7271	12.323	11.164	10.917	10.825	15 ± 3.8	6081±162	4.15±0.11	1.29±0.08
				NGC2516							
07544342-6024437	GESJ07544342-6024437	07:54:43.41543	-60:24:43.6177	13.904	12.353	11.959	11.862	3^{b}	5487±133	4.69±0.06	0.78±0.06
07550592-6104294	GESJ07550592-6104294	07:55:05.91544	-61:04:29.5043	13.452	11.926	11.542	11.455	11.8 ± 0.8	5570±107	4.51±0.05	0.87±0.04
07551977-6104200	GESJ07551977-6104200	07:55:19.74694	-61:04:19.8791	13.161	11.701	11.353	11.339	14.6 ± 1.1	6064±161	4.59±0.06	1.15±0.10
07553236-6023094	GESJ07553236-6023094	07:55:32.35296	-60:23:09.3785	13.505	12.084	11.706	11.652	9.2 ± 1.2	5739±114	4.59±0.05	0.94±0.05
07564410-6034523	Cl*NGC2516 DAC245	07:56:44.11234	-60:34:52.2419	13.548	12.121	11.721	11.682	7.9 ± 0.8	5708±112	4.61±0.05	0.92±0.05
07573608-6048128	Cl*NGC2516 EGG112	07:57:36.07772	-60:48:12.7140	13.78	12.206	11.809	11.74	4.6 ± 1.0	5592±108	4.62±0.05	0.85±0.05
07574792-6056131	Cl*NGC2516 DAC514	07:57:47.91111	-60:56:13.1008	13.30^{a}	12.261	11.873	11.801	3.2 ± 1.7	5617±109	4.73±0.05	0.84±0.05
07575215-6100318	Cl*NGC2516 JTH7454	07:57:52.13840	-61:00:31.6958	14.170^{a}	12.624	12.164	12.083	5.5 ± 0.9	5287±97	4.76±0.05	0.67±0.03
07583485-6103121	Cl*NGC2516 DAC622	07:58:34.86088	-61:03:12.0476	13.036	11.756	11.418	11.317	11.7 ± 1.3	5708±112	4.45±0.05	0.96±0.05
07584257-6040199	Cl*NGC2516 DAC914	07:58:42.56742	-60:40:19.9277	13.668	12.187	11.831	11.733	8.8 ± 0.7	5643±110	4.68±0.05	0.86±0.05
08000944-6033355	Cl*NGC2516 DAC830	08:00:09.44897	-60:33:35.5942	13.316	11.936	11.607	11.507	7.2 ± 1.1	5753±145	4.60±0.06	0.95±0.07
08013658-6059021	Cl*NGC2516 AR323	08:01:36.57484	-60:59:02.1588	13.488	12.086	11.746	11.639	8.9 ± 0.9	5673±111	4.54±0.06	0.92±0.05
				NGC 2547							
08102854-4856518	2MASSJ08102854-4856518	08:10:28.53907	-48:56:51.8506	12.723	11.471	11.137	11.047	15.3 ± 0.8	5800±148	4.34±0.05	1.04±0.07
08110139-4900089	2MASSJ08110139-4900088	08:11:01.40435	-49:00:08.8889	13.468	12.016	11.642	11.511	8.8 ± 0.8	5453±103	4.51±0.05	0.80±0.04

a) V magnitudes from NOMAD (Zacharias et al. 2004);

b) no error provided because it is an upper limit (VSINI FLAG=1);

Table 2.3: Atomic line data. The references for the $\log gf$ values are reported in Column 5. EWs and abundances for the Sun are reported in Columns 6 and 7. The abundances are in the log(X) scale. The full Table is available at the CDS. A portion is shown here for guidance regarding its form and content.

Element	λ (Å)	E.P. (eV)	$\log gf$	Ref.	$\mathrm{EW}_\odot$ (mÅ)	$\log(\mathrm{X})_\odot$
Na I	4982.814	2.104	−0.916	Froese Fischer & Tachiev (2012)	75.34	6.223
Na I	5682.633	2.102	−0.706	Froese Fischer & Tachiev (2012)	106.92	6.259
...	...	...	...	...	...	...

to be consistent with the analysis of the UVES spectra performed by the *Gaia*-ESO consortium. The lines I used were taken from D'Orazi et al. (2017), originally selected from the line list optimised for solar-type stars from Meléndez et al. (2014). I cross-matched our original line list with the official *Gaia*-ESO line list (Heiter et al. 2019) to adopt the same atomic data, in particular the value for the oscillator strength ($\log gf$). An extract of the line list can be found in Table 2.3, while the full Table is available at the CDS[2]. The Barklem prescription for damping values was adopted (see Barklem et al. 2000 and references therein).

The EWs for all the lines were measured using the software ARESv2 (Sousa et al. 2015)[3]. I discarded all the lines with uncertainties larger than 10% and those lines with EWs>120 mÅ because stronger lines cannot be fitted well with a Gaussian profile. In some cases, especially for stars with relatively high rotational velocities, I added lines by measuring their EWs by hand using the task *splot* in IRAF.

Given the issues related to Fe lines formation, I developed a new approach that derives the atmospheric parameters using the second element with the largest number of spectral lines measurable in the considered stellar types (both of the neutral and the ionised species): *titanium*. On average, Ti lines form deeper in the photosphere than the Fe lines, at $\log\tau_{5000} \sim -1$, where $\log\tau_{5000}$ is the optical depth expressed in the logarithmic scale and calculated at the 5000 Å reference wavelength (Gurtovenko & Sheminova 2015). Therefore, little influence from the chromosphere or the active layers at these depths is expected. In other words, we do not expect any trend between abundances and line formation depth. Moreover, Ti lines have very precise laboratory measurements of the $\log gf$ values from Lawler et al. (2013). Recently, Tsantaki et al. (2019) have argued that especially for cool dwarf stars, the atmospheric parameter values derived with Ti lines are more reliable than those derived with Fe lines. However, the authors used Ti lines only

---

[2] `https://vizier.u-strasbg.fr/viz-bin/VizieR?-source=J/A+A/634/A34`

[3] http://www.astro.up.pt/ sousasag/ares/

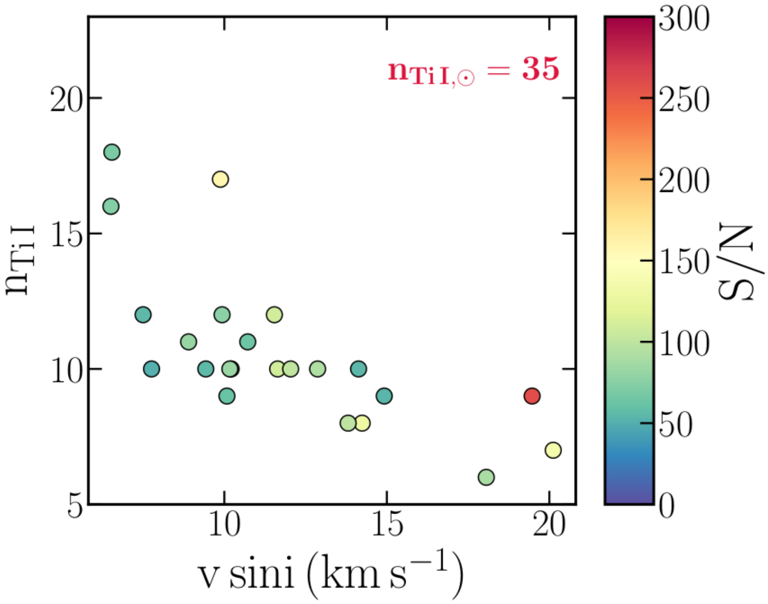

Figure 2.2: Number of Ti I lines measured for each star as a function of S/N, colour-coded according to $v \sin i < 20$ km s^{-1}. Stars with similar S/N but higher rotational velocities have fewer measurable lines. The number of Ti I lines measured in the Sun is reported in red in the top right corner.

to impose the ionisation balance, in order to infer surface gravity estimates. Here I expand upon this approach in order to overcome the analytical issues related to the formation of Fe lines.

In summary, my new approach develops through the following three steps:

- deriving T_{eff} by zeroing the trend between E.P. and abundances of Ti I and Fe I lines *simultaneously*;
- deriving $\log g$ by imposing the ionisation equilibrium for Ti lines alone;
- deriving ξ by zeroing the trend between the REW of Ti I lines alone and the abundances.

2.3.1 Effective temperature

In the spectroscopic analysis, the T_{eff} is derived by imposing the excitation equilibrium (through the Boltzmann equation). Lines of different excitation potential (E.P.) will then have the same abundances.

The E.P. range covered by Fe I lines in the final list goes typically from 0 to 5.0 eV; instead, for Ti I lines considered in this work, it is slightly smaller, going from 0 to 2.0 eV. Unfortunately, the E.P. range of Ti I lines only is too narrow to obtain a reliable estimate of T_{eff}. The values of T_{eff} derived with Ti lines only are higher than the photometric estimates by 200-300 K, with uncertainties of the order of 200 K.

Moreover, in some stars, especially those with higher $v \sin i$, the number of measurable Ti lines is very low, in some cases less than ten lines, as it is shown in Figure 2.2. In the Sun (and also in the GBS stars) I measured the EWs of 35 Ti I lines, but these correspond to an old star that rotates significantly slower than the younger stars in the sample.

To increase the number of lines and to obtain a wider coverage of the E.P. range, I derived T_{eff} values using Fe I and Ti I lines *simultaneously*. Tables 2.4 and 2.5 show that the agreement between the three different estimates of T_{eff} (photometric, with Fe lines only and with Fe+Ti lines) for the GBS and the cluster stars (respectively) is very good.

The final $T_{\text{eff,spec}}$ is obtained by imposing the excitation equilibrium to Ti+Fe lines, i.e. the slope of the trend between individual line abundances and the corresponding E.P. is lower than the uncertainty on the slope, and the trend is not statistically meaningful. The top panel of Fig. 2.3 show an example, where in the y-axis the difference between individual lines and the mean values per atomic species is reported and was calculated as $\Delta_{\log \mathrm{n(X)}} = \log \mathrm{n(X)_i} - \log \mathrm{n(X)_{mean}}$.

2.3.2 Surface gravity

In the new approach, $\log g$ is derived by imposing the ionisation equilibrium of Ti I and Ti II lines. The difference between Ti I and Ti II is of the order of the quadratic sum of the uncertainties calculated by MOOG (i.e., the rms of the measurements, mainly due to the EWs values) divided by the square root of the number of lines of the two species. With reference to the number of ionised lines, for the Sun I measured 11 Ti II lines and all of these lines have been measured in the GBS also. Instead, for my sample stars I measured from 4 to 8 lines, depending on the quality of the spectra.

2.3.3 Microturbulence velocity

As already mentioned in Section 2.1, the ξ parameter is an ad hoc parameter introduced in 1D analysis to explain the discrepancy between the measured and predicted EWs of strong lines due to small-scale motions of matter. It is derived by imposing that weak and strong lines of the same element have the same abundance.

In the new approach, I considered Ti I lines *only*. In Figure 2.3, I show an example of the observed trend obtained with the final parameters for star 8365498−5308342 that belongs to IC 2391 (age 50 Myr). The green dots represent the Fe I lines, and the blue squares represent the Ti I lines; in all the panels, the red continuous lines are the linear regressions. The individual slope and uncertainties are reported for the trends in each pan-

Table 2.4: Atmospheric parameters and chemical composition of Gaia benchmarks stars. We also report the value from the literature (i.e. ξ values from Jofré et al. 2015b -J15-, while $T_{\rm eff}$, $\log g$, [Fe/H] and [Ti/H] are from Jofré et al. 2018 -J18-) and from the *Gaia*-ESO iDR5 catalogue (GESiDR5). The numbers of the lines we used in the analysis are in square brackets. The uncertainties are calculated as the quadratic sum of the σ_1 and σ_2 contributions.

	Sun	αCen A	τCet	βHyi	18Sco
$T_{\rm eff,J18}$ (K)	5771±1	5792±16	5414±21	5873±45	5810±80
$\log g_{\rm J18}$ (dex)	4.44±0.00	4.30±0.01	4.49±0.01	3.98±0.02	4.44±0.03
$\xi_{\rm J15}$ (km s^{-1})	1.06±0.18	1.20±0.07	0.89±0.28	1.26±0.05	1.07±0.20
[Fe/H]$_{\rm J18}$ (dex)	0.03±0.05	0.26±0.08	−0.49±0.03	−0.04±0.06	0.03±0.03
[Ti/H]$_{\rm J18}$ (dex)	0.00±0.07	0.21±0.04	−0.17±0.07	−0.07±0.04	0.05±0.03
$T_{\rm eff,GESiDR5}$ (K)	5734±62	5813±60	5344±59	5828±116	5776±58
$\log g_{\rm GESiDR5}$ (dex)	4.45±0.12	4.35±0.11	4.56±0.11	3.90±0.23	4.42±0.11
$\xi_{\rm GESiDR5}$ (km s^{-1})	0.90±0.18	1.06±0.08	0.61±0.30	1.25±0.07	0.99±0.13
[Fe/H]$_{\rm GESiDR5}$ (dex)	0.06±0.11	0.27±0.11	−0.50±0.13	−0.06±0.10	0.08±0.07
[Ti/H]$_{\rm GESiDR5}$ (dex)	4.95±0.03*	0.26±0.01	−0.23±0.04	−0.05±0.03	0.03±0.02
$T(J-K)$ (K)	5777±1	5845±61	5401±51	5702±80	5295±134
$\log g_{\rm phot}$ (dex)	4.43±0.01	4.32±0.04	4.47±0.03	3.91±0.04	4.28±0.48
$\xi_{\rm phot}$ (km s^{-1})	1.00±0.00	1.08±0.03	0.79±0.02	1.13±0.03	0.79±0.15
$T_{\rm eff}$(Fe I) (K) [N$_{\rm lin}$]	5777±100 [59]	5845±75 [55]	5401±50 [59]	5800±100 [57]	5800±100 [59]
$T_{\rm eff}$(Fe I+Ti I) (K) [N$_{\rm lin}$]	5790±50 [94]	5830±75 [89]	5401±75 [98]	5870±100 [87]	5875±100 [100]
$\log g_{\rm spec}$ (dex)	4.47±0.05	4.45±0.10	4.38±0.10	3.95±0.10	4.55±0.10
$\xi_{\rm spec}$ (km s^{-1})	1.00±0.10	1.09±0.20	0.89±0.15	1.35±0.10	1.15±0.15
[Fe/H]$_{\rm I}$ (dex)	7.44±0.04*	0.23±0.02	−0.44±0.02	−0.09±0.02	0.06±0.02
[Fe/H]$_{\rm II}$ (dex)	7.45±0.03*	0.21±0.05	−0.44±0.05	−0.09±0.05	0.05±0.04
[Ti/H]$_{\rm I}$ (dex)	4.92±0.05*	0.26±0.05	−0.20±0.04	−0.09±0.02	0.09±0.03
[Ti/H]$_{\rm II}$ (dex)	4.93±0.04*	0.25±0.04	−0.19±0.04	−0.08±0.04	0.08±0.05

* The solar values are in log(X) scale.

Table 2.5: Different values of $T_{\rm eff}$ derived with photometry, from Fe lines alone, and from Fe and Ti simultaneously. We also report the number of the Fe and Ti lines that we measured for each star.

CNAME	$T_{\rm eff,phot}$ (K)	$T_{\rm Fe\,I}$ (K)	$T_{\rm Fe\,I+Ti\,I}$ (K)	$n_{\rm Fe\,I}$	$n_{\rm Ti\,I}$
		IC 2391			
08365498−5308342	5215±118	5150±100	5150±100	39	17
08440521−5253171	5471±103	5471±50	5471±75	35	9
		IC 2602			
10440681−6359351	5600±162	5500±100	5500±75	32	10
10442256−6415301	5825±117	5765±75	5765±75	40	12
10481856−6409537	5753±114	5700±100	5680±100	29	8
		IC 4665			
17442711+0547196	5397±103	5280±75	5397±75	15	9
17445810+0551329	5650±118	5600±75	5575±75	31	11
17452508+0551388	5321±108	5200±100	5271±100	17	10
		NGC 2264			
06405694+0948407	6081±162	6150±75	6150±75	30	7
		NGC 2516			
07544342−6024437	5487±133	5325±75	5300±100	46	16
07550592−6104294	5570±107	5500±75	5500±75	30	10
07551977−6104200	6064±161	6064±100	6050±100	33	8
07553236−6023094	5739±114	5650±75	5625±75	33	10
07564410−6034523	5708±112	5600±75	5600±75	28	10
07573608−6048128	5592±108	5572±100	5572±75	35	12
07574792−6056131	5617±109	5525±75	5515±75	35	18
07575215−6100318	5287±97	5200±75	5170±75	33	10
07583485−6103121	5708±112	5758±75	5730±75	28	10
07584257−6040199	5643±110	5525±75	5500±75	33	10
08000944−6033355	5753±145	5700±75	5700±75	32	11
08013658−6059021	5673±111	5600±75	5575±75	28	9
		NGC 2547			
08102854−4856518	5800±148	5800±100	5800±100	24	6
08110139−4900089	5453±103	5250±75	5353±100	32	12

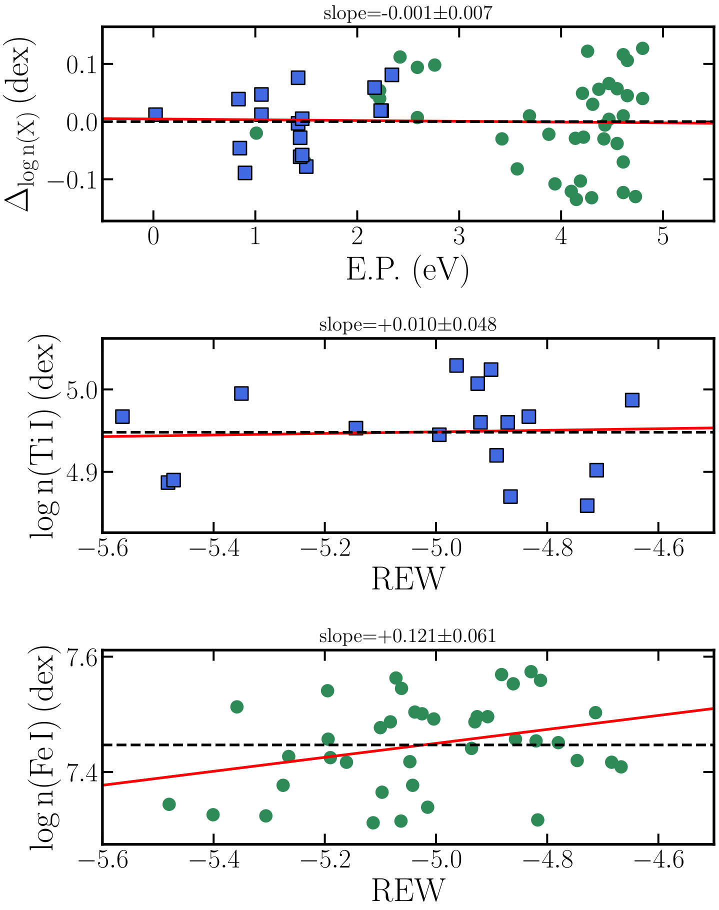

Figure 2.3: Example of applying the new method for star 08365498−5308342 (IC 2391, age 50 Myr). The stellar parameters obtained with the Ti+Fe approach are $T_{\rm eff}$ =5215 ± 100 K, log g =4.35 ± 0.10 dex and ξ = 0.85 ± 0.10 km s^{-1}. It is clear from the bottom panel that such value of ξ is too low and one needs to increase it.

els. The final stellar parameters obtained with the new procedure are $T_{\rm eff}$ = 5215 ± 100 K, log g = 4.35 ± 0.10 km s^{-1} and ξ = 0.85 ± 0.10 km s^{-1}. As it can be seen, the Ti lines (blue squares) suggest that such value is a good estimate of the microturbulence, and it is in very good agreement with the initial guess (that is 0.70 ± 0.03 km s^{-1}). However, the Fe lines (green dots) suggest that the microturbulence is equal to at least 1.75 km s^{-1}. Looking at Figure 2.4 (the same as Figure 2.1), it is clear that the synthetic profiles obtained with the stellar parameters derived with my new approach (blue lines) reproduce the observed lines better.

When the star had fewer than ten measurable Ti I lines, I kept the ξ value fixed to the $\xi_{\rm phot}$ of Table 2.2 (for a total of 7 of 23 stars). Microturbulence is coupled with the derivation of $T_{\rm eff}$ and the interplay between the parameters may affect the final values of the abundance. To evaluate the impact of keeping the ξ fixed to the photometric guess when too few lines are measured, I re-derived the atmospheric parameters main-

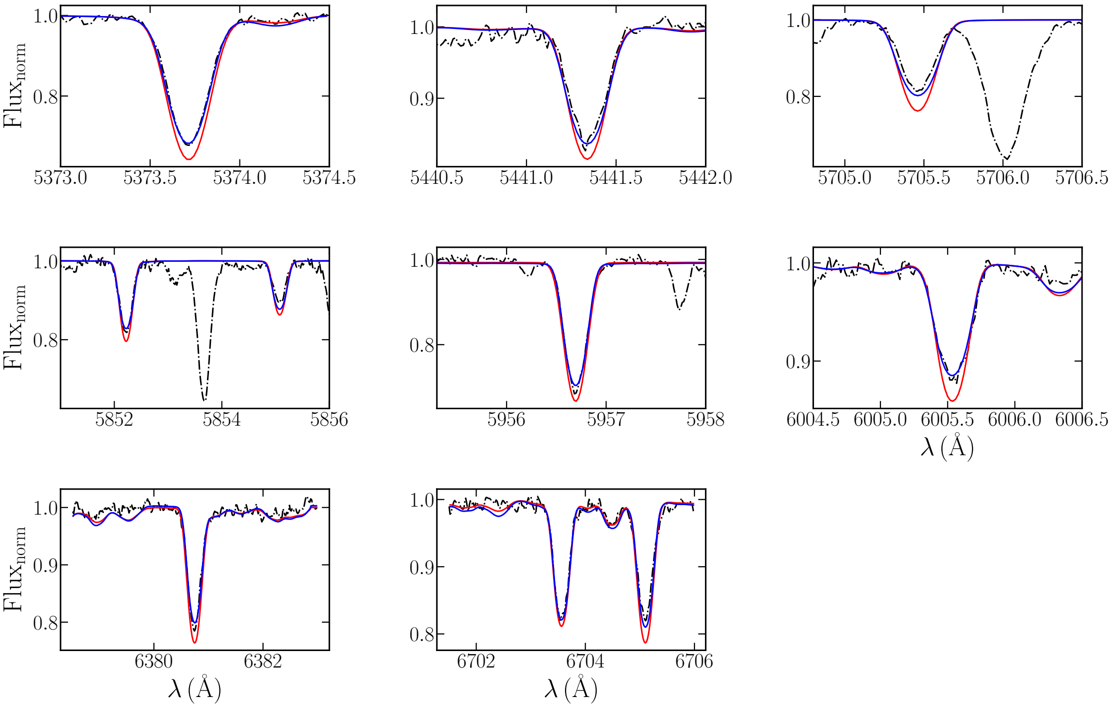

Figure 2.4: Examples of the synthesis of several Fe I lines of star 08365498−5308342 ($v \sin i$ = 9.88 km s^{-1}, as the recommended value given in the iDR5) for which the observed profile is not fitted when we adopt the ξ value obtained from the Fe lines (ξ=1.75 km s^{-1} ; red line) and with the values derived with the new method (ξ=0.85 km s^{-1} ; blue line).

taining for ξ the initial guesses. I consider two stars with very discrepant ξ values, i.e., 17452508+0551388 (IC 4665, age 40 Myr: $\xi_{\rm spec}-\xi_{\rm phot}$=+0.28 km s^{-1}) and 08110139−04900089 (NGC 2547, age 50 Myr: $\xi_{\rm spec}-\xi_{\rm phot}$=+0.25 km s^{-1}). I find that for first star the new parameters are equal to $T_{\rm eff}$=5321±150 K, log g=4.35±0.10 dex, and ξ=0.75±0.04 km s^{-1}, while for the second one, I find $T_{\rm eff}$=5325±100 K, log g=4.47±0.10 dex, and ξ=0.80±0.04 km s^{-1}. The difference between the newly derived $T_{\rm eff}$ and those derived with my method is lower than 50 K and lower than the typical error (75-100 K) obtained for the $T_{\rm eff}$ parameter, in both cases. Therefore, the two $T_{\rm eff}$ measurements are consistent and the effect of these differences on the final metallicity values is weak.

The final model atmospheres and abundances of the GBS and the cluster sample are reported in Table 2.4 and 2.6, respectively. Once the atmospheric parameters have been found, the final abundances are calculated differentially with respect to the Sun. I also calculated the abundances for other different α- and proton-capture and iron-peak elements, in particular, Na I, Mg I, Al I, Si I, Ca I, Cr I, and Ni I. The respective abundance ratios [X/Fe] were calculated as $[{\rm X/Fe}]=[{\rm X/H}]_\star-[{\rm Fe/H}]_\star$ (in particular for the ionised species, $[{\rm Ti/Fe}]_{\rm II}$ = $[{\rm Ti/H}]_{\rm II}-[{\rm Fe/H}]_{\rm II}$). The final abundance ratios are reported in Table 2.7.

2.3.4 Uncertainties estimates

The uncertainties of the atmospheric parameters reported in Tables 2.5 and 2.6 were estimated as follows. $\sigma_{T_{\rm eff}}$ was calculated by varying the temperature until the slope E.P. versus abundance was larger than its uncertainty and the trend became statistically meaningful. $\sigma_{\log g}$ was estimated by varying log g until Δ(Ti II−Ti I) was larger than the quadratic sum of the uncertainties. Finally, σ_ξ was calculated by varying ξ until the slope of the trend was larger than the uncertainty on the slope and the trend became statistically meaningful. In general, the uncertainties for each stars are about 75-100 K, 0.10-0.15 dex, and 0.10-0.15 km s^{-1} for $T_{\rm eff}$, log g, and ξ, respectively.

The uncertainties on the abundances, σ_1 and σ_2 reported in Table 2.6, include the internal uncertainties and the contribution of the atmospheric parameters into account, respectively. The first source of uncertainty, σ_1, can be represented by the standard deviation from the mean abundance considering all the lines divided by the square root of the number of lines. The σ_2 values instead represent the sensitivity of [X/H] to the uncertainties in the atmospheric parameters, and this sensitivity is calculated as

$$\sigma_2 = \sqrt{\left(\sigma_{T_{\rm eff}}\frac{\partial[{\rm X/H}]}{\partial T_{\rm eff}}\right)^2 + \left(\sigma_{\log\,{\rm g}}\frac{\partial[{\rm X/H}]}{\partial \log\,{\rm g}}\right)^2 + \left(\sigma_{\xi}\frac{\partial[{\rm X/H}]}{\partial \xi}\right)^2}.$$

Table 2.6: Derived stellar parameters and abundances with the final models and comparison with the photometric values.

CNAME	$\log g_{phot}$ (dex)	ξ_{phot} (km s^{-1})	$T_{\rm spec}$ (K)	$\log g_{spec}$ (dex)	ξ_{spec} (km s^{-1})	[Fe/H]$_{\rm I}$ ± σ_1 ± σ_2	[Fe/H]$_{\rm II}$ ± σ_1 ± σ_2	[Ti/H]$_{\rm I}$ ± σ_1 ± σ_2	[Ti/H]$_{\rm II}$ ± σ_1 ± σ_2
						IC 2391			
08365498-5308342	4.47±0.06	0.70±0.03	5215±100	4.35±0.10	0.85±0.10	0.00±0.01±0.06	0.09±0.03±0.08	0.01±0.01±0.13	0.02±0.03±0.05
08440521-5253171	4.28±0.06	0.88±0.04	5471±100	4.20±0.10	-	0.00±0.02±0.07	0.05±0.03±0.06	0.01±0.02±0.12	0.02±0.04±0.06
						IC 2602			
10440681-6359351	4.46±0.07	0.92±0.07	5525±75	4.38±0.15	1.00±0.20	0.00±0.01±0.06	0.08±0.03±0.06	0.06±0.02±0.10	0.07±0.04±0.05
10442256-6415301	4.49±0.07	1.04±0.06	5775±75	4.49±0.10	1.15±0.10	0.04±0.01±0.07	0.05±0.02±0.05	0.02±0.02±0.10	0.02±0.03±0.04
10481856-6409537	4.18±0.06	1.09±0.05	5680±100	4.10±0.10	-	0.03±0.02±0.07	0.06±0.03±0.06	0.01±0.02±0.10	0.02±0.04±0.06
						IC 4665			
17442711+0547196	4.43±0.03	0.80±0.04	5380±75	4.48±0.10	-	0.14±0.02±0.05	0.17±0.02±0.06	0.05±0.03±0.09	0.04±0.02±0.04
17445810+0551329	4.49±0.03	0.91±0.06	5575±75	4.47±0.10	0.96±0.10	0.12±0.01±0.07	0.13±0.04±0.04	0.13±0.02±0.11	0.15±0.03±0.05
17452508+0551388	4.48±0.03	0.75±0.04	5300±100	4.27±0.15	1.03±0.10	0.05±0.03±0.06	0.11±0.03±0.08	0.12±0.02±0.13	0.14±0.04±0.06
						NGC 2264			
06405694+0948407	4.15±0.11	1.29±0.08	6150±75	4.05±0.10	-	0.10±0.02±0.07	0.11±0.02±0.05	0.13±0.02±0.09	0.15±0.04±0.05
						NGC 2516			
07544342-6024437	4.69±0.06	0.78±0.06	5430±100	4.51±0.10	1.05±0.10	0.03±0.01±0.07	0.04±0.03±0.08	0.02±0.02±0.11	0.03±0.02±0.05
07550592-6104294	4.51±0.05	0.87±0.04	5550±75	4.20±0.10	0.95±0.10	0.05±0.03±0.07	0.08±0.02±0.06	0.04±0.02±0.09	0.04±0.02±0.05
07551977-6104200	4.59±0.06	1.15±0.10	6050±100	4.62±0.10	-	0.12±0.02±0.06	0.12±0.03±0.05	0.12±0.02±0.08	0.12±0.01±0.05
07553236-6023094	4.59±0.05	0.94±0.05	5700±75	4.52±0.10	1.15±0.15	0.09±0.01±0.07	0.13±0.01±0.07	0.12±0.02±0.08	0.13±0.02±0.05
07564410-6034523	4.61±0.05	0.92±0.05	5650±75	4.45±0.10	1.02±0.10	0.13±0.02±0.06	0.14±0.04±0.05	0.13±0.02±0.08	0.13±0.03±0.04
07573608-6048128	4.62±0.05	0.85±0.05	5625±100	4.55±0.10	1.03±0.10	0.11±0.01±0.07	0.10±0.02±0.08	0.11±0.03±0.11	0.11±0.04±0.05
07574792-6056131	4.73±0.05	0.84±0.05	5580±75	4.57±0.10	1.08±0.10	0.08±0.01±0.07	0.10±0.03±0.07	0.10±0.02±0.09	0.10±0.04±0.05
07575215-6100318	4.76±0.05	0.67±0.03	5275±100	4.54±0.10	0.98±0.10	0.07±0.02±0.05	0.10±0.05±0.08	0.10±0.02±0.09	0.11±0.02±0.05
07583485-6103121	4.45±0.05	0.96±0.05	5758±100	4.43±0.10	1.05±0.15	0.02±0.02±0.06	0.04±0.03±0.03	0.03±0.03±0.08	0.03±0.03±0.04
07584257-6040199	4.68±0.05	0.86±0.05	5550±75	4.48±0.10	0.98±0.10	0.09±0.01±0.06	0.08±0.04±0.06	0.09±0.02±0.09	0.09±0.02±0.05
08000944-6033355	4.60±0.06	0.95±0.07	5675±100	4.38±0.10	0.90±0.10	0.05±0.02±0.05	0.06±0.02±0.05	0.06±0.02±0.08	0.08±0.01±0.04
08013658-6059021	4.54±0.06	0.92±0.05	5585±100	4.32±0.10	-	0.06±0.02±0.06	0.07±0.02±0.05	0.08±0.02±0.09	0.08±0.02±0.04
						NGC 2547			
08102854-4856518	4.34±0.05	1.04±0.07	5800±100	4.20±0.10	-	0.11±0.02±0.07	0.14±0.03±0.05	0.10±0.01±0.10	0.11±0.03±0.04
08110139-4900089	4.51±0.05	0.80±0.04	5375±100	4.50±0.10	1.05±0.10	0.05±0.01±0.06	0.10±0.04±0.08	0.08±0.02±0.12	0.09±0.03±0.05

Table 2.7: Abundance ratios for different species.

CNAME	[Na/Fe]$\pm\sigma_1 \pm \sigma_2$	[Mg/Fe]$\pm\sigma_1 \pm \sigma_2$	[Al/Fe]$\pm\sigma_1 \pm \sigma_2$	[Si/Fe]$\pm\sigma_1 \pm \sigma_2$	[Ca/Fe]$\pm\sigma_1 \pm \sigma_2$	[Ti/Fe]$_{\mathrm{I}} \pm \sigma_1 \pm \sigma_2$	[Ti/Fe]$_{\mathrm{II}} \pm\sigma_1 \pm \sigma_2$	[Cr/Fe]$\pm\sigma_1 \pm \sigma_2$	[Ni/Fe]$\pm\sigma_1 \pm \sigma_2$
IC 2391									
08365498-5308342	0.00±0.01±0.04	0.05±0.01±0.06	0.03±0.01±0.03	−0.01±0.02±0.07	0.08±0.01±0.09	0.01±0.01±0.07	−0.07±0.04±0.10	−0.04±0.04±0.14	−0.06±0.02±0.10
08440521-5253171	−0.06±0.02±0.13	−0.01±0.02±0.03	-	0.01±0.02±0.08	0.07±0.02±0.09	0.01±0.02±0.04	−0.03±0.03±0.08	0.05±0.02±0.03	−0.01±0.02±0.02
IC 2602									
10440681-6359351	0.02±0.06±0.10	−0.01±0.02±0.17	-	0.08±0.02±0.13	0.12±0.03±0.14	0.06±0.02±0.11	0.00±0.04±0.03	0.05±0.03±0.15	0.02±0.03±0.16
10442256-6415301	0.02±0.01±0.02	−0.05±0.01±0.06	-	−0.03±0.02±0.07	0.04±0.02±0.07	−0.02±0.02±0.07	−0.03±0.03±0.06	0.08±0.03±0.14	0.02±0.01±0.03
10481856-6409537	0.02±0.01±0.04	−0.03±0.01±0.05	−0.01±0.01±0.05	−0.02±0.04±0.08	0.07±0.05±0.10	−0.02±0.02±0.04	−0.03±0.04±0.06	0.03±0.05±0.04	0.03±0.02±0.06
IC 4665									
17442711+0547196	−0.02±0.02±0.14	-	-	0.01±0.02±0.06	0.03±0.04±0.02	−0.09±0.03±0.16	−0.12±0.02±0.14	0.12±0.02±0.14	0.04±0.02±0.15
17445810+0551329	0.05±0.01±0.02	-	-	−0.01±0.02±0.08	0.09±0.03±0.04	0.02±0.02±0.04	0.02±0.03±0.04	0.06±0.02±0.10	0.07±0.02±0.06
17452508+0551388	0.10±0.03±0.16	-	-	0.08±0.03±0.17	0.09±0.03±0.04	0.08±0.03±0.12	0.05±0.04±0.08	0.06±0.03±0.04	0.07±0.02±0.14
NGC 2264									
06405694+0948407	0.06±0.02±0.07	−0.02±0.02±0.06	-	−0.01±0.02±0.04	0.02±0.01±0.04	0.03±0.02±0.06	0.04±0.03±0.14	0.02±0.03±0.04	0.00±0.02±0.02
NGC 2516									
07544342-6024437	−0.03±0.01±0.13	0.06±0.01±0.04	0.06±0.03±0.02	0.00±0.02±0.11	0.04±0.02±0.02	0.00±0.01±0.07	−0.01±0.03±0.14	0.04±0.04±0.05	0.02±0.02±0.03
07550592-6104294	−0.07±0.02±0.14	−0.11±0.01±0.12	-	−0.02±0.03±0.06	0.05±0.04±0.10	−0.02±0.02±0.04	−0.07±0.02±0.11	0.04±0.04±0.03	0.01±0.03±0.04
07551977-6104200	0.03±0.01±0.04	−0.13±0.01±0.13	-	−0.03±0.02±0.06	0.06±0.01±0.09	0.00±0.02±0.06	−0.01±0.03±0.06	0.07±0.02±0.06	0.05±0.03±0.09
07553236-6023094	−0.05±0.03±0.04	−0.10±0.01±0.15	-	−0.03±0.03±0.09	0.06±0.02±0.07	0.03±0.02±0.03	−0.01±0.02±0.05	−0.02±0.01±0.07	0.02±0.02±0.03
07564410-6034523	−0.01±0.01±0.15	−0.12±0.01±0.18	-	−0.06±0.03±0.12	0.05±0.04±0.010	0.00±0.01±0.03	−0.01±0.01±0.04	0.02±0.04±0.02	0.00±0.02±0.06
07573608-6048128	0.00±0.02±0.04	−0.10±0.01±0.16	-	−0.04±0.01±0.10	0.04±0.02±0.03	0.00±0.02±0.04	0.02±0.03±0.10	−0.02±0.02±0.04	−0.01±0.02±0.06
07574792-6056131	−0.09±0.01±0.1	-	−0.06±0.01±0.14	−0.05±0.02±0.08	0.00±0.02±0.10	0.02±0.02±0.06	0.01±0.04±0.03	0.02±0.02±0.09	0.03±0.02±0.05
07575215-6100318	0.03±0.05±0.05	-	-	−0.04±0.01±0.11	0.02±0.03±0.07	0.03±0.02±0.04	0.00±0.05±0.05	0.05±0.04±0.02	0.03±0.02±0.03
07583485-6103121	−0.04±0.02±0.09	−0.05±0.02±0.09	-	0.03±0.02±0.08	0.08±0.02±0.09	−0.01±0.02±0.03	−0.02±0.03±0.02	−0.06±0.04±0.10	0.06±0.02±0.12
07584257-6040199	0.00±0.01±0.05	−0.09±0.01±0.11	-	−0.03±0.03±0.07	0.03±0.03±0.05	0.01±0.02±0.03	0.01±0.02±0.03	0.08±0.01±0.09	0.01±0.02±0.03
08000944-6033355	−0.07±0.04±0.02	−0.05±0.01±0.02	-	−0.03±0.05±0.05	0.03±0.03±0.01	0.01±0.02±0.03	0.02±0.02±0.03	0.04±0.05±0.03	0.05±0.02±0.01
08013658-6059021	−0.01±0.01±0.15	0.00±0.01±0.09	-	0.02±0.02±0.07	0.06±0.04±0.09	0.02±0.02±0.04	0.00±0.02±0.03	-	0.07±0.01±0.10
NGC 2547									
08102854-4856518	−0.01±0.04±0.03	0.01±0.02±0.08	-	0.02±0.03±0.08	0.05±0.02±0.09	−0.02±0.01±0.05	−0.04±0.03±0.06	-	0.05±0.04±0.09
08110139-4900089	0.00±0.01±0.03	-	0.04±0.01±0.02	−0.03±0.02±0.07	0.09±0.02±0.13	0.04±0.02±0.07	−0.01±0.04±0.07	0.07±0.05±0.04	0.01±0.02±0.03

Table 2.8: Solar abundances derived here and in Asplund et al. (2009) (A09), and meteoritic abundances from Lodders et al. (2009) (L09). We also report the values derived by *Gaia*-ESO in iDR5 (GESiDR5).

Species	This work	A09	L09	GESiDR5
Na	6.24±0.04	6.24±0.04	6.27±0.02	6.17±0.05
Mg	7.63±0.02	7.60±0.04	7.53±0.01	7.51±0.07
Al	6.43±0.03	6.45±0.03	6.43±0.01	6.34±0.04
Si	7.47±0.01	7.51±0.03	7.53±0.01	7.48±0.06
Ca	6.27±0.04	6.34±0.04	6.29±0.02	6.31±0.12
Ti	4.93±0.01	4.95±0.05	4.91±0.03	4.95±0.06
Cr	5.57±0.03	5.64±0.04	5.64±0.01	5.61±0.09
Fe	7.45±0.01	7.50±0.04	7.45±0.01	7.49±0.03
Ni	6.19±0.04	6.22±0.04	6.20±0.01	6.23±0.07

As reported in Table 2.7, for the uncertainties of the abundance ratios [X/Fe], the σ_1 values were calculated by adding the σ_1 value of [Fe/H] and that of [X/H] quadratically. The σ_2 values instead were calculated in the same way as for [X/H].

2.4 Results and discussion

2.4.1 The Sun and the Gaia Benchmark stars

Firstly, I applied my new method to the GBS stars to determine its validity, and to the solar spectrum to derive the reference solar abundance scale. In Table 2.4 the values of the atmospheric parameters and abundances of Fe and Ti of both the GBS and the Sun are reported. The results obtained with the Ti+Fe approach are in excellent agreement with the results by Jofré et al. (2015b, 2018) and with *Gaia*-ESO, in particular for ξ (rows highlighted in yellow). The new ξ values are very similar to those obtained with Fe lines, which confirms our hypothesis that the *standard* spectroscopic analysis produces good results for older (and less active) stars ($\gtrsim$ 600 Myr).

In Table 2.8 the solar abundance scale (obtained with the atmospheric values reported in Table 2.4) is shown. The mean value between Fe I and Fe II for the final Fe abundance is reported, also for Ti. The uncertainties are the quadratic sum of the σ_1 and σ_2 contributions, computed as in Section 2.3.4. The solar abundances generally agree well with the results by Asplund et al. (2009), with the meteoritic results by Lodders et al. (2009), and also with the results of *Gaia*-ESO iDR5. Based on the study of Bergemann (2011) on the NLTE effects on Ti, the NLTE corrections for our lines that form at $\log(\tau_{5000}) \sim -1$ and at solar metallicities are negligible.

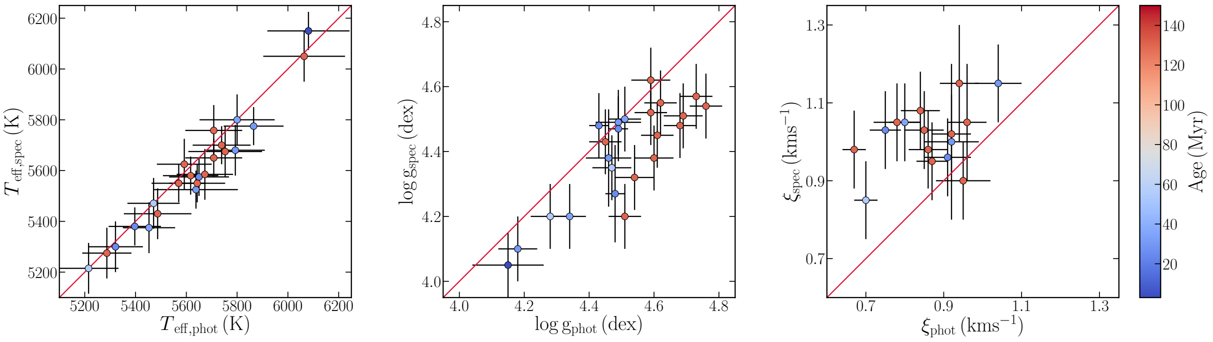

Figure 2.5: Comparison between the photometric and spectroscopic estimates of the atmospheric parameters. The red line represents the 1:1 relation. The points are colour-coded according to ages. The red points refer to NGC 2516, and the blue points to the younger clusters.

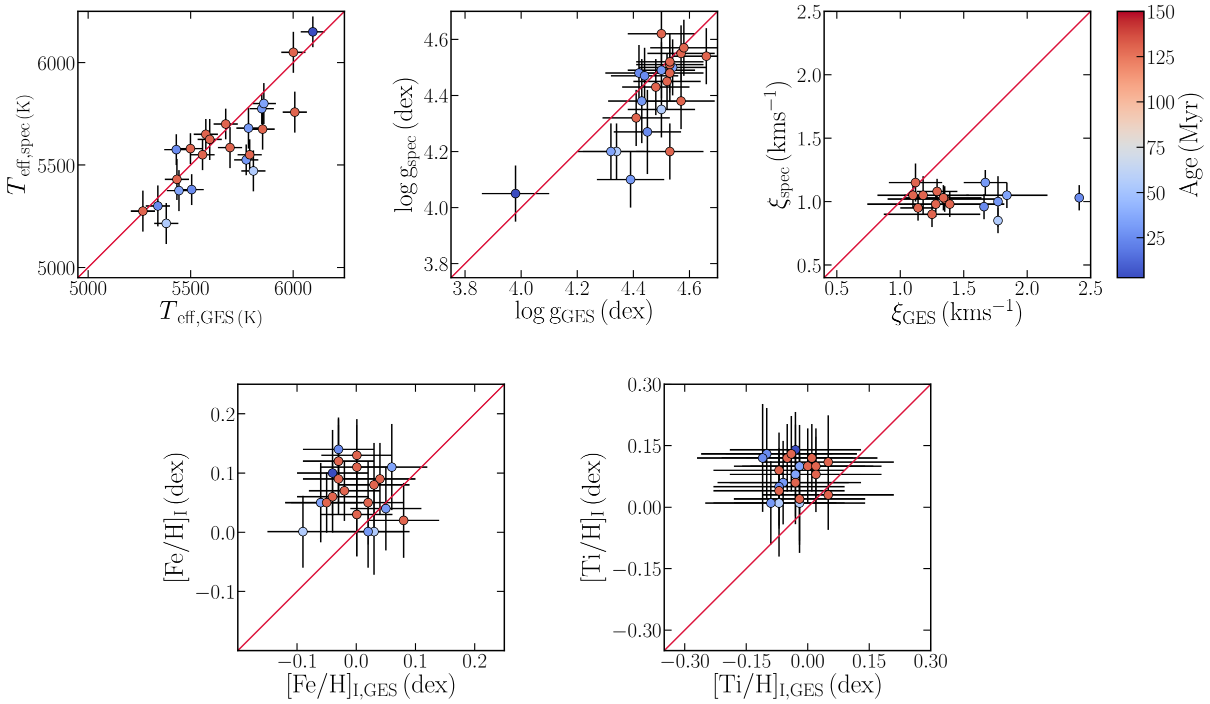

Figure 2.6: Comparison between the values of $T_{\mathrm{eff,spec}}$, $\log g_{\mathrm{spec}}$, ξ_{spec} , and [X/H] derived here with the values from *Gaia*-ESO iDR5. The red line represents the 1:1 relation. We exclude stars from the plot whose ξ value is fixed to the photometric estimates.

2.4.2 Stellar atmospheric parameters: comparison of photometry and spectroscopy

The atmospheric parameters inferred with the new method agree well with the photometric estimates (Figure 2.5, where the data are colour-coded according to age). The temperatures agree very well, with a mean difference of −37±49 K. There is a general offset of the $\log g$ values, with a difference of −0.11±0.09 dex: still, the ionisation equilibrium is valid (within the errors) for both Ti and Fe (Table 2.6). Regarding the ξ values, I find instead that the spectroscopic estimates are slightly larger than the photometric ones, but still comparable, with a difference of 0.15±0.10 km s^{-1}. I excluded from the comparison plots all stars whose ξ value was fixed to the photometric estimate. However, this offset between spectroscopic and photometric determinations of ξ is known in the literature and has also been observed in old stars. It is worth noting that if the values derived by *Gaia*-ESO ($\sim$ 2.0 km s^{-1}) are considered, the difference with the photometric estimates is even larger.

I compared my results of the atmospheric parameters, and the Fe and Ti abundances with those given in the *Gaia*-ESO iDR5 catalogue. The comparison plots are shown in Figure 2.6 (as in Figure 2.5, the data are colour-coded by age): my measurements of $T_{\rm eff}$ and $\log g$ (y-axis) are in fair agreement with *Gaia*-ESO. For $T_{\rm eff}$ the mean differences between our values and *Gaia*-ESO results is equal to −66±122 K. Instead, for $\log g$ I found $\Delta \log g = -0.07 \pm 0.11$ dex. We can conclude that my results are reliable and agree with those of *Gaia*-ESO, and also this suggests that the $T_{\rm eff}$ and $\log g$ are not so much influenced by the activity (it has also been confirmed by Yana Galarza et al. 2019 and Spina et al. 2020). This is also corroborated by the analysis of the GBS stars, even if these are older stars.

However, the largest differences are seen for the ξ parameter. My results are lower than those of iDR5: I find a mean difference of −0.46±0.36 km s^{-1}. A small mean difference like this can be explained by the fact that for the stars in NGC 2516 ($t \sim$ 130 Myr), I obtained values of ξ that agree with iDR5. The third panel in the top row in Figure 2.6 shows a net separation between younger OCs and older OCs (in this case, only NGC 2516, represented by the red points). The most dramatic effect of over-estimating the ξ value is seen in the youngest clusters. I calculated the mean differences separating the clusters with ages younger than 100 Myr and for NGC 2516 with ages older than 100 Myr. While the oldest cluster has a mean difference of −0.23±0.13 km s^{-1}, meaning that my results are comparable to the iDR5 results, for the youngest clusters the mean difference is equal to −0.85±0.27 km s^{-1}, which is significant at the 3σ level. These results support the original hypothesis that the standard analysis might over-estimate the ξ parameter for young stars, which , in turn, leads to an under-estimation of the element abundances, as it is shown in the bottom panels of Figure 2.6.

It is noteworthy that for the stars in NGC 2516 I derived a slightly higher metallicity than what was published by *Gaia*-ESO, although the ξ values are quite similar. In particular, even if the difference in ξ is smaller than the difference with the younger stars, the range covered by the difference in [Fe/H] is the same as for the younger stars. This can be explained as the result of small differences in the other photospheric parameters (e.g.

Table 2.9: Mean abundances and abundance ratios of each cluster.

	IC 2391	**IC 2602**	**IC 4665**	**NGC 2264***	**NGC 2516**	**NGC 2547**
[Fe/H]	0.04±0.01	0.04±0.01	0.12±0.02	0.11±0.02	0.08±0.01	0.10±0.01
[Ti/H]	0.02±0.01	0.03±0.01	0.11±0.03	0.19±0.09	0.09±0.01	0.10±0.01
[Na/Fe]	−0.03±0.02	0.02±0.01	0.04±0.03	0.06±0.04	−0.03±0.01	−0.005±0.004
[Mg/Fe]	0.02±0.02	−0.03±0.01	-	−0.02±0.04	−0.07±0.02	0.01±0.03
[Al/Fe]	0.03±0.02	−0.01±0.03	-	-	0.00±0.04	0.04±0.04
[Si/Fe]	0.00±0.01	0.01±0.03	0.03±0.02	−0.02±0.05	−0.02±0.01	−0.01±0.02
[Ca/Fe]	0.075±0.004	0.08±0.02	0.07±0.02	0.02±0.04	0.04±0.01	0.07±0.01
[Ti/Fe]	0.01±0.01	0.01±0.02	0.00±0.04	0.03±0.06	0.008±0.004	0.01±0.02
[Ti/Fe]$_{\rm II}$	−0.05±0.01	−0.02±0.01	−0.02±0.04	0.04±0.05	−0.01±0.01	−0.03±0.01
[Cr/Fe]	0.01±0.03	0.05±0.01	0.08±0.02	0.02±0.06	0.02±0.01	0.07±0.04
[Ni/Fe]	−0.04±0.02	0.023±0.003	0.06±0.01	0.00±0.02	0.03±0.01	0.03±0.02

* For this cluster we analysed only one star, therefore the uncertainty is the quadratic sum of σ_1 and σ_2.

100 K in temperature produces 0.07 dex in metallicity), to the use of different criteria in zeroing the trends in order to derive the photospheric parameters, to the use of different method, such as the spectral synthesis, and to differences in the EW measurements.

2.4.3 Element abundances

As already said, the final parameters and abundance ratios are reported in Tables 2.6 and 2.7. The mean values for each cluster are reported in Table 2.9, where the uncertainties represent the uncertainty on the mean, computed as the rms divided by the square root of the number of stars in the cluster (i.e., $\sigma/\sqrt{N_{stars}}$). In a few cases it was not possible to derive the abundances of some elements, such as Al I, because the lines were too weak to be measured or because of blending with nearby lines.

To evaluate the validity of my method, I determined the correlation between the derived abundances with T$_{\rm eff}$, as in Figure 2.7 for Fe and Ti and Figure 2.8 for the different [X/H] ratios. I also determined the trends between [X/H] and log g (Figure 2.9). In these Figures, the data are colour-coded according to the age, as for the previous plots. The α-, proton-capture and the iron-peak elements elements overall show solar abundances, as expected for these types of objects. We do not find any statistically meaningful trend, therefore my results are expected to be reliable.

Originally, the stellar sample included a few stars with $T_{\rm eff} \lesssim 5200$ K. For these stars I find discrepancies (differences larger than 0.8 dex) between abundances derived from Fe I and Fe II, as well as Ti I and Ti II. These can be explained with the so-called *overionisation effect*. It has been confirmed by different authors that dwarf stars with $T_{\rm eff} \lesssim 5200$ K show systematically larger Fe II abundances with respect to Fe I in clusters and in field stars (King et al. 2000; Chen et al. 2008; Schuler et al. 2010; Bensby et al. 2014). These

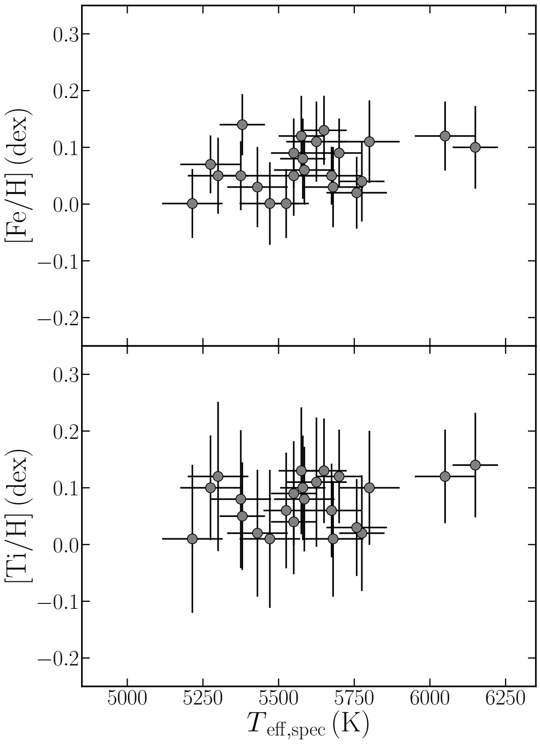

Figure 2.7: [Fe/H] (top panel) and [Ti/H] (bottom panel) as a function of $T_{\rm eff}$ derived using Fe and Ti lines simultaneously. For Fe, the Pearson correlation coefficient is r=0.35, with p=.10, which is not significant at $p < .05$. For Ti, the Pearson correlation coefficient is r=0.32, with $p = .14$, which is not significant at $p < .05$.

differences are stronger as $T_{\rm eff}$ decreases, and in particular as ages decreases, affecting dramatically the derived atmospheric parameters values, especially $\log g$. This is also valid for the Ti lines (see Fig.4 in D'Orazi et al. 2009a). According to the results reported by D'Orazi et al. 2009a, the overionisation effect reaches values up to +0.6 dex for stars with $T_{\rm eff}$ lower than 5000 K, difference which decrease with increasing $T_{\rm eff}$. overionisation (and/or overexcitation effects, observed in high-excitation potential lines of C or O, Schuler et al. 2015) drove the choice to restrict the analysis to star with $T_{\rm eff} \gtrsim 5200$ K.

Overall, the mean values of the abundances I obtained agree well with values found in literature. For IC 2391, IC 2602, IC 4665, and NGC 2516, our measurements in general confirm the results of different studies (De Silva et al. 2013, D'Orazi et al. 2009a, Shen et al. 2005, and Terndrup et al. 2002, respectively). For NGC 2264, King et al. (2000) derived abundances for three stars and obtained a mean metallicity of −0.15±0.09. The authors studied two stars with $T_{\rm eff} < 5000$ K and one star that was similar to the Sun: they derived $T_{\rm eff}$ and ξ with the standard spectroscopic analysis, but they fixed log g to the value estimated from the isochrones. Their Table 1 lists ξ values of the order of ~2.0 kms^{-1}, which most likely causes the Fe abundances to become sub-solar.

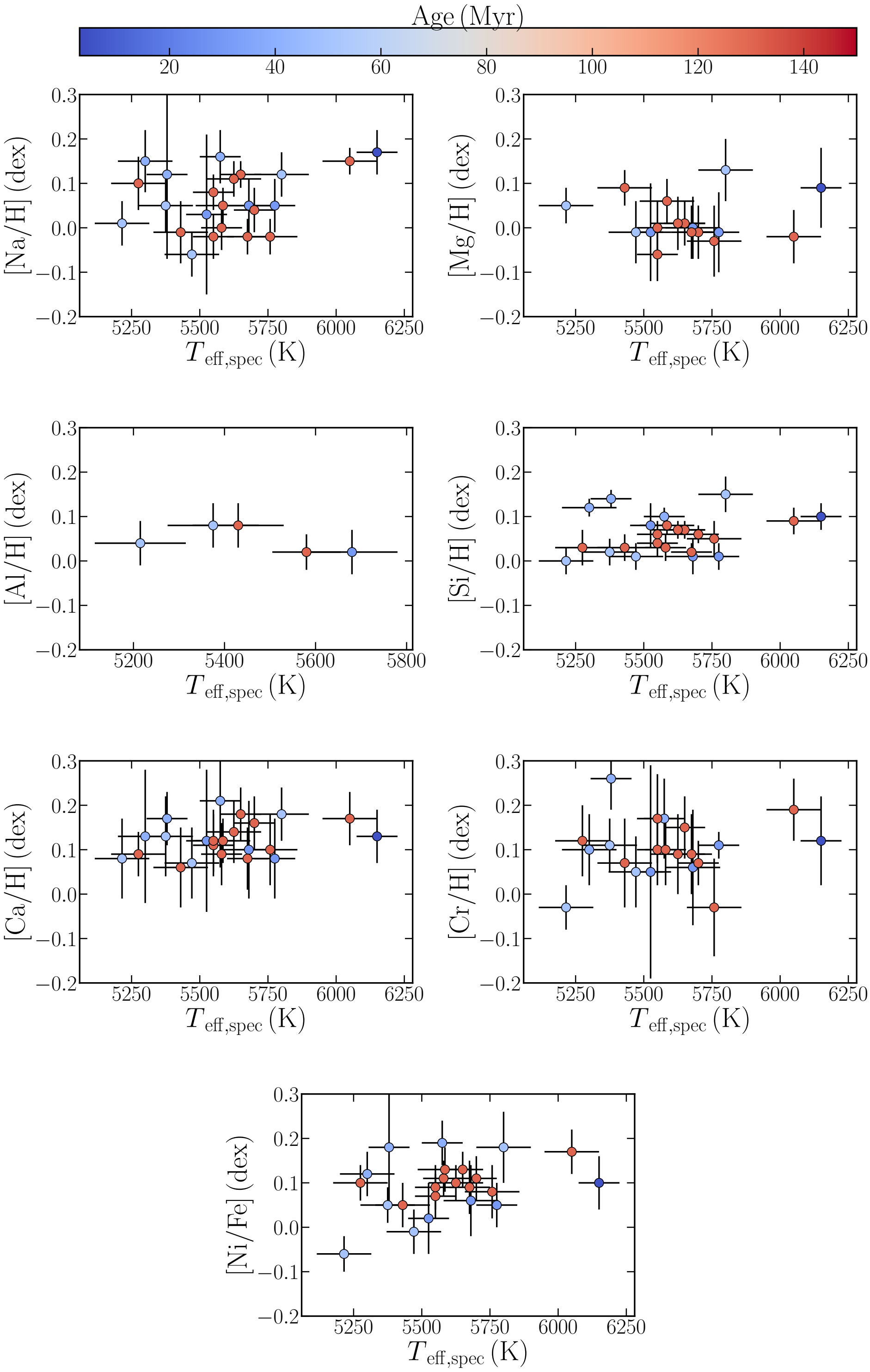

Figure 2.8: [X/H] as function of T_{eff}, derived with the new method and colour-coded according to age.

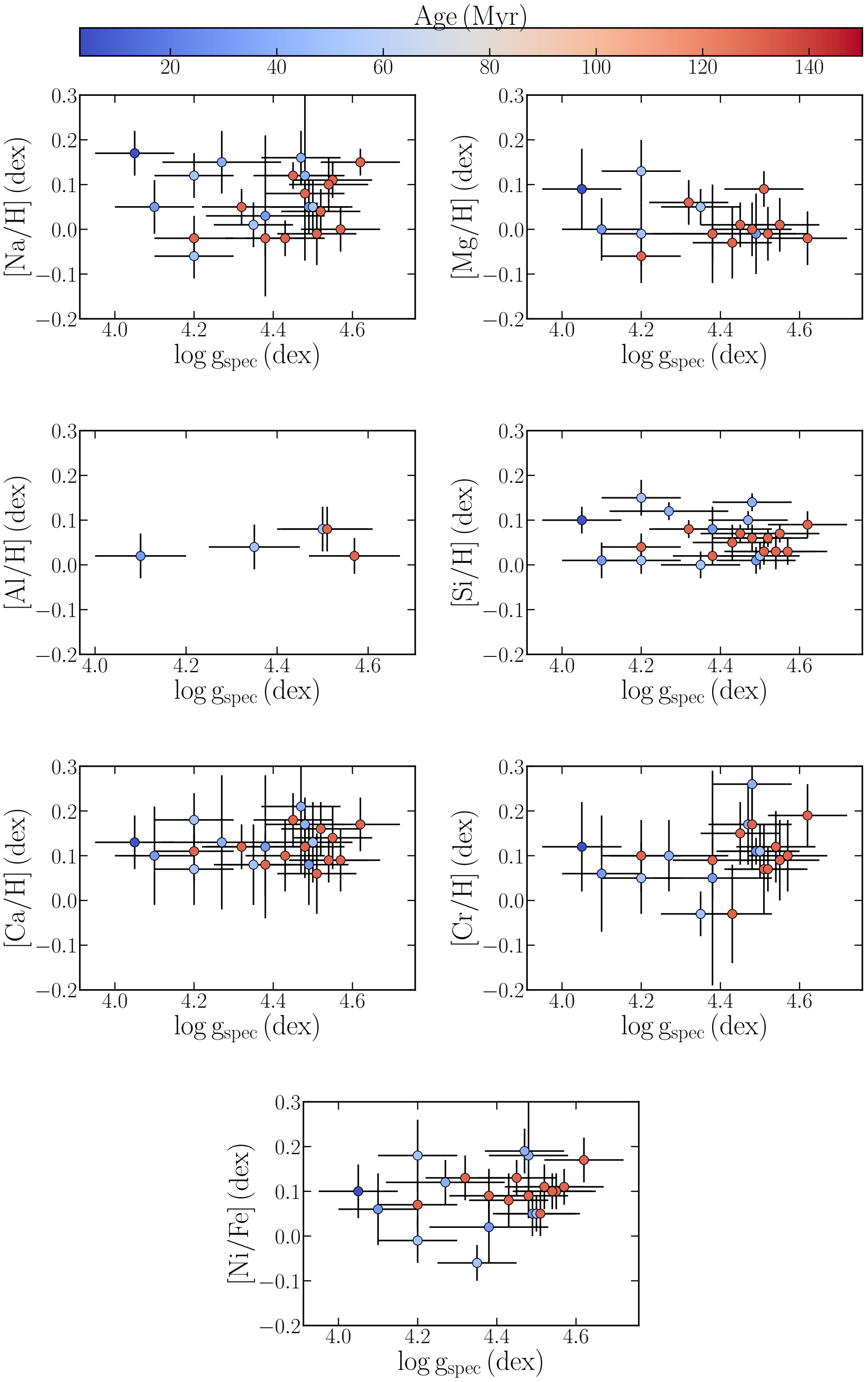

Figure 2.9: [X/H] as function of log g, derived using only Ti lines and colour-coded according to age.

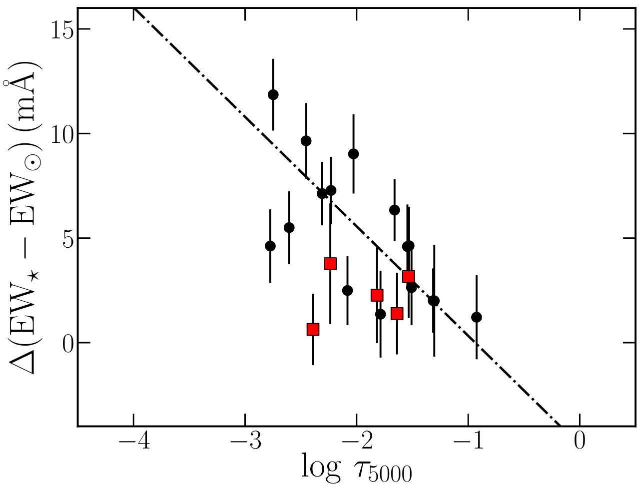

Figure 2.10: Difference between the EWs of the Fe (black dots) and Ti (red dots) lines measured in the solar-analogue star 10442256−6415301 (30 Myr) and the Sun as a function of the optical depth of line formation log τ_{5000}. The dot-dashed line is the trend for Fe lines.

2.4.4 The impact of stellar activity

To analyse the effect of stellar activity on Fe lines, I studied the dependence of the Fe line EWs on optical depth log τ_{5000}, taken from Gurtovenko & Sheminova (2015). In Figure 2.10, I plot the difference of the EWs (y-axis) of the Fe (black) and Ti (red) lines computed between a solar analogue (star 10442256−6415301 belonging to IC 2602, with an age of 30 Myr) and the Sun as a function of the optical depth (x-axis). The solar analogue has $T_{\rm eff}$ = 5775 ± 75 K and log g = 4.49 ± 0.10 dex, with solar metallicity. It is clear from the Figure that lines forming in the upper layers of the atmosphere (log $\tau_{5000} < -2.5$) in the young star are systematically stronger (i.e., they have larger EWs) than in the Sun, with differences up to 5-10 mÅ. The linear trend for the Fe lines has a Pearson correlation coefficient $r = -0.85$ and is significant at $p < 0.01$. This means that the presence of these strongest lines can influence the derivation of the ξ parameter when it is derived from Fe lines.

I also analysed the dependence of the ξ parameter on the chromospheric activity index, namely log $R'_{\rm HK}$. Since this index cannot be directly measured from the available spectra (because the spectral coverage does not include the Ca II H&K lines), I used the conversion relation found in Mamajek & Hillenbrand (2008), which takes the log $(L_{\rm X}/L_{\rm bol})$ activity index into account. I found in the literature values for 14 of the 23 stars we analysed. Figure 4.11 shows that while my measurements (black triangle) do not display a significant trend with activity, the ξ values measured by *Gaia*-ESO (i.e., with the *standard* analysis; grey dots) instead increase at increasing log $R'_{\rm HK}$, that is, at an increasing level of activity. In this Figure, I also report the values for the GBS I analysed (coloured triangles). The benchmarks are *old and quiet* stars, with log $R'_{HK} < -4.8$, and I obtain the same value as Jofré et al. (2015b) with the new approach, as reported in Table 2.4. I also note that the ξ value of β Hyi is slightly higher than the values obtained for the other benchmark stars, which is mainly due to the slightly advanced evolutionary stage.

Yana Galarza et al. (2019) and Spina et al. (2020) recently studied the effects of stellar activity on the line formation, proposing that the magnetic intensification could be responsible of the larger EWs measured in active stars, as it has been theoretically studied by several authors (Fabbian et al. 2010; Shchukina & Trujillo Bueno 2015; Shchukina et al. 2016; Rosén et al. 2016).

In the first study, the authors analysed HARPS spectra of a 400 Myr solar analog (HIP 36515) taken along the ∼ 6 yr of its activity cycle. They derived the stellar parameters in six different epochs along the total activity cycle, and most importantly, they observed variations of the EW of Fe lines along the activity cycle, and with optical depth. In particular they found that weak lines (EWs< 40 mÅ) with different Landè factors behave similarly: in particular, these lines will not affect the derivation of the stellar parameters, with variations of 6 K in $T_{\rm eff}$, 0.01 in log g, 0.02 km s^{-1} in ξ and finally 0.002 in [Fe/H]. Instead, the lines with EW larger than 40 mÅ(moderate-strong lines) are affected the most, showing significant variations in their strengths as they are formed at small log τ_{5000} (so up in the photosphere). The authors also found that lines that form at the same log τ_{5000} but with large Landè factors ($g_{\rm L} > 1.5$) show the largest variations of EWs. These lines will then dominate the trend and will affect the derivation of the stellar parameters: the authors found that $T_{\rm eff}$ changes by 27 K along the cycle (that is significant when compared to the internal precision of 15 K they found) and changes of almost 0.15 km s^{-1} on ξ that could explain the decrease of [Fe/H].

Spina et al. (2020) expanded the same investigation to a larger sample of Sun-like stars (211) observed at different phases of their activity with HARPS. For each star, they measured the EWs of lines of different elements, they derived the stellar parameters and abundances (in the *standard* way), and analysed the possible correlations with the activity. They found that some lines (for example the Ba II line at 5853.7 Å, but in general for all the lines with EW> 50 mÅ) are clearly stronger when the activity is at maximum. The increase of EW could be due to the Zeeman effect, which overall produces a splitting of the line into multiple components. According to their analysis, stars with log $R'_{HK} > -5.0$ (thus younger than the Sun, Lorenzo-Oliveira et al. 2018) are most affected by this phenomenon, that reflects also on the derivation of the stellar parameters. Indeed, Spina et al. (2020) found that $T_{\rm eff}$, metallicity and mircoturbulence varies strongly in stars with larger values of log R'_{HK}, thus more active, especially for log $R'_{HK} > -5.0$.

However, the analysis performed by Yana Galarza et al. (2019) and Spina et al. (2020)

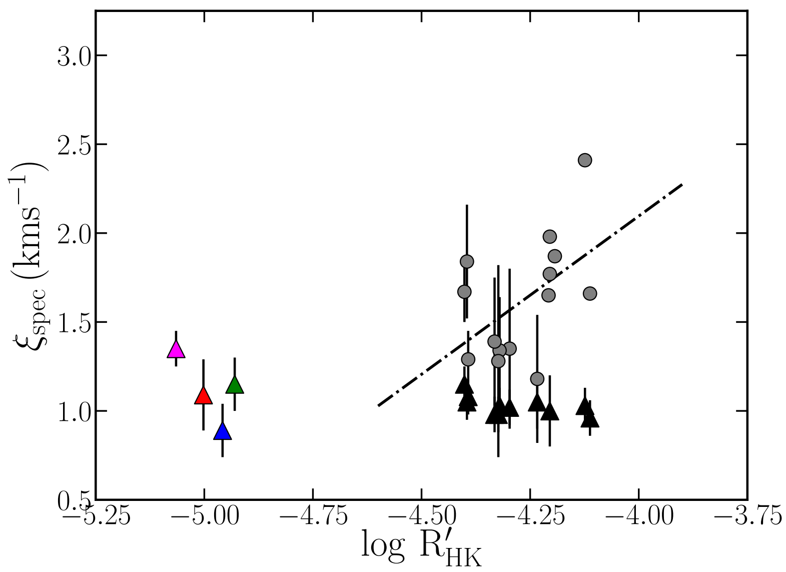

Figure 2.11: Activity index log R$'_{\rm HK}$ as a function of ξ values: the GESiDR5 results are represented with grey circles, and the triangles represent the values we find with our new method. The black triangles are the stars in the sample, and the coloured triangles represent the Gaia benchmark stars: red for α Cen A, green for 18 Sco, blue for τ Cet, and magenta for β Hyi. The dot-dashed line is the trend observed for the GES values.

involved stars that are older (t ∼400-600 Myr, and with log R$'_{\rm HK}$ from −5.4 to −4.4) than those in my sample, which have ages lower than 150 Myr and log R$'_{\rm HK}$ between −4.5 and −4.0. The conclusion we can drawn are the same: the activity alter the formation of spectral lines, affecting the derivation of the stellar parameters and ultimately the abundances. However, as it will be explained in the following Chapters, the inclusion of magnetic intensification at such young ages could not be sufficient to explain the anomalous behaviour of spectral lines since different, conspiring mechanisms could be simultaneously at work.

2.4.5 The Galactic metallicity distribution

What are the implications in the Milky Way galaxy framework? As already mentioned in Chapter 1, the slight metal-poor nature of the nearby youngest population could be only apparent and not real. In light of the new results, I plot the metallicity distribution as a function of the open cluster age in Figure 2.12, where the empty circles represent the clusters in Netopil et al. (2016) for which high-quality determination of metallicity are available (Heiter et al. 2014) and with $7.5 < R_{\rm gal} < 9$ kpc. The coloured stars represent the clusters I have analysed with the new determination of [Fe/H]. The empty stars represent the analysed clusters with the values of metallicity derived with the *standard* analysis. The blue triangles represent the *Gaia*-ESO clusters analysed in Magrini et al. (2018)

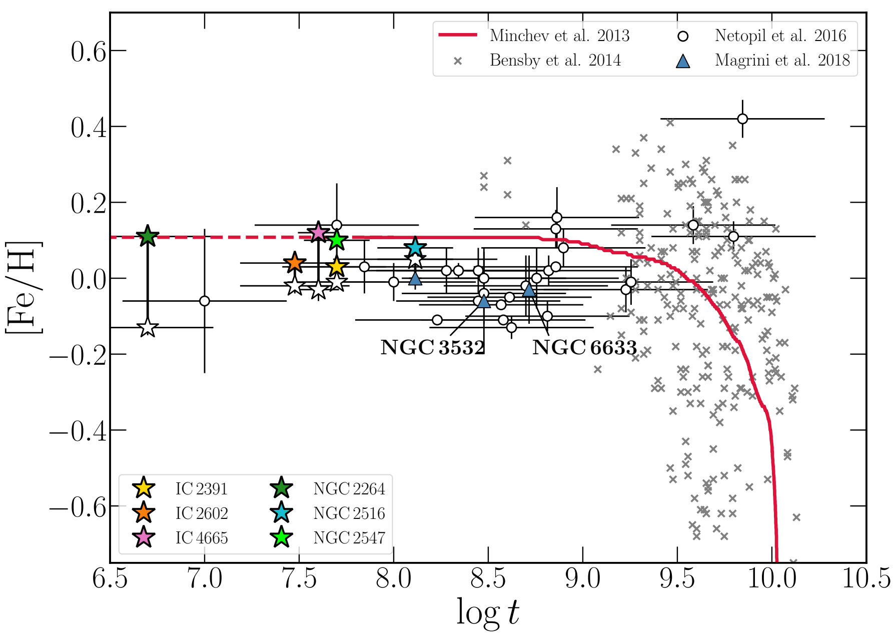

Figure 2.12: Age-metallicity distribution for the YOCs we analysed here, for the sample of Netopil et al. (2016) (empty circles), field stars taken from Bensby et al. (2014) (grey crosses), and *Gaia*-ESO clusters analysed in Magrini et al. (2018) (filled triangles). The red line represents the model by Minchev et al. (2013) for 7.5< R_{Gal} < 9 kpc. See text for further details. The empty stars represent the clusters we analysed whose metallicity was derived with the standard analysis (Netopil et al. 2016).

(intermediate-age and old clusters), for which I take the median [Fe/H] value reported in the same paper. In the case of NGC 2264, I consider the age estimate by Venuti et al. (2018) (in contrast with the estimate by Netopil et al. 2016, who reported 10±10 Myr), both for my new metallicity estimate and the value obtained with the *standard* analysis. The grey crosses, instead, represent the field stars taken from Bensby et al. (2014), from which I selected only thin-disc stars, those with TD/D<0.5, where TD is the probability of being a thick-disc star, and D corresponds to the probability of being a thin-disc star. A more detailed description of these parameters can be found in the Appendix A in Bensby et al. (2014). Also, I excluded those field stars with a difference between the upper and lower age limit that is larger than 4 Gyr, in order to exclude stars with large age uncertainties.

When considering the new estimates of the abundances and the model for the solar vicinity developed by Minchev et al. (2013) (red line), no peculiar chemical evolution of the Galaxy seems required. The model of Minchev et al. (2013) does not extend to ages younger than ~ 60 Myr, as already noted by Spina et al. (2017). However, an enrichment of nearly 0.10-0.15 dex at R_{Gal} of 7.5-9 kpc in the last 4-5 Gyr is expected. We might also expect the model to extend to the present time with a flat, continuous behaviour, but very likely not towards sub-solar metallicities, as the *standard* spectroscopic analysis seems to suggest instead. All of my new estimates of [Fe/H], ranging from 0.04 to 0.12 dex, lie within the predictions of the Galactic chemical evolution model. It is also worth noting that the sample of Netopil et al. (2016) lies lower than that predicted by the theoretical model. There is no conclusive explanation for this behaviour: it might be the combination of different factors, for example, the use of the standard analysis, but also the fact that the metallicity determinations in Netopil et al. (2016) are a combination of different heterogeneous studies.

2.5 Conclusions

In this Chapter I have described a new approach to deriving the stellar atmospheric parameters. I analysed a sample of 23 dwarf stars observed in five Galactic YOCs and one SFR that are included in the *Gaia*-ESO survey.

In particular, for a young cluster star an EW analysis that only uses Fe I lines returns a value for the ξ parameter that is too high, as shown by the model lines, which are too strong compared to the observed lines. This indicates that the derived Fe line abundances depend on the optical depth of line formation, as suggested by Reddy & Lambert (2017). I also confirmed that this effect is weak in old stars, as I showed for the GBS, for which I obtained the same results as Jofré et al. (2015b, 2018) and *Gaia*-ESO.

The new method consists of a combination of Fe and Ti lines to derive $T_{\rm eff}$ by zeroing the trend between the individual line abundances and the E.P. For $\log g$ and the ξ parameter, *only* Ti lines are employed to avoid possible complications due to the use of Fe lines, because these form in a wider range of optical depth and the strongest lines can be affected by the higher levels of activity of the superficial photospheric layers. The comparison with *Gaia*-ESO iDR5 results showed that while for $T_{\rm eff}$ and $\log g$ I obtained comparable measurements, a most dramatic effect is seen for ξ. Overall, I note an overestimation of this parameter, with the largest differences seen for clusters younger than 100 Myr.

I also investigated the effect of stellar activity. In Section 4.11 I reported that the difference between EWs measured in a young (30 Myr) solar analogue and the Sun is larger for lines that form in the outer layers of the atmosphere. Figure 2.10 showed that lines forming at $\log \tau_{5000} < -2.5$ are stronger in the young star when compared with the values measured in the Sun. This might cause higher values of the ξ parameter when it is derived with Fe lines. I also found a dependence of the ξ values on the chromospheric activity index $\log \mathrm{R}'_{\rm HK}$, which is stronger for the GES iDR5 results than for the values I derived with the new approach. This also confirms that for the GBS, which are quiet stars, I obtained the same values with both methods.

In the Galactic framework, as described in Section 2.4.5, the new estimates of [Fe/H] place well within the theoretical predictions of the Galactic chemical evolution model by Minchev et al. (2013). It seems that no peculiar chemical evolution of the Galaxy is needed to reproduce the metallicity distribution.

Finally, the revised metallicities might also affect the isochrone-derived ages of very young stars. Redder or cooler stars mimic younger ages if a higher metallicity is assumed. The isochrone-based ages may therefore be slightly different when this is performed for stars whose colour-magnitude diagram depends on [Fe/H].

Similar results have been confirmed in other two independent studies, Yana Galarza et al. (2019) and Spina et al. (2020). As already discussed by Spina et al. (2020), we still do not know what is the main mechanism behind the anomalous behaviour of spectral lines observed in very young stars (even if we cannot firmly state at which age these effects start to be more prominent). We can overcome these issues with a strategic choices of the master line list used in the spectroscopic analysis, like the solution proposed by Spina et al. (2020), or the new approach proposed in Baratella et al. (2020b). This latter could be further improved, by for example looking at Cr lines, since the stellar spectrum is also rich in this lines. A 3D analysis could also be effective. However, these results surely draw the attention to the need of revisiting the spectroscopic analysis when applied to very young stars. And of course this is of primary importance especially for the large spectroscopic surveys and for the data-driven techniques.

CHAPTER 3

The GAPS Programme at TNG

XXV. Stellar atmospheric parameters and chemical composition through GIARPS optical and near-infrared spectra

Based on:
Baratella M., D'Orazi V., Biazzo K., et al., 2020, A&A, Volume 640, id.A123, 15 pp.

The detailed chemical composition of stars is important in many astrophysical fields, among which is the characterisation of exoplanetary systems. Previous studies seem to indicate an anomalous chemical pattern of the youngest stellar population in the solar vicinity that has sub-solar metal content. This can imply that in these systems is less favorable to search for Jupiter-like planets, given the well established giant planet-metallicity correlation. In this framework, we aim to expand our knowledge of the chemical composition of intermediate-age stars and understand whether these peculiarities are real or related to spectroscopic analysis techniques. In this Chapter, I analyse high-resolution optical and near-infrared spectra of intermediate-age stars (< 700 Myr) that have been observed within the GAPS program with HARPS-N coupled with GIANO-B spectrograph in GIARPS mode. To overcome issues related to the young ages of the stars, I apply the new spectroscopic method presented in Chapter 2 to the optical spectra and I derive abundances of C I*, Na* I*, Mg* I*, Al* I*, Si* I*, Ca* I*, Ti* I*, Ti* II*, Cr* I*, Cr* II*, Fe* I*, Fe* II*, Ni* I*, and Zn* I*. The abundances of some of these elements have been derived also from GIANO-B spectra. The lack of systematic trends between elemental abundances and effective temperatures validates the methods. However, the coolest stars in the sample, where $T_{\rm eff} < 5400$ K, display higher abundances for the ionised species, in particular Cr* II*, and for high-excitation potential C* I *optical lines. A positive correlation between the higher abundances measured of C* I *and Cr* II *and the activity index $\log R'_{\rm HK}$ is confirmed. Instead, no correlations between the C abundances obtained from CH molecular band at 4300Å and both effective*

temperatures and activity have been found. Thus, I suggest that CH is a better indicator of C abundance, especially in the coolest regime. Finally, I find an indication of an increasing abundance ratio [X/H] with the condensation temperature for HD 167389, suggesting possible episodes of planet engulfment.

3.1 Introduction

As already shown in the previous Chapter, the spectroscopic analysis of young stars (< 200 Myr) is not trivial. The presence of active chromospheres and/or intense surface photospheric magnetic fields (Folsom et al. 2016) may alter the formation of spectral lines, affecting the derivation of the stellar parameters and the chemical abundances.

The precise determination of the atmospheric parameters and chemical composition of stars is important especially for exoplanetary studies. First, we are interested in understanding the main observational correlations between the properties of exoplanets and the characteristics of their host star. These correlations include the giant planet-metallicity relation (how are giant planet formed?) and the trends observed between the condensation temperature (Tc) and abundances ratios [X/Fe] (do stars engulf planets?). See the latest results by Nissen 2015; Brewer et al. 2016; Adibekyan 2019 and references therein for a complete review on the subject. Thus, it is important to determine accurately the abundances of the various elements.

However, it has been observed that young (< 200 Myr) and cool ($T_{\rm eff} \lesssim 5400$ K) stars display anomalous abundances of oxygen O I triplet (χ = 9.15 eV) and sulfur (S I line at 6053Å with χ = 7.87 eV) (Schuler et al. 2004; Teske et al. 2013; Ramírez et al. 2013). In particular, the abundances increase at decreasing $T_{\rm eff}$, reaching values of 0.8-1.0 dex over solar for the coolest dwarfs ($T_{\rm eff}$ ~4700 K). Together with carbon C I, O is particularly important for the planetary formation models. Thus, deriving reliable estimates of C/O ratio is crucial since it provides clues to where the planets formed in the protoplanetary disc and possible subsequent radial migration (Brewer et al. 2017).

Similarly, for the same kind of stars and in the same $T_{\rm eff}$ regime, differences between the neutral and ionised species of the same element of the order of +0.8 dex have been observed for Fe and Ti (Schuler et al. 2006; D'Orazi et al. 2009a). Such differences can produce unreliable results, in particular for the derivation of log g, which should be decreased in order to satisfy the ionisation equilibrium. These effects may be caused either by non-local thermodynamic equilibrium (NLTE) departures, for which the high-energy levels are not correctly modelled, or by the presence of unidentified blends (see also Tsantaki et al. 2019), or a combination of both. Aleo et al. (2017) argue that the large differences between Fe I and Fe I may be related to blending of Fe II lines that become more severe at decreasing $T_{\rm eff}$. These results were corroborated by Takeda & Honda (2020), who also concluded that the O I overabundance obtained from the oxygen triplet by Schuler et al. (2006) might be due to the different $T_{\rm eff}$ scale and to over-estimation of the strength of the lines in coolest stars. However, the possibility that these effects might be related to the stellar activity cannot be discarded.

Along with the increasing number of stellar spectra available thanks to the large spectroscopic surveys, the need arose to assess the precision and accuracy of spectroscopic analysis techniques (Jofré et al. 2019). Until recently, the study of stellar spectra mainly involved the analysis of data in the optical band, covering the wavelength range from ~4000 to ~7000 Å. However, the advent of high-resolution near-infrared (NIR) spectroscopy allowed us to extend the analysis of stellar spectra at longer wavelengths as well, and to test the validity of optical and NIR analysis techniques (Marfil et al. 2020). This is particularly important in the study of young and intermediate-age stars, for which stellar activity and other effects can alter the derivation of atmospheric parameters and, specifically, the chemical composition.

For five years, the Global Architecture of Planetary Systems (GAPS) project (Covino et al. 2013; Poretti et al. 2016) searched for planets through a radial velocity (RV) technique with High Accuracy Radial velocity Planet Searcher for the Northern emisphere (HARPS-N; Cosentino et al. 2014) at Telescopio Nazionale Galileo (TNG, Roque de los Muchachos, La Palma) around different types of stars, including the characterisation of selected planet-host stars. Recently, a new phase of the project started with the aim of exploiting the full capabilities of the GIARPS mode (Claudi et al. 2017). This means that we can study and fully characterise planetary systems by analysing GIAno-B (Oliva et al. 2006) and haRPS stellar spectra acquired simultaneously. In this context, the GAPS Young Objects (GAPS-YO) group (Carleo et al. 2020) aims to monitor and study young ($<$ 100 Myr) and intermediate-age ($<$ 700 Myr) stars to search for and characterise hot and warm planets down to sub-Neptune mass in formation or at an early stage of their evolution.

Within the GAPS-YO goals, and in light of the results I showed in the previous Chapter, my new spectroscopic approach became the main strategy adopted by the stellar characterisation team to analyse the observed young targets. In this Chapter, I will present the results obtained from GIARPS spectra of the Sun, two RV standard stars (HD 3765 and HD 15922), and seven more stars members of intermediate-age stellar clusters and moving groups (ages less than ~ 600 Myr). In Section 3.2 I present the collected data and some information on the selected stars. My analysis is separated between the optical and NIR spectral ranges. In particular, in Section 3.3 I describe the new method applied to derive atmospheric parameters and elemental abundances from optical spectra. These parameters were used to derive abundances of neutral C, Na, Mg, Al, Si, Ca, Ti, Fe, and Ni from NIR spectral lines, presented in Section 3.4. In Section 3.5 I present the resulting chemical abundances of various atomic species and the comparison with literature. In Section 3.6 instead I discuss extensively the derivation of C abundance and the effects of stellar activity. Finally, in Section 3.7 I present the conclusions.

3.2 The GAPS-YO targets and spectroscopic data

High-resolution spectra of seven young and intermediate-age stars observed within the GAPS-YO project have been analysed. The spectra were selected with high signal-to-noise ratios (S/N), low rotational velocities ($v \sin i < 15 \mathrm{km\,s^{-1}}$) to avoid line blending, and with spectral type FGK. Stars with spectral type later than K were excluded from the analysis to avoid problems with the molecular bands, which become more important as the temperature decreases.

The selected targets are: TYC 1991 − 1235 − 1, HIP 61205, TYC 1989 − 0049 − 1, and TYC 1989 − 147 − 1, which belong to the Coma Berenices OC (Mermilliod et al. 2008), with an age of ~600 Myr; HD 167389 and HD 59747, which are part of the Ursa Major moving group (Montes et al. 2001), with an age of ~500 Myr; and HD 70573 of Hercules Lyra moving group (López-Santiago et al. 2006), with an age of ~200 Myr. I also analysed, for validation, the spectra of two old stars observed as RV standard stars, HD 3765 and HD 159222. Some basic information on the targets could be found in Table 3.1: the SIMBAD ID are reported in Column 1; right ascension (RA) and declination (Dec) in Columns 2 and 3, respectively; the spectral type (SpT) is in Column 4; V and 2MASS (Cutri et al. 2003) magnitudes in the J, H and K bands are reported in Column 5, 6, 7 and 8; the distances, taken from Bailer-Jones et al. (2018) are reported in Column 9; ages (Column 10) and rotational velocities $v \sin i$ (Column 11) are taken from different sources in literature, as indicated in the Table notes; the activity indexes log $\mathrm{R'_{HK}}$ are in Column 12 (see Sec. 3.6.1 for the details of the computation).

The spectra were acquired with HARPS-N and GIANO-B spectrographs placed at the 3.6 m INAF-Telescopio Nazionale Galileo (TNG) in La Palma. The HARPS-N spectrograph is the northern counterpart of HARPS at the La Silla Observatory (Chile), mounted at the Nasmyth-B focus of the TNG. With a resolving power R~115 000 and large wavelength coverage in the optical range (0.38-0.69 μm), it allows us to obtain very precise (less than 1 $\mathrm{m\,s^{-1}}$) RV measurements, thanks to an accurate control system that minimises pressure and temperature variations and prevents spectral drifts due to environmental conditions. The GIANO-B spectrograph is a high-resolution (R~45 000-50 000)

Table 3.1: Basic information of both standard stars and members in young associations analysed in this Chapter.

SIMBAD ID	RA (J2000)	Dec (J2000)	SpT	V (mag)	J (mag)	H (mag)	K (mag)	d^a (pc)	Age (Gyr)	$v \sin i$ (km s^{-1})	$\log R'_{HK}$
HD 3765	00 40 49.27	+40 11 13.82	K2	7.344	5.694	5.272	5.164	17.94±0.03	4.94±6.56	2.6^e	−4.94±0.01
HD 159222	17 32 00.99	+34 16 16.13	G1	6.595	5.342	5.076	4.998	24.22±0.01	3.24±1.48	3.01^f	−4.88±0.01
					Coma Berenices						
TYC 1991-1235-1	12 28 56.43	+26 32 57.39	K5	10.971	9.208	8.768	8.661	84.14±0.33	0.56 ± 0.09^b	3.5 ± 1.2^g	−4.41±0.05
HIP 61205	12 32 31.07	+35 19 52.31	G0	9.635	8.407	8.132	8.086	83.41±0.32	0.56±0.09	6.4 ± 0.9^i	−4.43±0.02
TYC 1989-0049-1	12 21 15.62	+26 09 14.05	K3	11.483	9.614	9.087	8.972	84.71±0.29	0.56±0.09	1.4 ± 2.8^g	−4.17±0.02
TYC 1989-147-1	12 24 05.73	+26 07 42.92	K0	10.461	9.081	8.762	8.611	88.67±0.31	0.56±0.09	5.0 ± 0.9^g	−4.55±0.01
					Ursa Major						
HD 167389	18 13 07.23	+41 28 31.31	F8	7.453	6.224	5.968	5.918	34.72±0.03	0.5 ± 0.1^c	3.5 ± 0.5^l	−4.78±0.02
HD 59747	07 33 00.58	+37 01 47.45	G5	7.797	6.090	5.662	5.589	20.68±0.02	0.5±0.1	2.6 ± 0.5^h	−4.37±0.02
					Hercules Lyra						
HD 70573	08 22 49.95	+01 51 33.55	G1	8.711	7.558	7.276	7.191	59.28±0.16	0.25 ± 0.05^d	13.5 ± 0.5^m	−4.31±0.02

a) Bailer-Jones et al. (2018); b) Silaj & Landstreet (2014); c) Montes et al. (2001); d) Eisenbeiss et al. (2013);e) Luck (2017); f) Martínez-Arnáiz et al. (2010); g) Mermilliod et al. (2009); h) Marsden et al. (2014); i) Mermilliod et al. (2008); l) Valenti & Fischer (2005); m) Gonzalez et al. (2010)

NIR spectrograph covering the wavelength range from 0.95 μm to 2.45 μm that is placed at Nasmyth-B focus of the TNG. The configuration of the two spectrographs allows us to observe the stars simultaneously in the optical and NIR wavelengths in the GIARPS mode. We analysed GIARPS spectra of the Sun, HD 3765, HD 159222, TYC 1991 − 1235 − 1, HIP 61205, and HD 167389. Instead, for the other targets, the GIANO-B spectra are not available, and only the optical spectra were analysed.

HARPS-N data are reduced with the standard Data Reduction Software (DRS). Since the spectra were collected by the GAPS-YO collaboration to obtain time series for RV monitoring, the available HARPS-N data for each target were then combined to obtain a co-added spectrum with S/N $>$ 100 (Malavolta et al. 2016). This procedure do not introduce any systematic errors, thanks to the high stability of the instrument over several months.

The NIR data reduction was performed with the pipeline GOFIO (Rainer et al. 2018; Harutyunyan et al. 2018), while the telluric correction was performed following the method described in Carleo et al. (2016). For GIANO-B spectra I considered the highest S/N observation (S/N>70) for each star. Since the analysis is differential with respect to the Sun, I derived the solar abundance scale by analysing the HARPS-N and GIANO-B spectra of Ganymede, which have a S/N = 145 at 607 nm and S/N = 180 at 1500 nm, respectively.

3.3 Optical analysis

The HARPS-N optical spectra were analysed to derive the stellar atmospheric parameters and the chemical composition of the targets. I applied the new spectroscopic approach presented in Chapter 2 given the relatively young age of the stars. I used the code MOOG[1] (version 2017, Sneden (1973); Sobeck et al. (2011)) under the assumption of local thermodynamic equilibrium (LTE). I estimated the abundances of C i, Na i, Mg i, Al i, Si i, Ca i, Ti i, Ti ii, Cr i, Cr ii, Fe i, Fe ii, Ni i, and Zn i using the EW method by running the *abfind* driver. I adopted the same line list used in D'Orazi et al. (2020) that includes 86 Fe i lines, 17 Fe ii lines, 57 Ti i lines, 22 Ti ii lines, and 42 more lines of different atomic species. The complete line list is published in Baratella et al. (2020a). Two C i lines (specifically lines 5380.34 and 6587.61 Å) have been added to the original line list, taking into account the atomic data from Amarsi et al. (2019). The Barklem prescription for damping values was adopted (see Barklem et al. 2000 and references therein).

The EWs for all lines were measured with the software ARESv2 (Sousa et al. 2015)[2], which calculates EWs through a Gaussian fitting of the line. Lines with fitting errors larger

---

[1] https://www.as.utexas.edu/ chris/moog.html

[2] http://www.astro.up.pt/ sousasag/ares/

Table 3.2: Solar abundances derived from the analysis of HARPS-N and GIANO-B spectra. The values from Asplund et al. (2009) (A09) are also reported for comparison.

Species	HARPS-N	GIANO-B	A09
C I	8.45±0.04(NLTE)	8.38±0.10	8.43±0.05
Na I	6.21±0.04(NLTE)	6.24±0.04	6.24±0.04
Mg I	7.63±0.04	7.59±0.01	7.60±0.04
Al I	6.49±0.03	6.45±0.03	6.45±0.03
Si I	7.54±0.02	7.52±0.01	7.51±0.03
Ca I	6.35±0.05	6.36±0.01	6.34±0.04
Ti I	4.97±0.02	4.98±0.01	4.95±0.05
Ti II	4.98±0.04	-	
Cr I	5.65±0.04	-	5.64±0.04
Cr II	5.66±0.05	-	
Fe I	7.49±0.03	7.51±0.01	7.50±0.04
Fe II	7.48±0.04	-	
Ni I	6.24±0.04	6.22±0.02	6.22±0.04
Zn I	4.55±0.01	-	4.56±0.05

than 10% and those lines with EWs>120 mÅ were discarded. In this way, the strong lines (for which the Gaussian approximation might not be adequate) have been removed form the analysis. The 1D model atmospheres linearly interpolated from the ATLAS9 grid of Castelli & Kurucz (2003), with new opacities (ODFNEW), were adopted.

The input values of the $T_{\rm eff}$ and of surface gravities ($\log g$) were estimated as in the previous Chapter. Briefly, the $T_{\rm eff}$ estimates were obtained via 2MASS photometry with the calibrated relation by Casagrande et al. (2010) valid for $(J-K)$ de-reddened colours. In this calibrated relation, the input metallicity was assumed to be solar, which was later confirmed by the chemical abundances analysis. The initial values of the surface gravities (trigonometric gravities, $\log g_{\rm \ trig}$) were estimated using the classical equation, based on Gaia DR2 distances as calculated by Bailer-Jones et al. (2018) (see Table 3.1). Instead, at variance with Baratella et al. (2020b) the initial values of ξ were derived using the relation by Dutra-Ferreira et al. (2016), calibrated for dwarf stars, that is:

$$\xi(km\ s^{-1}) = 0.998 + 3.16 \times 10^{-4}\, X - 0.253\, Y - 2.86 \times 10^{-4}\, X\, Y + 0.165 Y^2 \qquad (3.1)$$

where $X = T(J-K) - 5500\,(\rm K)$ and $Y = \log g - 4.0$ (dex). This is because the *Gaia*-ESO relation used in the previous Chapter is valid for stars with $T_{\rm eff} > 5200\,$K: here, instead cooler stars are analysed.

For the Sun, I obtained $T_{\rm eff}$ =5790±75 K, $\log g$ =4.40±0.05 dex and ξ=0.93±0.05 km s^{-1} for the spectroscopic atmospheric parameters. The solar abundances of each element are reported in Table 3.2, where the uncertainties are the quadratic sum of the uncertainty due to EWs measurements (σ_1) and due to the contribution of the atmospheric parameters (σ_2). As shown, the solar abundances are in very good agreement with those derived by Asplund et al. (2009).

The final values of stellar atmospheric parameters, as well as the input estimates, and the derived abundances of neutral and ionised Fe and Ti for the two standard and the seven target stars in our sample are reported in Table 3.3. The final abundance ratios [X/Fe] are reported in Table 3.4 and they have been computed as $[\mathrm{X/Fe}]=[\mathrm{X/H}]_\star-[\mathrm{Fe/H}]_\star$ (in particular, for the ionised species $[\mathrm{X/Fe}]_{\mathrm{II}} = [\mathrm{X/H}]_{\mathrm{II}}-[\mathrm{Fe/H}]_{\mathrm{II}}$). For star HD 70573, the derivation of the abundances of C and Al was hampered by the relatively high $v \sin i$. Moreover, the analysis of HD 3765 was not trivial. We derived spectroscopically T_{eff} =5001±75 K, but if the ionisation equilibrium was satisfied for Ti, this was not the case for Fe and Cr. In particular, I obtained a difference of +0.11 and +0.18 dex between ionised and neutral Fe and Cr species, respectively. The same issue was raised by Ramírez et al. (2007), who obtained a difference between Fe I and Fe II of +0.18 dex. Since the ionisation equilibrium is not satisfied for Fe, the [X/H] values of each element for star HD 3765 are reported in Table 3.4. Moreover, I also obtained an anomalously large value of [C/H]=+0.36±0.05±0.09 dex. Similar values of carbon abundances were also obtained for the other cool stars in our sample. This behaviour is discussed extensively in Section 3.6.

3.4 Near-infrared analysis

The GIANO-B spectra were acquired for HD 3765, HD 159222, TYC 1991 − 1235 − 1, HIP 61205 and HD 167389. The NIR abundances were measured through spectral synthesis via the driver *synth* in MOOG.

In general the number of lines of the ionised atomic species is significantly lower in the NIR than in the optical part of the spectrum. Thus, for this reason, I used the atmospheric parameters derived from the analysis of HARPS-N spectra and derived the abundances of Na I, Mg I, Al I, Si I, Ca I, Ti I, Fe I, and Ni I with the spectral synthesis. The line list from D’Orazi et al. (2020) was adopted, and one C I line was added to the original line list, the 16021.7 Å line, for which atomic data were taken from Shetrone et al. (2015).

Briefly, a spectral region of 1000 Å was synthesised and the best instrumental profile was determined, taking into account the resolution of GIANO-B and the $v \sin i$ values listed in Table 3.1. Then, I focussed on the line of interest and I derived the given abundance with 0.1 dex steps to find the best-fit profile that minimises the sum of the squared residuals between the synthetic and the observed spectra. In Table 3.2 the mean values ob-

Table 3.3: Input values of the atmospheric parameters and results of the spectroscopic analysis of HARPS-N spectra for the stars in our sample. The derived abundances of Fe and Ti are also reported, where the uncertainties are σ_1 and σ_2, which are due to the EW measurements and to the atmospheric parameters, respectively.

ID	$T_{\rm eff,phot}$ (K)	$\log g_{\rm trig}$ (dex)	ξ (km s^{-1})	$T_{\rm eff,spec}$ (K)	$\log g_{\rm spec}$ (dex)	$\xi_{\rm spec}$ (km s^{-1})	[Fe/H]$_{\rm I}$ (dex)	[Fe/H]$_{\rm II}$ (dex)	[Ti/H]$_{\rm I}$ (dex)	[Ti/H]$_{\rm II}$ (dex)
						Standard stars				
HD3765	5111±92	4.56±0.02	0.79±0.04	5001±75	4.56±0.10	0.59±0.20	0.02±0.01±0.08	0.13±0.03±0.09	0.14±0.01±0.11	0.13±0.02±0.06
HD159222	5863±111	4.41±0.05	1.03±0.04	5900±75	4.43±0.05	1.03±0.10	0.14±0.01±0.06	0.12±0.02±0.04	0.09±0.01±0.07	0.08±0.01±0.03
						Coma Berenices				
TYC 1991-1235-1	5040±108	4.62±0.04	0.77±0.04	5070±70	4.53±0.05	0.87±0.12	−0.05±0.01±0.04	−0.03±0.03±0.07	−0.03±0.01±0.09	−0.02±0.02±0.04
HIP 61205	5972±114	4.58±0.02	1.05±0.04	5825±50	4.52±0.05	1.05±0.10	−0.04±0.01±0.04	−0.03±0.02±0.03	−0.06±0.01±0.05	−0.05±0.01±0.03
TYC 1989-0049-1	4718±76	4.73±0.02	0.67±0.04	4718±50	4.61±0.05	0.63±0.07	−0.06±0.02±0.03	0.01±0.04±0.07	0.00±0.02±0.07	0.02±0.03±0.03
TYC 1989-147-1	5333±100	4.66±0.03	0.85±0.04	5313±50	4.51±0.05	0.80±0.10	−0.05±0.01±0.04	−0.01±0.03±0.05	−0.04±0.01±0.06	−0.02±0.02±0.04
						Ursa Major				
HD 167389	6038±140	4.51±0.02	1.07±0.04	6000±75	4.55±0.05	1.07±0.15	0.01±0.01±0.06	0.00±0.02±0.04	0.03±0.01±0.07	0.02±0.02±0.04
HD 59747	5206±110	4.71±0.02	0.81±0.04	5106±50	4.58±0.05	0.73±0.10	−0.02±0.01±0.03	−0.01±0.03±0.05	0.01±0.01±0.06	0.02±0.02±0.03
						Hercules Lyra				
HD 70573	5755±129	4.43±0.03	1.00±0.04	5800±75	4.40±0.07	1.10±0.10	−0.03±0.02±0.09	0.02±0.02±0.07	−0.02±0.02±0.10	0.00±0.02±0.06

Table 3.4: Abundance ratios obtained from the optical analysis. The two uncertainties in the abundances are σ_1 and σ_2, which are related to the EW measurements and atmospheric parameters, respectively.

[X/Fe]	HD3765*	HD159222	TYC 1991-1235-1	HIP 61205	TYC 1989-0049-1	TYC 1989-147-1	HD 167389	HD 59747	HD 70573
[C/Fe]	−0.07±0.10±0.09	−0.16±0.12±0.07	−0.12±0.15±0.07	−0.05±0.11±0.06	−0.06±0.20±0.09	−0.10±0.15±0.07	0.08±0.09±0.07	−0.12±0.12±0.08	-
[Na/Fe]$_{\rm NLTE}$	0.11±0.01±0.07	0.00±0.02±0.03	−0.05±0.04±0.04	−0.04±0.02±0.06	−0.15±0.07±0.08	−0.12±0.03±0.14	−0.05±0.02±0.14	−0.08±0.03±0.06	−0.02±0.04±0.03
[Mg/Fe]	0.12±0.01±0.05	−0.01±0.05±0.02	0.01±0.02±0.01	−0.06±0.01±0.10	−0.11±0.04±0.19	−0.02±0.02±0.04	−0.03±0.03±0.06	−0.02±0.02±0.03	−0.02±0.03±0.05
[Al/Fe]	0.24±0.01±0.05	0.06±0.01±0.11	0.02±0.03±0.04	0.01±0.03±0.14	0.00±0.04±.03	0.00±0.01±0.01	−0.03±0.03±0.06	0.03±0.03±0.06	-
[Si/Fe]	0.08±0.03±0.03	−0.02±0.01±0.07	0.00±0.02±0.05	−0.05±0.02±0.09	0.00±0.03±0.04	−0.01±0.01±0.05	−0.05±0.02±0.10	0.00±0.01±0.04	0.00±0.04±0.04
[Ca/Fe]	0.14±0.02±0.07	−0.01±0.03±0.02	0.06±0.01±0.12	0.04±0.03±0.07	0.09±0.02±0.17	0.04±0.01±0.08	0.06±0.03±0.10	0.07±0.03±0.13	0.08±0.04±0.13
[Ti/Fe]$_{\rm I}$	-	−0.04±0.01±0.16	0.03±0.01±0.10	−0.02±0.01±0.10	0.06±0.03±0.12	0.01±0.01±0.10	0.01±0.01±0.13	0.03±0.01±0.09	0.00±0.02±0.13
[Ti/Fe]$_{\rm II}$	-	−0.04±0.02±0.07	0.01±0.06±0.09	−0.03±0.02±0.08	0.01±0.04±0.09	−0.01±0.04±0.07	0.02±0.03±0.06	0.03±0.04±0.15	−0.03±0.03±0.08
[Cr/Fe]$_{\rm I}$	0.16±0.02±0.08	−0.01±0.01±0.01	0.05±0.02±0.11	0.02±0.01±0.04	0.09±0.03±0.17	0.02±0.02±0.06	0.02±0.01±0.05	0.10±0.01±0.19	0.04±0.05±0.09
[Cr/Fe]$_{\rm II}$	0.34±0.02±0.08	0.01±0.04±0.02	0.07±0.06±0.14	0.04±0.04±0.06	0.14±0.06±0.25	0.07±0.03±0.12	−0.01±0.07±0.04	0.14±0.04±0.27	0.04±0.05±0.06
[Ni/Fe]	0.13±0.02±0.03	−0.01±0.01±0.02	0.00±0.02±0.03	−0.07±0.01±0.12	0.02±0.04±0.05	−0.04±0.02±0.07	−0.06±0.01±0.10	−0.01±0.01±0.03	0.03±0.04±0.04
[Zn/Fe]	0.04±0.03±0.05	0.00±0.01±0.05	0.03±0.02±0.06	0.03±0.02±0.05	0.01±0.05±0.03	0.04±0.02±0.06	−0.06±0.02±0.15	0.04±0.04±0.05	0.03±0.05±0.03

* For HD 3765, the [X/H] values are reported, since Fe does not satisfy the ionization equilibrium. The [Ti/H] values are reported in Table 3.3.

Table 3.5: Mean values of the [X/H] ratios derived from the NIR analysis for four stars in our sample.

[X/H]	HD3765	HD159222	TYC 1991-1235-1	HIP 61205	HD 167389
C	0.11±0.10±0.08	0.18±0.09±0.06	−0.03±0.15±0.09	0.02±0.12±0.06	-
Na	-	0.20±0.08±0.06	-	-	−0.10±0.10±0.07
Mg	0.15±0.02±0.07	0.13±0.03±0.06	−0.02±0.01±0.08	−0.03±0.03±0.06	0.01±0.03±0.07
Al	0.25±0.08±0.09	0.22±0.10±0.08	0.03±0.12±0.08	0.00±0.12±0.08	-
Si	0.12±0.03±0.06	0.04±0.04±0.05	0.00±0.03±0.06	0.02±0.02±0.06	−0.01±0.01±0.05
Ca	0.16±0.07±0.07	0.10±0.03±0.04	0.02±0.02±0.09	0.06±0.09±0.05	0.08±0.03±0.06
Ti	0.15±0.10±0.06	0.09±0.09±0.05	0.00±0.10±0.07	0.05±0.08±0.06	−0.05±0.07±0.06
Fe	0.11±0.05±0.08	0.17±0.09±0.07	−0.04±0.06±0.07	−0.02±0.04±0.06	−0.01±0.07±0.06
Ni	0.15±0.06±0.08	0.20±0.08±0.06	0.00±0.12±0.06	0.00±0.09±0.07	0.05±0.11±0.05

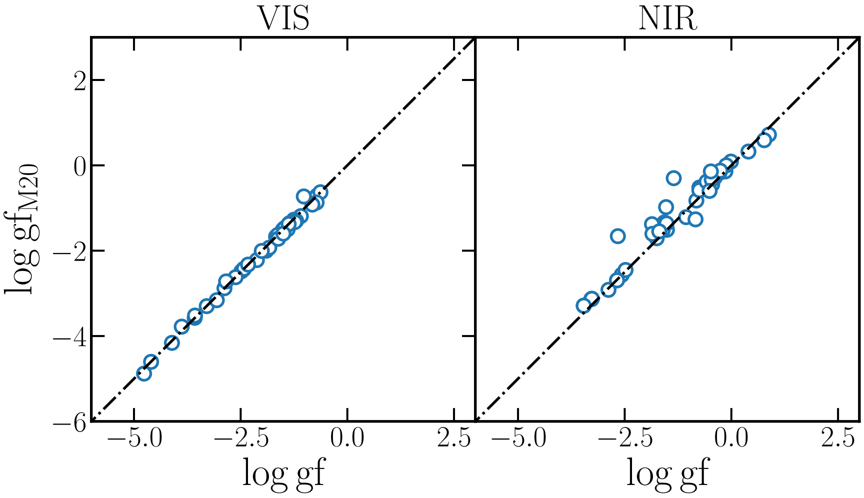

Figure 3.1: Comparison of $\log gf$ between our line lists (x-axis) and those used in M20 (y-axis).

tained from the NIR analysis of the solar spectrum are reported in Column 3. As it can be seen, the agreement with the optical values is extremely good, also validating the results of the atmospheric parameters obtained from the optical analysis. The final abundances for the stars for which I analysed GIANO-B spectra are reported in Table 3.5. For C, Na, Al, and Mg, I measured only one line, so the uncertainties σ_1 and σ_2 on the abundances in the Table account for the uncertainties on the fitting procedure and the sensitivity of [X/H] to changes in the atmospheric parameters, respectively. Instead, for the remaining elements for which more than one line were measured, I reported the mean values of the abundances, where σ_1 is the error on the mean and σ_2 related to the atmospheric parameters, respectively.

Recently, Marfil et al. (2020) (hereafter M20) analysed CARMENES spectra of a sample of FGK stars (wavelength coverage between 5200-17100 Å and R=95 000 and R=80 000 in the optical and NIR channel, respectively) with the EWs method, using an extended line list that also comprises Fe I and Fe II lines in the NIR part (216 and 1 lines, respectively) to assess the impact of the NIR lines on the derived stellar parameters. I compared the log gf values of the adopted line list and those of the authors and I find that the values are nearly the same, as shown in Figure3.1. The mean difference between the derived values and those found in M20 is +0.02±0.08 for optical and −0.13±0.26 for NIR; thus it is expected to obtain the same results as M20. I applied to our solar spectrum the same procedure and the same line list (the one that the M20 authors optimised for metal-rich dwarfs) as in M20. Since the wavelength coverage of CARMENES spectrograph is different than that of by HARPS-N and GIANO-B, we measured a total of 165 Fe I and Fe I lines adopted from M20 in the solar spectrum, in particular 125 lines in VIS and 40 lines in NIR. The analysis of optical+NIR spectra produced $T_{\rm eff}$ =5790±50 K, log g =4.50±0.10 dex, ξ=0.70±0.10 km s^{-1}, with log(Fe I)=7.53±0.01±0.04 and log(Fe II)=7.54±0.05±0.04. These values are very similar to what obtained from the optical analysis alone and using our line list. The M20 authors, instead, find nearly the same $T_{\rm eff}$ and log g, but ξ=1.31±0.09 km s^{-1}. I derived the atmospheric parameters applying the same criteria as the code STEPAR (Tabernero et al. 2019) and I found $T_{\rm eff}$ =5750±75 K, log g =4.40±0.05 dex and ξ=0.77±0.15 km s^{-1}. Such a large discrepancy of the ξ values could be mainly due to the EW measurements of lines in the NIR. The NIR may pose a challenge when it comes to measuring EWs: for example, telluric lines in emission that remain after the correction, which that the placement of the continuum and a variable S/N ratio that is smaller at shorter wavelengths (Marfil, priv. comm.). Thus, it is possible that there is significant differences between the EWs I measured and those measured in M20 and these differences may be responsible for the discrepancy in ξ values.

3.5 Discussion

3.5.1 Stellar parameters and elemental abundances

The atmospheric parameters for all the stars in the sample, as well as abundances of Fe I, Fe II, Ti I, and Ti II, are reported in Table 3.3. All the abundance ratios obtained from the optical analysis are reported in Table 3.4. Given the relatively wide range in $T_{\rm eff}$ of our targets, NLTE corrections were applied to Na and C abundances derived from the optical range, following the prescriptions given by Lind et al. (2011) and Amarsi et al. (2019), respectively. The final NIR abundances and uncertainties are reported in Table 3.5.

The input estimates of the stellar parameters ($T_{\rm eff}$ $_{\rm ,phot}$, log g $_{\rm ,trig}$ and ξ, in Column 2, 3, and 4 of Table 3.3) agree very well with the values derived spectroscopically ($T_{\rm eff}$ $_{\rm ,spec}$, log g $_{\rm ,spec}$ and $\xi_{\rm spec}$, in Column 5, 6, and 7 of Table 3.3). The mean difference be-

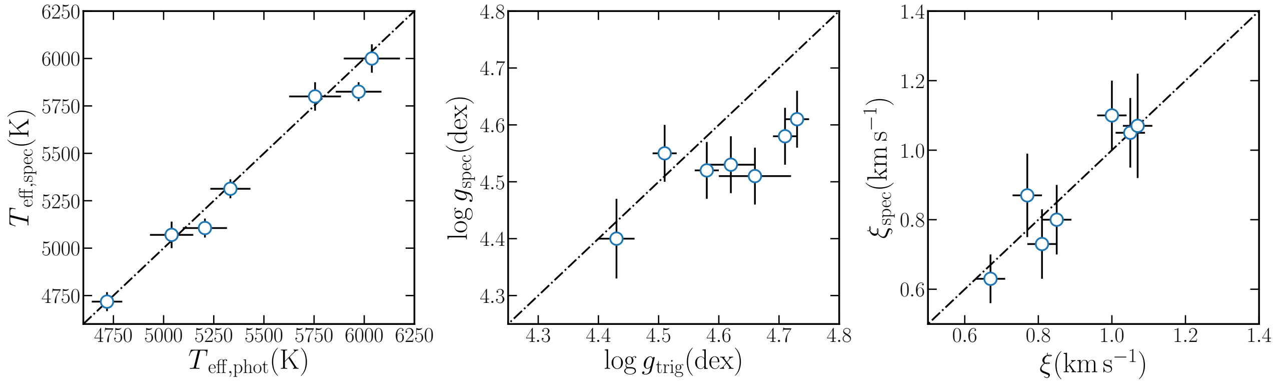

Figure 3.2: Comparison between the input estimates of the atmospheric parameters and the derived spectroscopic values. The dash-dotted line represents the 1:1 relation.

tween the initial guesses and the final spectroscopic values for each parameter was computed: the temperatures are in excellent agreement, with $\Delta T_{\rm eff}$=33±64 K. For the comparison between the spectroscopic and trigonometric gravities, I find a mean difference of −0.08±0.06 dex. As already noted by several authors (Sozzetti et al. 2007; Tsantaki et al. 2013; Maldonado et al. 2015), the spectroscopic gravities tend to be under-estimated with respect to the trigonometric values, especially for $\log g > 4.50$ dex, where $T_{\rm eff} < 5000$ K. This is again a manifestation of the ionisation balance problem affecting cool dwarf stars, that is enhanced as the stellar age decreases. As an additional check, for the stars with significant difference between spectroscopic and trigonometric gravities, the Gaia DR2 astrometric solutions[3] (including the parallax) are all well behaved, based on the reduced unit weight error (RUWE) metric (see e.g. Lindegren et al. 2018). This further argues for the discrepancy arising because of above-mentioned limits in the spectroscopic measurements. Finally, regarding the ξ values, I find a mean difference of −0.004±0.066 km s^{-1}.

In Figures 3.3 and 3.4, the abundances of the different elements are displayed as a function of $T_{\rm eff}$: the open symbols refer to the values we obtained from the optical analysis, while the red symbols represent the results from the NIR analysis. In particular, the diamond symbol is TYC 1991 − 1235 − 1, the star symbol stands for HIP 61205, and the pentagon symbol represents HD 167389. The lack of systematic trends between the derived optical abundances and $T_{\rm eff}$ estimates validates the derivation of the atmospheric parameters. I computed the Pearson correlation coefficient for all the trends in the two figures: none of these is statistically significant at p-value < 0.1 with the exception of Cr II. Despite the low [Mg/H] value obtained for TYC 1989 − 0049 − 1, equal to −0.17±0.03±0.04, the trend [Mg/H] versus $T_{\rm eff}$ has a Pearson correlation coefficient

---

[3] This work has made use of data from the European Space Agency (ESA) mission *Gaia* (`https://www.cosmos.esa.int/gaia`), processed by the *Gaia* Data Processing and Analysis Consortium (DPAC, `https://www.cosmos.esa.int/web/gaia/dpac/consortium`). Funding for the DPAC has been provided by national institutions, in particular the institutions participating in the *Gaia* Multilateral Agreement.

r=0.548, and p=0.2 . For this star only HARPS-N spectra are available, so the optical value could not be compared this low value with the NIR estimate. The abundance were obtained for the line 4730Å for which NLTE corrections for the Sun are of the order of 0.01 dex, as calculated by Zhao et al. (2016). The 5711Å line is strong in the spectrum of this star, and it has an EW of 143 mÅ. According to the initial selection criteria, it was excluded from the line list for the derivation of the abundance. The NLTE corrections for a star such as TYC 1989 − 0049 − 1 are very small, of the order of −0.006 dex (Osorio et al. 2015) and the NLTE corrections of the line 4730Å are expected to be of the same order.

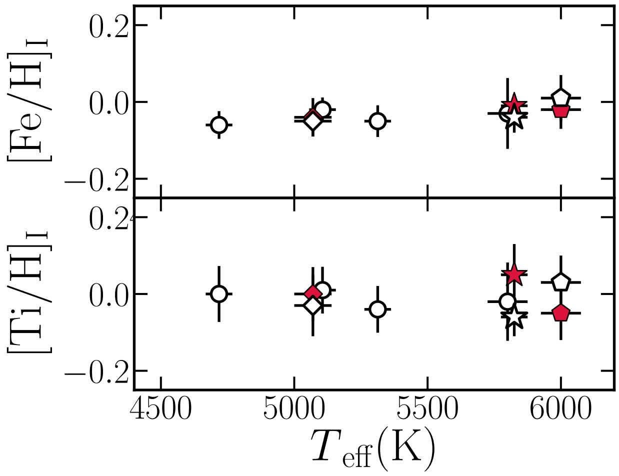

Figure 3.3: Abundances of Fe I and Ti I as function of $T_{\rm eff}$. The open symbols represent the optical measurements, while the red symbols indicate the NIR measurements. The diamond indicates TYC 1991−1235−1, the star symbol represents HIP 61205, and the pentagon denotes HD 167389, for which we have both optical and NIR measurements. The Pearson correlation coefficient of the trend in the top panel is r=0.67, which is not significant at p <0.1. For Ti the Pearson correlation coefficient is r=−0.03, which is not significant at p <0.1.

The ionization equilibrium is satisfied for Ti and also for Fe for the stars in our sample, as it can be seen in Table 3.3. Interestingly, this is not true for Cr, for which an anti-correlation with $T_{\rm eff}$ is found. As shown in Figure 3.4, the Cr II abundances increase at decreasing $T_{\rm eff}$, especially for stars with $T_{\rm eff} \lesssim$5400 K. This is explained with the overionisation effect. Differences between the neutral and ionised species for some elements, such as Fe, Ti, and Cr, have been observed in cool dwarfs with $T_{\rm eff} \lesssim$ 5400 K (King et al. 2000; Ramírez et al. 2007; D'Orazi et al. 2009a; Schuler et al. 2010). These differences can reach values up to 0.6-0.8 dex in stars younger than 100 Myr and consequently the value of log g should be decreased. The over-ionization effect is seen in cool dwarf stars, both in OC stars and in field stars (Bensby et al. 2014; Tsantaki et al. 2019). This effect is also observed in the cool ($T_{\rm eff}$ =5001 K) standard star HD 3765 (age ∼ 5 Gyr). While

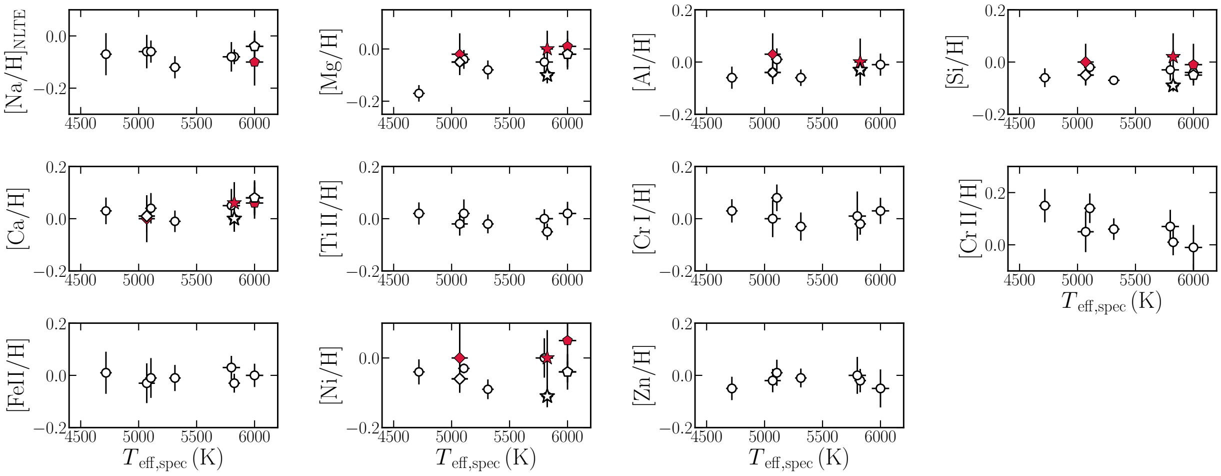

Figure 3.4: Individual values of [X/H] as a function of spectroscopic estimates of $T_{\rm eff}$, derived from the analysis of the optical spectra (open symbols) and from the analysis of NIR spectra (red symbols). The symbols for the three stars for which we analysed GIARPS spectra are the same as in Fig. 3.3 . All trends have Pearson correlation coefficients that are not significant at p <0.1, apart from Cr II (see the text for details).

the ionisation equilibrium is satisfied for Ti, suggesting a good estimate of log g for this star, I find a large discrepancy between Fe I and Fe II of about +0.11 dex, as already noted in Ramírez et al. (2007). A similar discrepancy is also seen for the Cr abundances, for which a difference of +0.18 dex between Cr I and Cr II is obtained, as shown in Table 3.4. In the analysis, two Cr II lines that are not blended with known contaminants (according to Lawler et al. 2017) are used. Notice that the NIR Fe abundance is in agreement with the Fe II estimate in the optical range. The reason for such observed discrepancies is still unknown: this may be due to the limitations of 1D-LTE model atmospheres, 3D effects, stellar activity, or a combination of these.

The agreement between the optical and NIR abundances for the stars is overall good, within the uncertainties. My results corroborate the previous findings of Caffau et al. (2019), who derived chemical abundances for different species of 40 disc stars by analysing spectra from GIANO in its previous configuration (fibre-fed). The authors compared the NIR abundances with those derived from the optical analysis fior 8 atomic species, among which Fe, Al, Si, Ca, Ti and Ni, and found a very good agreement (see their Table 2). However, for the star HIP 61205 that I have analysed, I obtained larger discrepancies for Mg, Si and Ni between the optical and NIR abundances; the latter values are nearly solar. Such discrepancies could be related to the different number of lines used to derive the abundances: more in the optical range (16 lines) than in the NIR (1 line).

In Figure 3.5, the abundance ratios [X/H] are plotted as a function of the condensation

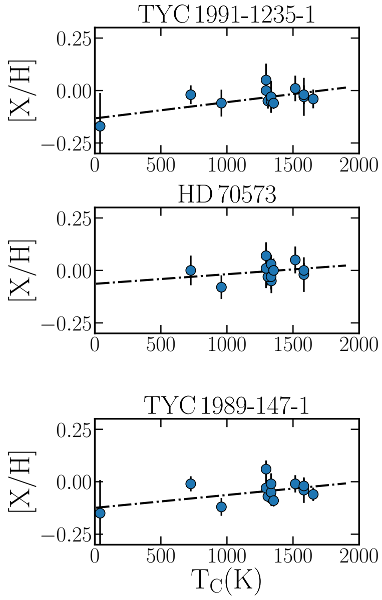

Figure 3.5: Values of [X/H] as a function of the condensation temperature T_C, taken from Lodders (2003).

temperature T_C, taken from Lodders (2003). Given the wide range in T_{eff} covered by the stars (~1500 K), I could not perform a strictly differential analysis with respect to stars of the same association and with similar T_{eff} (see e.g. Meléndez et al. 2009, 2014). For each trend the Pearson and Spearman correlation coefficients were computed and I find that the trend is significant at $p < 0.05$ in both cases for HD 167389 alone. It has been suggested that the positive slopes observed in [X/H]-T_C plots might be the result of accretion onto the star of refractory material present in the circumstellar disc or a signature of planet engulfment episodes. Instead, for the other stars, the correlation coefficients are not in agreement; thus no exhaustive conclusions can be drawn in those cases.

3.5.2 Comparison with the literature

The final abundance measurements are in overall fair agreement with other studies found in the literature, as shown in Table 3.6, where the mean values for each cluster and results from different studies are reported. Regarding the Coma Berenices cluster, my measurements are in good agreement with Blanco-Cuaresma et al. (2015) for all the atomic species. Netopil et al. (2016) report a mean [Fe/H] equal to 0.00±0.08, averaging over different estimates in the literature. Other studies on the chemical composition of this cluster are mainly focussed on the analysis of AF type stars that have temperatures higher than 6000 K. Burkhart & Coupry (2000) reported a mean [Fe/H]=−0.07 ± 0.05 dex for 1 F-type star; on the contrary, Gebran et al. (2008) found < [Fe/H] >=0.07±0.09 dex for 11 F-type stars analysed through the spectral synthesis technique. The large difference be-

Table 3.6: Mean values of the abundances ratios for each cluster and comparison with literature studies. For Hercules Lyra association only the star HD 70573 was analysed, for which the errors are calculated as the quadratic sum of the σ_1 and σ_2 contributions.

Ref.	< [Fe/H] >	< [C/Fe] >	< [Na/Fe] >	< [Mg/Fe] >	< [Al/Fe] >	< [Si/Fe] >	< [Ca/Fe] >	< [Ti/Fe] >	< [Cr/Fe] >	< [Ni/Fe] >	< [Zn/Fe] >
					Coma Berenices						
This work	−0.05±0.01	−0.08±0.02	−0.09±0.03	−0.05±0.03	0.01±0.01	−0.02±0.01	0.06±0.01	0.02±0.02	0.05±0.02	−0.02±0.02	0.03±0.01
BC15[a]	−0.07±0.02	-	−0.05±0.02	0.01±0.02	-	0.04±0.02	0.04±0.01	0.02±0.02	0.02±0.06	−0.08±0.01	-
					Ursa Major						
This work	−0.01±0.02	−0.02±0.07	−0.07±0.02	−0.03±0.01	0.00±0.03	−0.03±0.03	0.07±0.01	0.02±0.01	0.06±0.04	−0.03±0.02	−0.01±0.05
T17[b]	0.03±0.07	-	−0.06±0.05	−0.03±0.06	−0.02±0.06	0.00±0.03	0.03±0.03	0.05±0.06	0.01±0.03	−0.04±0.03	-
B12[c]	0.01±0.01	-	−0.08±0.03	0.01±0.04	0.09±0.01	−0.03±0.06	0.07±0.01	0.02±0.09	0.01±0.03	−0.05±0.01	−0.12±0.05
					Hercules Lyra						
This work	0.00±0.01	-	−0.02±0.05	−0.02±0.06	-	0.00±0.06	0.08±0.14	−0.01±0.01	0.04±0.01	0.03±0.05	0.03±0.06
B16[d]	0.08	−0.05	−0.14	−0.14	−0.23	−0.08	0.05	0.00	0.03	−0.14	-

[a] Blanco-Cuaresma et al. (2015)
[b] Tabernero et al. (2017)
[c] Biazzo et al. (2012)
[d] Brewer et al. (2016)

tween these two studies could be related to the different line lists and techniques employed and also to the different number of stars analysed. Friel & Boesgaard (1992) analysed high-resolution, high S/N spectra of 14 FG type stars, with $T_{\rm eff} > 5950$ K, through the EW method. In particular, they analysed the spectral window 6078-7755 Å , where they measured 8 Fe I lines. These authors found a mean metallicity of −0.05±0.05 dex, again in good agreement with my results, despite the different type of stars analysed. Regarding the individual stars, my measurements for HIP 61205 confirm the results of Brewer et al. (2016), for which the authors find $T_{\rm eff}$ =5796 K, log g =4.51 dex and [Fe/H]=−0.02. Brewer et al. (2016) also derived abundances for different atomic species, in particular they find that [C/Fe]=−0.04, [Na/Fe]=−0.12, [Mg/Fe]=−0.06, [Al/Fe]=−0.12, [Si/Fe]=−0.04, [Ca/Fe]=0.02, [Ti/Fe]=−0.02, [Cr/Fe]=0.01, and [Ni/Fe]=−0.09. All abundance ratios agree very well with my estimates, as shown in Table 3.4. For TYC 1991 − 1235 − 1, TYC 1989 − 0049 − 1, and TYC 1989 − 147 − 1, there are no previous studies on abundances in the literature.

For the UMa moving group, the mean metallicity [Fe/H]=−0.01±0.01 is in fair agreement with the results from Soderblom & Mayor (1993), King & Schuler (2005), and Monier (2005), which reported mean values equal to −0.08±0.09, −0.06±0.05, and −0.05±0.02, respectively. My results also confirm what Biazzo et al. (2012) and Tabernero et al. (2017) report; these authors analysed stars similar to this sample and using the same technique. My results agree well with the two studies. HD 167389 has been analysed by Ammler-von Eiff & Guenther (2009) and Tabernero et al. (2017). In particular, the former derived the stellar parameters and abundances of Fe and Mg through spectral synthesis: they find $T_{\rm eff}$ =5895±80 K, log g =4.37±0.15 dex, ξ=0.99±0.20 km s^{-1}, [Fe/H]=−0.02 ± 0.07, [Mg/Fe]=−0.03 ± 0.05, in excellent agreement with my estimates. Tabernero et al. (2017) analysed candidate members of the UMa group to confirm their membership through chemical tagging by employing the EW analysis method. The authors found for HD 167389 $T_{\rm eff}$ =5978 K, log g =4.56 dex and [Fe/H]=+0.01, as my results. Moreover, they derived abundances for various atomic species, finding [Na/Fe]=−0.06±0.01, [Mg/Fe]=−0.07 ± 0.03, [Al/Fe]=−0.05 ± 0.01, [Si/Fe]=−0.02 ± 0.01, [Ca/Fe]=0.03 ± 0.01, [Ti/Fe]=0.01 ± 0.01, [Cr/Fe]=−0.01 ± 0.01, and [Ni/Fe]=−0.04 ± 0.01. HD 59747 was analysed by Ammler-von Eiff & Guenther (2009), who derived the stellar parameters, [Fe/H], and [Mg/H] through spectral synthesis fitting. The authors found $T_{\rm eff}$ =5094 K, log g =4.55 dex, [Fe/H]=−0.03, and [Mg/Fe]=−0.01, in excellent agreement with my results.

In the Her-Lyr association, only the star HD 70573 was analysed, which is also the star with the highest $v \sin i$ in the sample. This star was also analysed by Gonzalez et al. (2010) in the standard way, that is using Fe (neutral and ionised) lines to derive the atmospheric parameters. These authors found $T_{\rm eff}$ =5807±85 K, log g =4.35±0.08 dex, ξ=1.80±0.16 km s^{-1} and [Fe/H]=−0.05±0.06. These results are also confirmed by Ghezzi et al. (2010), who analysed the star in the same way, finding $T_{\rm eff}$ =5884±26 K, log g =4.57±0.08 dex, ξ=1.69±0.06 km s^{-1} and [Fe/H]=−0.04±0.03. My results confirm the parameters values reported in the two different studies, with the exception of ξ, for which I find a lower value equal to 1.10±0.10 km s^{-1}; there is a difference of the order of 0.6-0.7 km s^{-1} between the two studies. Such a discrepancy could be explained with differences in the atomic data of lines in the list used, or, most likely, it could be due to the effects presented in Chapter 2. As shown in Table 3.6, my results confirm those found by Brewer et al. (2016). However there is large differences for some elements, such as Na, Mg, and Ni, which could be due to differences in the line list used, in particular to differences in the atomic line parameters, and to the different spectroscopic analysis technique employed.

3.6 Carbon abundance

The abundance of C was derived by using four different indicators: two high-excitation potential lines at 5380.337 and 6587.61 Å (atomic data from Amarsi et al. 2019) in the optical region; the NIR line at 16021.7 Å (atomic data from Shetrone et al. 2015); and the CH molecular band at 4300Å , for which molecular line data come from Plez (priv. communication). The line at 16021.7Å suffers from a blend with Fe and Si lines in the blue wing. This blend is not significant for the Sun, TYC 1991 – 1235 – 1, and HIP 61205, but it becomes more important in HD 167389 ($T_{\rm eff}$ =6000 K), because the Si feature is a high-excitation line (χ = 7.035 eV), which strengthens at these temperatures. For this reason, the abundance in the NIR range for this star was not derived. The abundances of C I lines in the optical part were calculated with the EW method, while the abundances for the NIR lines and for the CH feature were calculated through spectral synthesis. NLTE correction were applied to C I optical abundances following Amarsi et al. (2019). Despite the wide range in $T_{\rm eff}$ covered by the stars we analysed, NLTE corrections of optical lines are small, typically of the order of −0.01 dex.

As already mentioned in Section 3.1, the derivation of precise C/O ratio values is critical to understand how planets formed and, eventually, moved in the protoplanetary disc through radial migration. Usually, abundances of oxygen (O) are derived from OH molecular features in the NIR, but in FG stars molecular absorption is less important, weakening the lines (Souto et al. 2018). As a consequence, the O abundance could not be derived for the stars for which we have GIANO-B spectra. Instead, for the K-type star TYC 1989 – 0049 – 1 the NIR spectrum is not available, hampering the determination of abundances through the molecular lines. It has been also argued that extremely high-resolution, high S/N spectra are required to be able to measure OH lines (Meléndez 2004). Additionally, the HARPS-N spectra does not allow to cover the O I triplet at 7773 Å, which is ideal for solar-type stars. Despite the forest of CN lines in the solar spectrum covering the blue, red, and NIR part of it (Sneden & Lambert 1982), N abundance from those molecular lines was not derived. First of all, for solar-type stars the best tools to derive reliable N abundance are high-excitation N I atomic lines at 7400-8720 Å (Asplund et al. 2009; Sneden et al. 2014), which is not covered by HARPS-N (and GIANO-B) spectra. Moreover, it should be noticed that N has little impact on the molecular equilibrium. Thus, I derived only C abundance, fixing O and N abundances to solar values, which is a reasonable assumption for the stellar sample that is comprised of intermediate-age, thin disc, main-sequence stars (e.g. Bensby et al. 2014).

The values for the Sun are reported in Table 3.2; for C abundance inferred from the CH features I obtained $\log(C)_{\odot}$=8.35±0.08, that is marginally lower than what obtained from the atomic lines. Such difference can be due to the atomic data of the CH feature, which are not so precise. In Figure 3.6 the different C abundance estimates are reported as a function of $T_{\rm eff}$. The empty symbols represent the values obtained in the optical range from atomic lines, the red symbols stand for the NIR measurements, and the blue symbols indicate the C values from CH molecular band. The different stars are represented by the different symbols, as described in the caption of the Figure. Different trends of the abundances from the different lines can be noticed, in particular the increasing C I abundances at decreasing $T_{\rm eff}$ for the optical measurements. Interestingly, this is not seen for the NIR abundances and the values derived from the CH. Since NLTE corrections of C I optical abundances are negligible for the stars in our sample, its trend with $T_{\rm eff}$ is most likely due to overexcitation effects. Schuler et al. (2015) find similar behaviour when deriving C abundance from two high-excitation lines (with χ similar to the adopted lines) for a star with $T_{\rm eff}$ =5406 K. The authors find that the C abundance inferred from atomic lines is +0.16 dex higher than that derived from the C_2 feature. Recently, Delgado Mena et al. (2021) derived [C/Fe] ratios for a sample of 1111 FGK stars by analyzing HARPS spectra. They found that this ratio increase sharply from $T_{\rm eff} < 5200$ K, especially when using the line 5380.34 Å. However, the stars they have analysed have all older than 4 Gyr, so the authors concluded that the presence of an unknown blend is responsible for the observed trend. The interesting aspect is that even if the NIR C line has a high-excitation energy (χ=9.631 eV), the same effect in the abundances is not observed. A possible explanation is that at 1.6 μm there is the H^- absorption minimum, so the deepest photospheric layers of the atmosphere are seen, where LTE is a good approximation to compute the populations of atomic levels. Schuler et al. (2015) argue that the overexcitation could be explained as a NLTE effect, specifically it could be the result of our incapacity to properly model the population of high-energy levels under LTE approximation. Thus, the C abundances obtained from the NIR line, even if it has a high-excitation energy, could be the real C abundances of the stars. Moreover, while for star TYC 1991 − 1235 − 1, $T_{\rm eff}$ =5070 K, I obtained a difference between optical and NIR abundances of +0.26 dex, for HIP 61205, $T_{\rm eff}$ =5825 K, the behaviour is reversed; in this star, the optical C abundance is smaller than the NIR estimate by −0.22 dex. Unfortunately, I could not confirm this trend in the whole temperature range, since GIANO-B spectra are not available for all the stars. As a further test, C abundance was measured from the CH band at 4300Å . I found that the trend with $T_{\rm eff}$ is not statistically meaningful (with a p-value > 0.1) and, most importantly, the overexcitation effect observed for the C I abundances is not present. Also, especially for TYC 1991 – 1235 – 1, the C abundance from CH is in better agreement with the NIR estimate than the optical. We suggest that the values obtained from molecular features in the optical for very young stars are more reliable estimates of C abundances, as already pointed out by Schuler et al. (2015). This is what has been done in Maldonado et al. (2020). For this reason, the [C/Fe] values in Table 3.4 are calculated with the C abundance derived from CH lines.

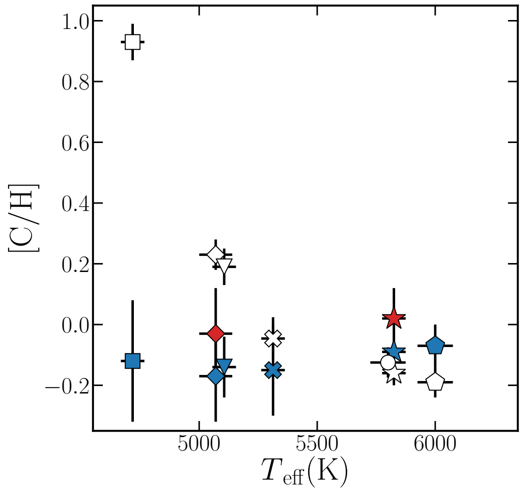

Figure 3.6: Abundances of C I as a function of $T_{\rm eff}$, derived from the optical analysis (empty symbols), from the NIR line (red symbols), and from CH band at 4300Å . The different symbols are the different estimates for the same star: the diamond represents TYC 1991 − 1235 − 1, the star HIP 61205, the pentagon HD 167389, the circle HD 70573, the triangle HD 59747, the square TYC 1989 − 0049 − 1, and finally the x-shaped symbol indicates TYC 1989 − 147 − 1.

3.6.1 The effects of stellar activity

The overexcitation and overionisation effects observed for the C and Cr II abundances are among the main problems affecting the analysis of young and intermediate-age ($\tau \lesssim$ 800 Myr) and cool dwarf stars ($T_{\rm eff} \lesssim$5400 K). These effects increase dramatically as age and temperature decrease, and reflect fundamental issues in the spectroscopic analysis of such stars.

One of the possible explanation could be found in the fact that young stars are more active and, consequently, they have more intense chromospheric or photospheric magnetic fields than older stars. The main effect of local magnetic fields on spectral lines is the broadening of their profile through the Zeeman effect that causes a splitting of the spectral line into its multiplet components. This effect is directly proportional to the wavelength and to the value of the Landè $g_{\rm L}$ factor. The latter parameter measures the sensitivity of an atomic transition to the magnetic fields, meaning the higher the $g_{\rm L}$ factor, the more sensitive the line is to Zeeman splitting. The C I NIR (16021Å) and optical (5380Å and 6588Å) lines have a Landè factor equal to 1.15, 1.0, and 1.0, respectively. For the Cr II lines at 4848.23 Å and 5237.33 Å the $g_{\rm L}$ is equal to 1.25 and 1.30, respectively. According to Shchukina et al. (2015), these lines are insensitive to the presence of magnetic fields, which produce the stronger effects in lines with $g_{\rm L} \sim 2.0$ typically. Moreover, the Zeeman splitting has two main effects on the spectral line. On one hand, it produces a broadening of the profile and an increase of the EW. On the other hand, the line weakens, with a decrease of its depth; thus, the two effects compensate for each other (Reiners et al. 2013). In this case, the Zeeman effect might be excluded as a possible explanation of the observed trends in Figures 3.4 and 3.6 .

In Figure 3.7, the estimates of the C (panel on the left) and Cr II (panel on the right) abundances from the atomic lines (empty symbols) in the optical range and from the CH molecule (blue symbols) are displayed as a function of the activity index log $R'_{\rm HK}$. The latter values were calculated with Yabi[4] interface (Hunter et al. 2012), following the prescription of Noyes et al. (1984) and through the procedure described by Lovis et al. (2011). Yabi is a Python web application installed at IA2 in Trieste that allows authorised users to run the HARPS-N DRS pipeline on proprietary data with custom input parameters. Since I analysed co-added spectra of the stars, I calculated the mean values of the activity indexes, averaging over the spectra used in the co-adding procedure. The log $R'_{\rm HK}$ indexes are reported in Table 3.1.

As shown, the C I abundances from atomic lines in the optical range have a positive correlation with the log $R'_{\rm HK}$, with a Pearson correlation coefficient of r=0.69 and p-value=0.08. On the contrary, the abundance values derived from the CH features do not

---

[4] `https://www.ia2.inaf.it`

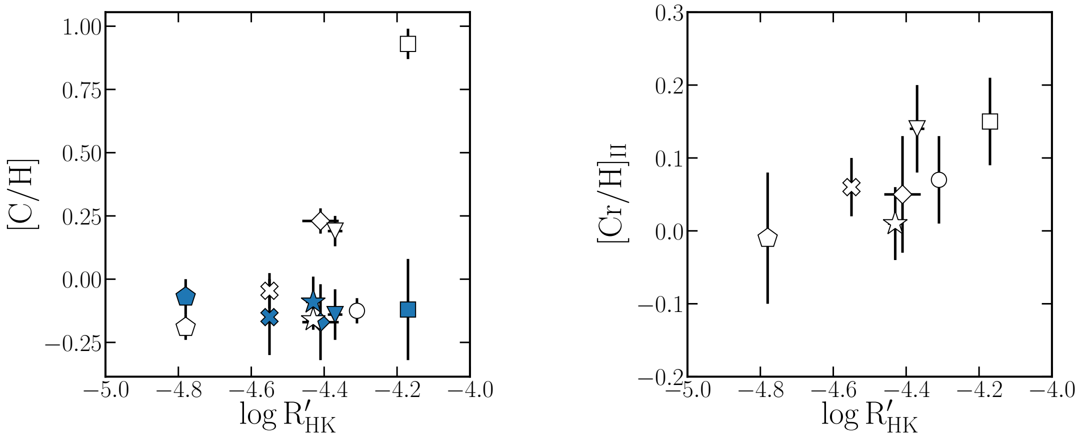

(a) Carbon

(b) Chromium

Figure 3.7: *On the left:* Abundances of C I derived from atomic lines in the optical range (empty symbols) and from the CH molecular features (blue symbols) as a function of the activity index log R'_{HK}. *On the right:* Abundances of Cr II as a function of activity index log R'_{HK}. The symbols in both panels are the same as in Fig.3.6.

correlate with the activity indexes, again suggesting that these values are more reliable estimates of C abundances. A similar behaviour is seen for Cr II abundances, as shown in the right panel of Figure 3.7. We may envisage different, plausible scenarios to explain this peculiar trend. The effect of the chromospheric emission in active stars is observed mainly in the Lyman-α lines of H atom, the Ca II H and K lines, Mg II lines, and He lines. In particular, the photons from the Lyman-α, with an energy of 10.2 eV, can ionise Cr atoms that have a first ionisation potential of 6.77 eV. So, the population of Cr II atoms is larger than Cr I and this can qualitatively explain the increase of abundance at increasing levels of activity. In the case of C I lines, a possible explanation of the overabundance is the presence of unknown blends in the optical lines that become stronger as the $T_{\rm eff}$ decreases. Moreover, these blends could be more important in active stars than in quiet stars, if a significant part of the flux comes from cool regions, such as photospheric dark spots, where the lines are stronger and/or more sensible to the temperature. Another possible explanation is that the increase of the population of the atomic levels (from which the 5380 and 6587 Å lines form) is mainly due to UV continuum photons between 1450 Å and 1650 Å, which increase in intensity at increasing levels of activity (Linsky et al. 2012). These photons might be responsible of the larger population of the levels from which the 5380 Å and 6587 Å lines are formed. Although there isn't a definitive explanation to the overionisation/excitation effects, the solutions proposed seem intriguing and worthy of a detailed investigation.

I also find that the ξ values obtained using Ti lines do not seem to correlate with log R'_{HK}, as shown in Figure 3.8. The symbols in this figure are colour coded according to the $T_{\rm eff}$. As already known, the ξ velocity increases systematically towards higher $T_{\rm eff}$ and lower log g. In particular, in dwarf stars (log $g \sim 4.50$ dex) the ξ values are of the order of 0.70 km s^{-1} at $T_{\rm eff}$ ~4500 K (Steffen et al. 2013). Thus, the trend of ξ with $T_{\rm eff}$ observed in Figure 3.8 is expected. I computed the Pearson correlation coefficient for the trend, that is equal to $r = -0.49$, with $p = 0.26$; thus it is not significant at $p < 0.10$. This result further validates the new spectroscopic approach and what was previously presented in Chapter 2.

3.7 Conclusions

In this Chapter, I presented the first results of an extensive analysis of optical and NIR spectra of stars observed by the GAPS-YO program and the main strategy used by the stellar characterisation team. In particular, I derived the atmospheric parameters and the chemical composition of seven target stars, the Sun, and two RV standard stars, HD159222 and HD3765, using a new spectroscopic approach to overcome analytical issues related to the relatively young ages of the stars.

The analysis of young and intermediate-age stars, in particular in the cool temperature regime ($T_{\rm eff} \lesssim 5400$ K), is not trivial, owing to a series of effects still unexplained from a theoretical point of view. For these reasons, I applied the same methodology as in Baratella et al. (2020b) for the analysis of the optical HARPS-N spectra. In general, the derived spectroscopic estimates of the atmospheric parameters are in excellent agreement with the initial guesses. These were used to derive the abundances in the NIR part, through the spectral synthesis technique and using the same line list as in D'Orazi et al.

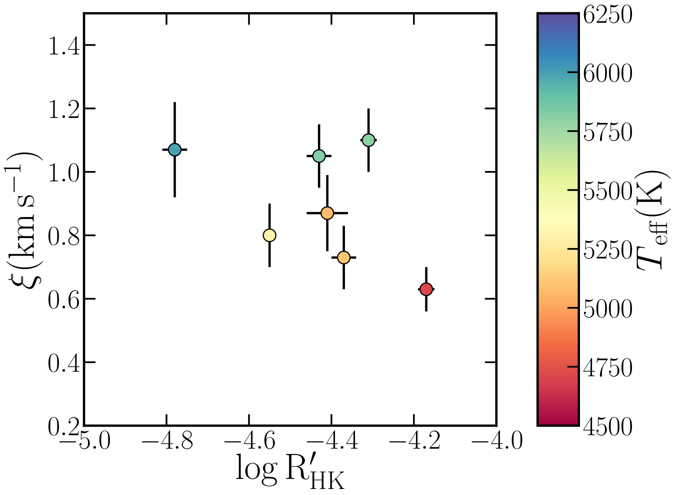

Figure 3.8: Values of ξ parameter derived with the new approach as a function of the chromospheric activity index log R$'_{\rm HK}$. The symbols are colour-coded according to the $T_{\rm eff}$.

(2020). I derived abundances for 11 atomic species, both α-, proton-capture and iron-peak elements. Overall, we find a good agreement between optical and NIR abundances. The lack of trends between [X/H] and $T_{\rm eff}$ confirms that my analysis is reliable, with the exception of Cr II, for which instead a trend of increasing abundances at decreasing temperatures is observed. This trend confirms the previous findings of Schuler et al. (2006, 2010) about the overionisation effects. The derivation of C I abundances from optical atomic lines reveals a similar effect. The two lines used have high-excitation potential and they yield higher abundances (up to almost +1.0 dex) at decreasing $T_{\rm eff}$. In the NIR, I analysed another high-excitation line, 16021Å , but only in two stars, TYC 1991 − 1235 − 1 and HIP 61205. Despite what I obtained from the optical lines, the same effect as in the optical is not seen in the NIR. Schuler et al. (2015) find a trend similar to what we observed for two C lines with χ >7eV and these authors suggested that the C abundance from C_2 features is more reliable. In a similar way, I derived C abundances from CH molecular band at 4300Å . At variance with what obtained from the atomic lines, I did not observe the same trend for the new abundance determinations, in agreement with the findings of Schuler et al. (2015). We suggest that for very young and cool stars the C abundance derived from molecular lines is more reliable.

The overionisation/excitation effects could be explained by different factors, such as the higher level of activity due to the young age of the stars and the presence of intense local chromospheric and/or photospheric magnetic fields that can alter the line profiles. Indeed, I found a positive correlation between the C abundances derived from the atomic lines in the optical range and the activity indexes log $R'_{\rm HK}$, suggesting that these effects are related to higher activity levels. This behaviour is not seen in the C estimates from CH molecular features. I also found a positive correlation between the Cr II values and log $R'_{\rm HK}$. However, as already pointed out in previous studies (Baratella et al. 2020b; Spina et al. 2020), the main causes are still unknown and they may be a combination of different factors, most likely a combination of more intense chromospheric or photospheric magnetic fields.

CHAPTER 4

The *Gaia*-ESO Survey: a new approach to chemically characterising young open clusters

II. Abundances of the neutron-capture elements Cu, Sr, Y, Zr, Ba, La, and Ce

Based on:
Baratella M., D'Orazi V., Sheminova, V., et al., 2021, A&A, Volume 653, id.A67, 24 pp

Young open clusters (ages less than 200 Myr) have been observed to exhibit several peculiarities in their chemical compositions. These anomalies include a slightly sub-solar iron content, super-solar abundances of some atomic species (e.g. ionised chromium), and atypical enhancements of [Ba/Fe], with values up to ~ +0.7 *dex. Regarding the behaviour of the other s-process elements like Y, Zr, La, and Ce, there is general disagreement in the literature: some authors claim that they follow the same trend as Ba, while others find solar abundances at all ages. In this Chapter I expand upon the previous analysis of a sample of five young open clusters (IC 2391, IC 2602, IC 4665, NGC 2516, and NGC 2547) and one star-forming region (NGC 2264), with the aim of determining abundances of different neutron-capture elements, mainly Cu* I, *Sr* I, *Sr* II, *Y* II, *Zr* II, *Ba* II, *La* II, *and Ce* II. *For NGC 2264 and NGC 2547 I present the measurements of these elements for the first time. After a careful selection, I derive abundances of isolated and clean lines via spectral synthesis computations and in a strictly differential way with respect to the Sun. The selected clusters have solar [Cu/Fe] within the uncertainties, while I confirm that [Ba/Fe] is super-solar, with values ranging from +0.22 to +0.64 dex. The analysis also points to a mild enhancement of Y, with [Y/Fe] ratios covering values between 0 and +0.3 dex. For the other s-process elements the [X/Fe] ratios are solar at all ages. It is not possible to reconcile the anomalous behaviour of Ba and Y at young ages with stan-*

dard stellar yields and Galactic chemical evolution model predictions. I explore different possible scenarios related to the behaviour of spectral lines, from the dependence on the different ionisation stages and the sensitivity to the presence of magnetic fields (through the Landé factor) to the first ionisation potential (FIP) effect. I also investigate the possibility that they may arise from alterations of the structure of the stellar photosphere due to the increased levels of stellar activity in stars with ages less than ~ 200 *Myr. However, we are still unable to explain these enhancements, the Ba puzzle remains unsolved and other elements, for example Sr, Zr, La, and Ce, might be more reliable tracer of the s-process at young ages*

4.1 Introduction

Beside the apparent metal-poor nature of YOCs, another intriguing aspect of these systems is the behaviour of the elements mainly produced via the *slow* neutron-capture process (hereinafter s-process elements, Käppeler et al. 2011, and references therein).

Early analytical models found that the solar system abundances of the whole s-process elements could be explained by the contribution of the weak, the main and the strong components. The weak component accounts for the formation of elements up to the atomic mass A~90 (from Fe to strontium, Sr) and it takes place mostly in massive stars during convective He core and C shell burning phases (e.g. The et al. 2007, Pignatari et al. 2010; Sukhbold et al. 2016; Limongi & Chieffi 2018). Most of the copper (Cu), gallium (Ga), and germanium (Ge) in the solar system is made by the weak s-process in massive stars (Pignatari et al. 2010). In particular, copper was thought to be mostly made by thermonuclear supernovae since the s-process contribution was limited (Matteucci et al. 1993). However, thanks to a new generation of neutron-capture reaction rates the s-process production of copper in massive stars was revised (Heil et al. 2008). Therefore, present s-process calculations in massive stars means that the missing copper and the solar abundances can be explained (Bisterzo et al. 2005; Romano & Matteucci 2007; Pignatari et al. 2010). Elements with A~ 90 – 208 traditionally belong to the main and strong components (e.g. Gallino et al. 1998; Bisterzo et al. 2014; Kobayashi et al. 2020), which are associated with low-mass asymptotic giant branch (AGB) stars ($\approx 1.5 - 4$ M$_\odot$), during the thermally pulsating phase (e.g. Lugaro et al. 2012; Karakas & Lattanzio 2014). Rubidium (Rb), strontium (Sr), yttrium (Y), and zirconium (Zr, with atomic number $37 \leq$ Z ≤ 40) belong to the first peak of the s-process in the solar abundance distribution; barium (Ba), lanthanum (La), cerium (Ce), praseodymium (Pr), and neodymium (Nd, with $56 \leq$ Z ≤ 60) populate the second-peak; finally lead (Pb) and bismuth (Bi) are at the third peak. The three peaks correspond to the neutron magic numbers N=50, 82, and 126.

Starting from the pioneering work of D'Orazi et al. (2009a), it has been confirmed that the observed [Ba/Fe] ratios dramatically increase at decreasing ages, reaching values up to +0.60 dex in very young clusters like IC 2391 and IC 2602 (ages of $\sim 30-50$ Myr). Conversely, older clusters with ages $\gtrsim 1$ Gyr exhibit solar-scaled abundances. The Ba over-abundance has subsequently been confirmed by other studies (e.g., Yong et al. 2012; Jacobson & Friel 2013, among the others).

The interest also moved toward the behaviour of other *s*-process elements, like Y, Zr, La and Ce. At present the abundance evolution of these elements with respect to age is a matter of debate. Maiorca et al. (2011) measured abundance ratios for these elements in a sample of 19 OCs, with ages from 0.7 to 8.4 Gyr and they found a steep growth at younger ages. Similar conclusions have been reached by Magrini et al. (2018), who analysed a sample of 22 OCs with ages spanning from 0.1 to 7 Gyr. Recently, Frasca et al. (2019) studied the young cluster ASCC 123 (age $\sim$ 150 Myr) and found an overabundance of Sr, Y, and Zr, with values between +0.3 and +0.5 dex. On the other hand, other studies confirmed that young clusters and local moving groups display first and second peak elements with a different behavior than Ba, in all cases showing solar values of Y, Zr, La and Ce (e.g., D'Orazi et al. 2012; Yong et al. 2012; Jacobson & Friel 2013; D'Orazi et al. 2017). Reddy & Lambert (2015) analysed stars belonging to five local associations ($5-200$ Myr) and they found a large spread in [Ba/Fe] ratios, from +0.07 to +0.32 dex. Mishenina et al. (2015) again confirmed the trend of increasing Ba at decreasing ages from the analysis of giant stars in five OCs, together with solar-like abundances of La. In Chapter 1 the extensive discussion on the time evolution of the *s*-process elements has been

The extraordinary enhancements of Ba cannot be explained neither with non-local thermodynamic equilibrium (NLTE) effects, nor with stellar nucleosynthesis and GCE models (Travaglio et al. 1999; Busso et al. 2001). As discussed in D'Orazi et al. (2009a), increasing the stellar yields by a factor ~6 for AGB stars with masses of $1-1.5\,M_{\odot}$, a GCE model is able to reproduce the observed abundances up to $500-600$ Myr, but not the measured massive over-production of Ba in the last $50-100$ Myr. Indeed, from the stellar nucleosynthesis point of view the most puzzling signature to explain is not the intrinsic enrichment of Ba, but *the production of Ba disentangled from La*. For pure nuclear physics reasons, this cannot be done in *s*-process conditions (e.g., Käppeler et al. 2011). At the same time, observations of old metal-poor *r*-process rich stars have confirmed that also the *r*-process co-produce Ba and La in similar amounts (e.g., Sneden et al. 2008, and references therein). In light of these considerations, Mishenina et al. (2015) proposed the *intermediate* (*i*-) process as a possible explanation of the Ba enrichment in OCs.

The *i*-process was firstly introduced by Cowan & Rose (1977) and it is characterised by neutron densities that are intermediate between the *s*-process and the *r*-process, in the order of 10^{14-16} neutrons cm^{-3}. In these conditions, Ba production is disentangled from La, and it is indeed possible to reproduce the high [Ba/La] ratios seen in stars hosted by YOCs (Bertolli et al. 2013; Denissenkov et al. 2021). Different types of stars have been proposed as possible stellar hosts of the *i*-process: post-AGB stars (Herwig et al. 2011) and low-mass AGB stars (e.g., Lugaro et al. 2015; Cristallo et al. 2016; Choplin et al. 2021), super-AGB stars (Jones et al. 2016), rapidly-accreting white dwarfs (e.g., Denissenkov et al. 2017; Côté et al. 2018; Denissenkov et al. 2019) and massive stars (Roederer et al. 2016; Clarkson et al. 2018; Banerjee et al. 2018). However, in the context of YOCs which stellar site where the *i*-process becomes so relevant only in the last ~Gyr is still a mystery. From the analysis of solar-twin stars, Reddy & Lambert (2017) found a mild increase of La, Ce, Nd, and Sm with decreasing ages, while the trend for [Ba/Fe] is more evident and confirms all the previous findings. They also provided an important piece of evidence in trying to solve this so-called barium puzzle. In fact, these authors detected a positive correlation between the activity index of the stars and their [Ba/Fe] ratios. A similar trend between [Ba/H] and chromospheric/accretion diagnostics were also found in the Lupus SFR by Biazzo et al. (2017).

As shown in the previous Chapters, the higher levels of stellar activity could affect the formation of spectral lines in the upper layers of the photosphere. The moderate and strong lines (those forming in the upper layers of the photosphere) are systematically deeper in a young solar-analog than in the old and quiet Sun. The same result was confirmed by Yana Galarza et al. (2019) and Spina et al. (2020), who proposed that the magnetic intensification could be responsible of the observed patterns. In Spina et al. (2020), the same effect was observed also for the Ba line at 5853.7 Å. In both studies, intermediate-age (~ 400 Myr) stars have been analysed: the solution of magnetic intensification might be sufficient at these ages, but this might not be the case for stars as young as those analysed in this work.

In this Chapter, I expand the analysis of these stars to derive the abundances of the heavy elements Cu, Sr, Y, Zr, Ba, La and Ce. The main goal of this new investigation is to shed light on the behaviour of the *s*-process dominated elements and fin hints that could help us solving the Ba puzzle. I have analaysed the same stars of Chapter 2. To our knowledge, for the cluster NGC 2547 and the SFR NGC 2264 no previous studies focused on the heavy elements abundances have been published so far. The exceptions are IC 2391 and IC 2602, which will be used as calibrators, NGC 2516, for which only few elements have been investigated in the past, and IC 4665, recently analysed by Spina et al. (2021) within the GALAH DR3 (Buder et al. 2020).

This Chapter is organised as follows: in Section 4.2 I briefly summarise the characteristics of the stellar data; in Section 4.3 the procedure adopted to derive the abundances is presented as well as details on the selected lines of each elements; in Section 4.4 I discuss the results and compare them with available literature measurements; in Section 4.5 I explore different possible solution to the Ba puzzle, both form a spectral and from a nucleosynthesis point of view; finally, in Section 4.6 I draw the main conclusion of this analysis.

4.2 Data

The observational data have already been described in Chapter 2. To summarise, the spectra of 23 dwarf stars observed in five YOCs IC 2391, IC 2602, IC 4665, NGC 2516 and NGC 2547, and the SFR NGC 2264 are analysed. In addition to these, I analysed also spectra of the Sun and the four (old and slow-rotating) Gaia benchmark stars (hereafter GBS), namely α Cen A, τ Cet, β Hyi and 18 Sco, exploiting UVES spectra taken from Blanco-Cuaresma et al. (2014b). Out of 34 GBS, our selection was restricted only to those targets with atmospheric parameters similar to our stars (Jofré et al. 2015c, 2018).

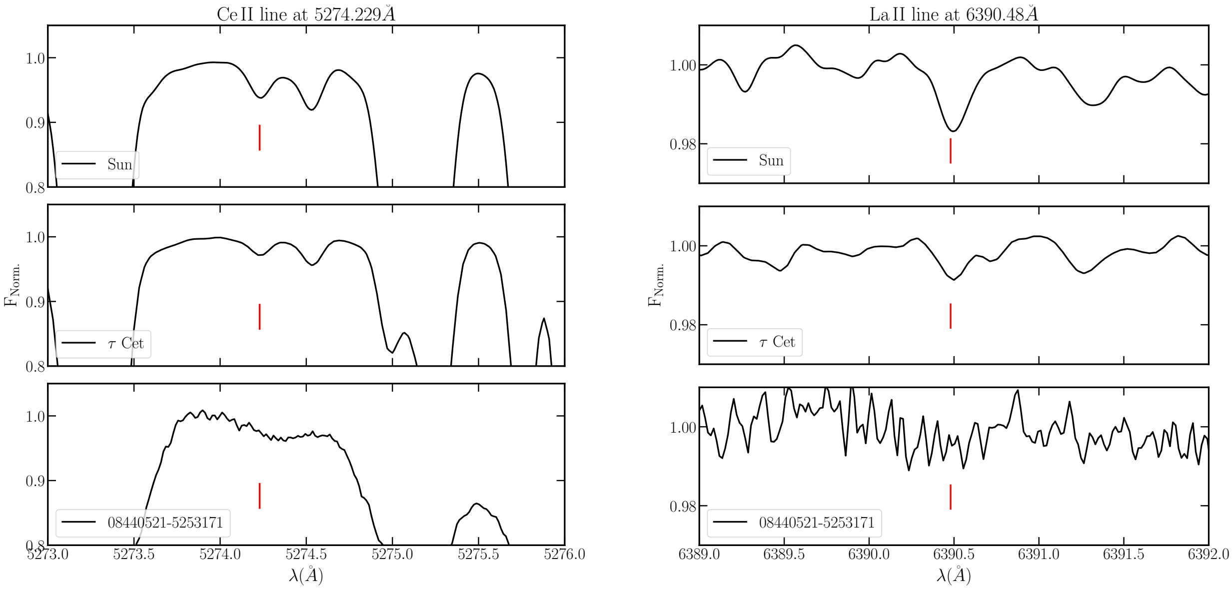

Figure 4.1: Comparison of spectra of the Sun (top), *τCet* (central) and the star 08440521-5253171 (bottom) of IC 2391 (S/N=260) in two spectral regions: on the left, a 3 Å window around the Ce II line 5274.23 Å, while on the right a region near the La II line at 6390.48 Å are shown.

The UVES spectra were acquired with the 580-setup (spectral coverage 4800-6800 Å) of FLAMES-UVES spectrograph (nominal resolution $R = 47\,000$; Pasquini et al. 2002b) and reduced according to the *Gaia*-ESO pipeline (see Sacco et al. 2014). It is well known that the majority of strong, clean and isolated atomic lines for heavy-element abundance

Table 4.1: Atomic data of the lines used in the analysis, both for the bluer (3800 – 4800 Å) and the redder (4800 – 6800 Å) ranges.

Element	λ (Å)	E.P. (eV)	$\log gf$	Ref. $\log gf$	$\log(X)_\odot$	g_L	FIP (eV)[a]
				3800 - 4800 Å(archive)			
Sr I	4607.33	0.00	0.28	Bergemann et al. (2012)	2.72 ± 0.07 ± 0.07(LTE) 2.82 ± 0.07 ± 0.07(NLTE)	1.00	5.69
Sr II	4215.52	0.00	−0.16	Bergemann et al. (2012)	2.87 ± 0.18 ± 0.1(LTE)	1.33	5.69
Y II	4398.01	0.13	−1.00	Hannaford et al. (1982)	2.26 ± 0.10 ± 0.08	1.00	6.38
Zr II	4050.32	0.71	−1.06	Ljung et al. (2006)	2.55 ± 0.08 ± 0.06	0.90	6.84
Zr II	4208.98	0.71	−0.51	Ljung et al. (2006)	2.58 ± 0.11 ± 0.05	0.86	6.84
La II	3988.51	0.40	0.21	Lawler et al. (2001)	1.05 ± 0.07 ± 0.07	1.33	5.58
La II	4086.71	0.00	−0.07	Lawler et al. (2001)	1.10 ± 0.10 ± 0.06	0.83	5.58
Ce II	4073.47	0.48	0.21	Lawler et al. (2009)	1.55 ± 0.08 ± 0.07	-[b]	5.47
				4800 - 6800 Å(*Gaia*-ESO)			
Cu I	5105.54	1.39	−1.52	Kurucz (2011)	4.21 ± 0.12 ± 0.07	1.10	7.72
Y II	4883.69	1.08	0.07	Hannaford et al. (1982)	2.19 ± 0.08 ± 0.06	1.13	6.38
Y II	5087.42	1.08	−0.17	Hannaford et al. (1982)	2.16 ± 0.07 ± 0.05	1.25	6.38
Zr II	5112.27	1.67	−0.85	Ljung et al. (2006)	2.59 ± 0.06 ± 0.02	0.80	6.84
Ba II	5853.69	0.60	−1.01	McWilliam (1998)	2.31 ± 0.08 ± 0.10	1.07	5.21
Ce II	5274.23	1.04	0.13	Lawler et al. (2009)	1.64 ± 0.06 ± 0.05	-[b]	5.47

The solar abundances obtained from our analysis are shown in Column 6. The Landé factor and the FIP are reported in Columns 7 and 8, respectively.

[a] : FIP values are taken from Table D.1 of Gray (1992)

[b] : values of the Landé factor for Ce II lines have not been computed due to the complex term of its levels

determination are located in the wavelength range between 3800-4800 Å, which is not accessible to the considered spectral setup. For this reason, I searched through the ESO archive for further observational data-sets of the cluster stars. Only star 08440521−5253171 (IC 2391) and star 10440681−6359351 (IC 2602) have been observed with either UVES, FEROS ($R \sim 48\,000$, λ = 3500-9200 Å – Kaufer et al. 1999) or HARPS ($R \sim 115\,000$, λ = 3830-6900 Å – Mayor et al. 2003) spectrographs. In addition, I also re-analyse three stars of IC 2391 that have been previously published in D'Orazi et al. (2017), namely PMM 1142, PMM 665 and PMM 4362. These have been observed with UVES (blue setup $\lambda\lambda$=3900 Å) in the framework of the program ID 082.C-0218 (PI C. Melo).

4.3 Analysis

In the following, the details of the selected spectral lines used in the analysis are described (Section 4.3.1), together with the procedure to compute the optical depths (Section 4.3.2) and the details of the abundance measurements (Section 4.3.3).

4.3.1 Selection of the spectral lines

A careful selection of spectral lines in the redder part of the spectra was carried out, searching in the official *Gaia*-ESO survey master line-list (Heiter et al. 2020) for lines of Cu I, Sr I and Sr II, Y II, Zr I and Zr II, Ba II, La II and Ce II. From this list, I selected only lines with highly accurate measurements of the atomic data (*gf_flag*=Y) and mostly unblended (*synflag*=Y or U). The *Gaia*-ESO line list covers the wavelength range 4750-6850 Å for the region of the UVES-580 setting. For the bluer part of the spectrum, I included lines that have been extensively used and that have been proven to be reliable (see, e.g., D'Orazi et al. 2017).

Despite the large number of lines available for each atomic species, I selected only those that are moderately strong and not blended in the solar spectrum. Since the stellar sample includes stars with $v \sin i$ up to 20 km s^{-1} and some of the spectra are noisy, most of the pre-selected lines are too broad and not measurable. Two examples for lines 5274.23 Å of Ce II and 6390.48 Å of La II are illustrated in the left and right panels of Figure 4.1, respectively. In this Figure, observed spectra of the Sun, τ Cet and star 08440521−5253171 of IC 2391 ($v \sin i$ =16.7km s^{-1} and S/N=260) are displayed. As it can be seen, both lines are already relatively weak, though still usable, in the Sun, but they disappear at higher values of $v \sin i$.

In the following, I report the details of the lines used in the analysis:

`Copper:` in the solar spectrum, only lines of neutral Cu were identified. For this element, the analysis relied just on line at 5105.54 Å, since the one at 5700.24 Å is heavily blended in the Sun, whereas line at 5782.13 Å falls in the UVES wavelength gap. For this element, the isotopic solar mixture of 69% of ^{63}Cu and 31% of ^{65}Cu is considered (Grevesse et al. 2015). Copper is affected by isotopic broadening and hyperfine structure (HFS), for which I adopted values from Kurucz (2011). According to Shi et al. (2014), the NLTE correction for line 5105.54 Å are small in the Sun, being of the order of +0.02 dex.

`Strontium:` lines 4607.33 Å of Sr I and 4215.52 Å of Sr II were measured. According to Bergemann et al. (2012), the Sr I line has a NLTE correction of +0.10 dex in dwarf stars with solar metallicity, while line 4215.52 Å has negligible NLTE corrections. It is worth noting that line of Sr II is very strong and almost saturated. Moreover, it is also blended with a nearby Fe I line at 4215.42 Å and with the CN molecular lines. Both features have been accounted for in the spectral synthesis.

`Yttrium:` regarding Y II, I selected the lines at 4398.01 Å, 4883.69 Å, 4900.12 Å, 5087.42 Å, 5289.82 Å and 5728.89 Å. The line at 4900.12 Å is blended with a nearby Ti I line at 4899.91Å, which becomes significant for $v \sin i > 4 - 5\,\mathrm{km\,s^{-1}}$. The lines at 5289.82 Å and 5728.89 Å, instead, are very weak in the Sun, both having EW$\sim$ 4 mÅ; thus, they cannot be measured in our targets, due to the relatively large $v \sin i$. The HFS for Y can be neglected, as previously discussed in several papers (e.g., D'Orazi et al. 2017).

`Zirconium:` this element is present in the form of neutral and ionised species in the solar photosphere. However, the available reliable lines of Zr I (at 6127.44 Å, 6134.55 Å, 6140.46 Å, 6143.2 Å and 6445.74 Å) are too weak to be measured in the stellar sample. In the bluer region, lines 4050.32 Å and 4208.98 Å of Zr II were analysed. The line at 5112.27 Å of Zr II is also weak and as a matter of fact, it was measured only in the Sun, in the GBS sample and in one target. According to Velichko et al. (2010), Zr II lines form under LTE conditions in solar-type stars.

`Barium:` for ionised barium, instead, I used only 5853.7 Å, which is not blended and does not experience severe HFS or isotopic shifts. To our knowledge, this line is the best diagnostic to measure the Ba abundance. There are other lines of Ba II in our spectral range. However, the resonance Ba II line at 4554.03 Å is almost saturated; the line at 6141.7 Å is known to be blended with a strong Fe I line; the line at 6496.9 Å is also blended with an iron line, and it is affected by strong NLTE effects. Reddy & Lambert (2015) explored the possible detection of the line of neutral Ba at 5535 Å in a sample of

F-G dwarfs. Still, this line is blended with a strong Fe I line that dominates the profile and its abundance show a significant correlation with $T_{\rm eff}$ (see their Figure 7), most likely caused by large NLTE effects. Therefore, as already pointed out by the authors, in absence of NLTE corrections it is not suitable to derive accurate abundances and to solve the Ba puzzle. Nevertheless, to obtain more accurate abundances, I considered also the HFS data from McWilliam (1998) and the isotopic solar mixture of 81 per cent for (^{134}Ba +^{136}Ba +^{138}Ba) and 19 per cent for (^{135}Ba +^{137}Ba) was adopted (see Grevesse et al. 2015 for further details). According to Korotin et al. (2015), the NLTE corrections are small for stars in the parameter space covered by our sample. Gallagher et al. (2020) derived NLTE corrections for the Sun and found that the $\Delta_{\rm 1D-NLTE}$=−0.11 dex and $\Delta_{\rm 3D-NLTE}$=0.03 dex. However, there are not available tables of NLTE corrections for stars with parameters similar to our sample. In general, the NLTE corrections are not sufficient to solve the Ba puzzle: for these reasons, I report the LTE Ba abundances.

`Lanthanum:` regarding La II, I selected lines at 4804.04 Å, 4920.98 Å, 5122.99 Å and 6390.48 Å. Unfortunately, none of them is strong enough to be measured in the stars in the range 4800 − 6800 Å. Instead, in the bluer part, I relied on the measurements of lines 3988.51 Å and 4086.71 Å. Lanthanum has one single isotope ^{139}La that accounts for 99.9% of the total La abundance in the solar material and it is strongly affected by HFS: the prescriptions by Lawler et al. (2001) were considered.

`Cerium:` finally for Ce, I measured only lines 4073.47 Å and 5274.23 Å. Cerium has four stable isotopes, all with zero nuclear spin: ^{136}Ce (abundance of 0.185%), ^{138}Ce (abundance of 0.251%), ^{140}Ce (abundance of 88.450%), ^{142}Ce (abundance of 11.114%). The isotopic splitting is negligible for both lines, according to Lawler et al. (2009). Thus, it is not affected by HFS.

In Table 4.1 only the lines for which I obtained more than one measurement in the stellar sample are indicated; the element (Column 1), the corresponding wavelength (Column 2), the excitation potential energy (E.P., Column 3), the oscillator strength $\log gf$ (Column 4), references for the $\log gf$ values (Column 5) and the solar $\log(\mathrm{X})_\odot$ (Column 6) of each individual line are given (the average solar abundances are in Table 4.3). For each line we computed the Landé factor $g_{\rm L}$ following Landi Degl'Innocenti (1982) (Column 7). The first ionisation potential (FIP) values, instead, are taken from Table D.1 in Gray (1992) (Column 8).

Table 4.2: Optical depths of line formation log $\tau_{5000\ \mathrm{core}}$ of the line core and log $\tau_{5000\ \mathrm{full}}$ of full line profile.

λ (Å)	El.	E.P. (eV)	log gf	EW$_{\mathrm{obs}}$ (mÅ)	R$_\star$	log $\tau_{5000\ \mathrm{core}}$	log $\tau_{5000\ \mathrm{full}}$	HFS
5105.54	Cu I	1.39	−1.52	88.0	0.51	−3.4	−2.4	y
4607.33	Sr I	0.00	0.28	46.2	0.38	−2.1	−1.6	n
4215.52	Sr II	0.00	−0.16	173.1	0.67	−5.2	−2.5	n
4398.01	Y II	0.13	−1.0	53.3	0.42	−2.6	−1.9	n
4883.69	Y II	1.08	0.07	58.5	0.4	−2.6	−1.9	n
5087.42	Y II	1.08	−0.17	47.3	0.32	−2.1	−1.6	n
4050.32	Zr II	0.71	−1.06	22.0	0.23	−1.4	−1.2	n
4208.98	Zr II	0.71	−0.51	45.3	0.39	−2.1	−1.6	n
5112.27	Zr II	1.67	−0.85	6.5	0.05	−1.1	−1.1	n
5853.69	Ba II	0.60	−1.01	66.4	0.36	−3.2	−2.3	y
3988.51	La II	0.40	0.21	51.0	0.32	−2.7	−1.9	y
4086.71	La II	0.00	−0.07	42.0	0.37	−2.3	−1.7	y
4073.47	Ce II	0.48	0.21	20.3	0.16	−1.5	−1.3	n
5274.23	Ce II	1.04	0.13	9.1	0.05	−1.3	−1.2	n

4.3.2 Computation of the optical depths of line formation

The main working hypothesis is that lines forming in the upper layers of the photosphere (i.e., at smaller log τ_{5000}) are more influenced by the higher levels of the activity present in young stars. Therefore, these lines are stronger than what is observed in spectra of old and quiet stars, affecting the derivation of the stellar parameters and, finally, the abundances (Yana Galarza et al. 2019; Baratella et al. 2020b; Spina et al. 2020). To investigate further this aspect, the optical depth of line formation log τ_{5000} of all the selected lines were computed in a consistent way following the prescriptions by Gurtovenko & Sheminova (2015).

Calculations of the average formation depth of the absorption line are based on the contribution function (CF), which describes the contribution of the various layers of the stellar atmosphere to the absorption line (or line depression). Gurtovenko et al. (1974) suggested to use the CF as the integrand of the emergent line depression in the solar disc center, computed as:

$$R(0) = \int_0^\infty g(\tau_c)\eta(\tau_c)\exp(-\tau_l)d\tau_c = \int_0^\infty CF d\tau_c, \qquad (4.1)$$

where R=$1 - I_l/I_c$ is the line l depression and η is the ratio between the coefficient of the selective absorption and the coefficient of continuum c absorption. In the same formula, g is the Unsold's weighting function for LTE (Unsöld 1932), multiplied by the emergent intensity in the continuum $I_c(\tau_c = 0)$. This weighting function has the following expression:

$$g(\tau_c) = \int_{\tau_c}^{\infty} B(\tau_c) * \exp(-\tau_c) d\tau_c - B(\tau_c) * \exp(-\tau_c), \tag{4.2}$$

where $B(\tau_c)$ is the Plank function.

When dealing with the interpretation of observed line profiles or line depth in its center or equivalent width, the average depth of the layers contributing to the absorption line is used. The average depth at a given wavelength position of the line profile $\Delta\lambda$ and at given position on the stellar disk $\mu = \cos\theta$ is calculated by the following formula:

$$\langle \tau_{\Delta\lambda,\mu} \rangle = \int_{-\infty}^{\infty} \tau CF(\Delta\lambda, \mu, \tau) d\tau / \int_{-\infty}^{\infty} CF(\Delta\lambda, \mu, \tau) d\tau. \tag{4.3}$$

Considering the integrated line profile, i.e. the EW, its average optical depth is calculated as:

$$\langle \tau_{\Delta\lambda,\mu,EW} \rangle = \int_{\lambda_1}^{\lambda_2} \langle \tau_{\Delta\lambda,\mu} \rangle R(\Delta\lambda, \mu) d(\Delta\lambda) / \int_{\lambda_1}^{\lambda_2} R(\Delta\lambda, \mu) d(\Delta\lambda). \tag{4.4}$$

Here $R(\Delta\lambda, \mu)$ is the line depression at $\Delta\lambda$ and μ, while λ_1 and λ_2 are initial and final wavelengths position of the line profile, respectively. To obtain the average depth of formation of the line depression observed in the stellar spectra at a given $\Delta\lambda$, the following formula was used:

$$\langle \tau_{\Delta\lambda,\star} \rangle = \int_{0}^{1} \langle \tau_{\Delta\lambda,\mu} \rangle \mu d\mu. \tag{4.5}$$

Instead, to have the average formation depth of the whole line profile using EWs:

$$\langle \tau_{EW,\star} \rangle = \int_{\lambda_1}^{\lambda_2} \langle \tau_{\Delta\lambda,\star} \rangle R_\star(\Delta\lambda) d(\Delta\lambda) / \int_{\lambda_1}^{\lambda_2} R_\star(\Delta\lambda) d(\Delta\lambda) \tag{4.6}$$

where $R_\star$ is the line depression in the spectra of stellar flux.

In this work, the average depth of line formation of our lines were computed both in the core ($\log \tau_{5000\ \mathrm{core}}$) and in the whole profile ($\log \tau_{5000\ \mathrm{full}}$). The derived values are reported in Column 7 and 8 of Table 4.2, respectively. For this calculation, the classical LTE approximation was assumed. The damping constant associated with the van der Waals force between the absorbing and perturbing atoms was considered to be equal to γ_6, according to the classical Unsold's approximation. These assumptions are acceptable to estimate the average depth of the formation of weak, moderate, and moderately strong lines, like those analysed here. The $\mathrm{EW_{obs}}$ and $\mathrm{R}_\star$ (Column 5 and 6, respectively) of each line using ARESv.2 software (Sousa et al. 2015). Then, the lines were synthesised in the solar spectrum with the SPANSAT code of Gadun & Sheminova (1988). The $\log \tau_{5000}$ value is then derived from the abundance obtained when the EW of the synthetic line matches the EW_{obs}. Following what was done in Chapter 2, the MARCS solar atmosphere model was obtained with the chemical composition taken from Lodders (2019), and with the stellar parameters derived in that Chapter. The macroturbulent velocity equal to 2 km/s and $v \sin i = 1.84$ km s^{-1} were considered (Sheminova 2019).

Some lines (those lines labelled with *y* in Column 9 of Table 4.2) are affected by HFS, which though was considered only indirectly in the computations of log τ_{5000}. Lines affected by strong HFS are splitted into multiple components, resulting in larger EWs. Thus, completely neglecting the HFS when deriving the abundances from EWs will result in overestimated values (Scott et al. 2015; Jofré et al. 2017) and all lines form in higher layers of the photosphere since the overestimated abundances (corresponding to the larger EW_{obs}) is used in the computation of the optical depth. At the same time, the abundance calculated from the fitting of central depths ($R_\star$) of the lines can be underestimated and the depths of the formation of the lines will be large (i.e., the line will form in deeper layers). Therefore, these values are indicative and should be considered with some caution. The code to compute the log τ_{5000} will be further implemented with computations considering the HFS in the future. The possible errors due to the adopted approximations in the aforementioned computations are small and they can be neglected within the limits of specific calculations of the depths of line formation.

4.3.3 Abundance measurements

The abundances of the *s*-process elements were derived using synthetic spectrum line profile fitting technique through the driver *synth* in MOOG (version 2017, Sneden 1973; Sobeck et al. 2011). The 1D-LTE plane-parallel MARCS model atmospheres (Gustafsson et al. 2008) were used, fixing the atmospheric parameters to the values found in Chapter 2 (see Tables 2.4 and 2.6), both for the cluster stars and the GBS. All abundances were computed in a strictly differential way (i.e., line-by-line) with respect to the Sun as $[X/H]_\star = \log(X)_\star - \log(X)_\odot$ (using the individual abundances $\log(X)_\odot$ in column 6 of Table 4.1). The mean values of the adopted solar scale are reported in Table 4.3 for completeness, and they are used only to compare them with literature results. The final abundance ratios $[X/Fe] = [X/H]_\star - [Fe/H]_\star$ can be found in Tables 4.4, 4.5 and 4.6 for the GBS, the stellar sample results in the 4800 − 6800 Å range and in the 3800 − 4800 Å range, respectively. The stars in the sample are in the main-sequence evolutionary phase, therefore the carbon and magnesium isotopic ratios were set to the solar values, equal to $^{12}C/^{13}C = 89$ (Asplund et al. 2009) and ^{24}Mg:^{25}Mg:^{26}Mg=80:10:10 (Fenner et al. 2003), respectively. To compute the synthetic profiles, I used the new tables of limb darkening coefficients (LDCs) by Claret (2019), corresponding to the Gaia G_{BP} pass-band (their Table 6). The rotational broadening profiles were calculated using the $v \sin i$ measured by the *Osservatorio Astrofisico di Catania* (OACT) Node of the *Gaia*-ESO consortium, measured using the routine ROTFIT (see, e.g., Frasca et al. 2015, and references therein, for more details); the values are reported in Column 4 of Table 4.5. The values of $v \sin i$ of PMM 665, PMM 4362 and PMM 1142 were taken from De Silva et al. (2013) (hereafter DS13). However, in some cases (as for stars PMM 1142, PMM 665, PMM 4362 of IC 2391, the star in NGC 2264, the stars 07544342−6024437 and 07574792−6056131 of NGC 2516, and the star 08102854−4856518 of NGC 2547), the profiles computed with the $v \sin i$ taken from literature did not reproduce well the line profiles. Then, I recomputed the $v \sin i$ by looking at 15-20 isolated and clean lines over the whole spectral range. The final measurements of $v \sin i$ can be found in Column 3 of Table 4.5. Of the whole line list in the redder part, I measured only lines 5105.53 Å of Cu, 4883.69 Å and 5087.42 Å of Y and 5853.7 Å of Ba for all the stars. These are the strongest lines in the line list: the large values of $v \sin i$ (up to 18 km s^{-1}) prevented me from measuring weaker lines. I measured Ce abundance from line 5274.23 Å only for 2 stars and Zr from line 5112.27 Å for one star, for which the uncertainty of the best fit model is 0.35 dex (due to the relatively high rotational velocity).

4.3.4 Error budget

There are two sources of internal uncertainties affecting the [X/Fe] ratios derived via spectral synthesis. The first kind of error, σ_1, is related to the best fit procedure, and spans values from ±0.06 to ±0.3 dex depending on the quality of the spectra, mainly the S/N (affecting the continuum placement), and on the individual spectral features under consideration.

The second source of uncertainties, σ_2, is related to uncertainties in the stellar parameters (Table 2.6). These uncertainties were computed in a conservative way by varying each quantity separately, leaving the others unchanged, and evaluating the abundance sensitivity to those changes as:

$$\sigma_2 = \sqrt{\left(\sigma_{T_{\rm eff}} \frac{\partial[{\rm X/H}]}{\partial T_{\rm eff}}\right)^2 + \left(\sigma_{\log g} \frac{\partial[{\rm X/H}]}{\partial \log g}\right)^2 + \left(\sigma_{\xi} \frac{\partial[{\rm X/H}]}{\partial \xi}\right)^2 + \left(\sigma_{[{\rm Fe/H}]} \frac{\partial[{\rm X/H}]}{\partial[{\rm Fe/H}]}\right)^2}. \quad (4.7)$$

Both errors are indicated in Tables 4.1, 4.4, 4.5 and 4.6.

4.4 Results

4.4.1 The Sun and the Gaia Benchmarks

As already mentioned, in Table 4.3 the average solar abundance values are displayed, together with the photospheric abundances from Grevesse et al. (2015), the metoritic abundances from Lodders (2019) and the results reported in the *Gaia*-ESO internal data release 4 (for La and Sr) and 5 (iDR4 and iDR5, respectively). For the abundances of Y, Zr, La and Ce I report the simple mean of the values derived in the bluer and in the redder regions, and the uncertainties are computed as the errors on the mean. For Sr the value in the Table 4.3 is the average between the Sr I (corrected for NLTE) and the Sr II results. For Ba and Cu, for which only one line was analysed, I report the individual abundance, while the uncertainty is the error on the fitting procedure (σ_1). As it can be seen from the comparison with the literature, the mean solar abundances agree well with the photospheric values from Grevesse et al. (2015), and with the meteoritic abundances from Lodders (2019). They are also in fair agreement with the *Gaia*-ESO iDR5 and iDR4 results.

Table 4.3: Mean solar abundances derived in this work, in Grevesse et al. (2015) (G15), and meteoritic abundances from Lodders (2019) (L19). We also report the values derived by *Gaia*-ESO (GES) in iDR5 and iDR4 catalogue.

Species	This work	G15	L19	GES
Cu	4.21 ± 0.12	4.18 ± 0.05	4.21 ± 0.03	4.12 ± 0.10
Sr	2.85 ± 0.03	2.83 ± 0.06	2.83 ± 0.06	2.87 ± 0.1^a
Y	2.20 ± 0.03	2.21 ± 0.05	2.20 ± 0.05	2.19 ± 0.12
Zr	2.57 ± 0.01	2.59 ± 0.04	2.59 ± 0.06	2.53 ± 0.13
Ba	2.31 ± 0.09	2.25 ± 0.07	2.19 ± 0.07	2.17 ± 0.06
La	1.08 ± 0.03	1.11 ± 0.04	1.14 ± 0.03	1.22 ± 0.12^b
Ce	1.60 ± 0.05	1.58 ± 0.04	1.61 ± 0.06	1.70 ± 0.11

^{a} : value reported in the iDR4, derived from Sr I lines only;
^{b} : value reported in the iDR4.

Regarding the GBS, I list in Table 4.4 the abundance ratios [X/Fe] obtained for each line separately in the blue and red spectral ranges, while average values and comparison with the literature are provided in Table 4.7. For Cu and Ba, the uncertainties in the Table represents the total uncertainties (computed as the square root of the sum of the squares of σ_1 and σ_2). Instead, for the other elements the error is the standard deviation of the abundances obtained from the different lines. As it can be seen, for the GBS that are old and *quiet* stars I obtained solar-scaled abundances for all the heavy elements. The estimates for α Cen A, τ Cet and 18 Sco are in fair agreement with Luck (2018), who analysed high-resolution (R= 115 000), high S/N HARPS spectra of a sample of

Table 4.4: Abundances of the $s-$process elements of the GBS. The first source of uncertainty is due to the best fit procedure, while the second is related to uncertainties in the stellar parameters (details on the computations can be found in Sec. 4.3.4).

El.	λ (Å)	[X/Fe]$_{\alpha\,\mathrm{Cen\,A}}$	[X/Fe]$_{\tau\,\mathrm{Cet}}$	[X/Fe]$_{\beta\,\mathrm{Hyi}}$	[X/Fe]$_{18\,\mathrm{Sco}}$
		3800 - 4800 Å			
Sr I(NLTE)	4607.33	−0.02 ± 0.08 ± 0.07	−0.05 ± 0.08 ± 0.07	−0.05 ± 0.11 ± 0.07	+0.05 ± 0.1 ± 0.06
Sr II	4215.52	0.00 ± 0.2 ± 0.1	−0.07 ± 0.19 ± 0.1	−0.07 ± 0.22 ± 0.09	+0.06 ± 0.19 ± 0.09
Y II	4398.01	−0.03 ± 0.15 ± 0.09	−0.14 ± 0.11 ± 0.07	−0.04 ± 0.1 ± 0.07	+0.01 ± 0.13 ± 0.07
Zr II	4050.32	+0.02 ± 0.12 ± 0.06	−0.07 ± 0.14 ± 0.08	−0.02 ± 0.13 ± 0.08	−0.01 ± 0.11 ± 0.06
Zr II	4208.98	+0.01 ± 0.15 ± 0.07	−0.05 ± 0.1 ± 0.09	−0.04 ± 0.12 ± 0.05	+0.01 ± 0.10 ± 0.07
La II	3988.51	−0.04 ± 0.1 ± 0.06	−0.01 ± 0.15 ± 0.06	−0.02 ± 0.15 ± 0.06	+0.10 ± 0.1 ± 0.07
La II	4086.71	−0.08 ± 0.15 ± 0.08	−0.05 ± 0.17 ± 0.07	−0.06 ± 0.16 ± 0.07	+0.06 ± 0.12 ± 0.08
Ce II	4073.47	0.00 ± 0.13 ± 0.06	0.03 ± 0.15 ± 0.05	0.00 ± 0.15 ± 0.05	+0.08 ± 0.08 ± 0.06
		4800 - 6800 Å			
Cu I	5105.54	+0.15 ± 0.20 ± 0.09	−0.08 ± 0.20 ± 0.11	−0.01 ± 0.15 ± 0.11	−0.02 ± 0.10 ± 0.10
Y II	4883.69	+0.02 ± 0.15 ± 0.13	−0.08 ± 0.13 ± 0.09	−0.06 ± 0.15 ± 0.08	−0.09 ± 0.09 ± 0.07
Y II	5087.42	+0.05 ± 0.15 ± 0.1	−0.11 ± 0.13 ± 0.07	−0.05 ± 0.11 ± 0.07	−0.10 ± 0.10 ± 0.07
Zr II	5112.27	−0.06 ± 0.20 ± 0.06	−0.01 ± 0.1 ± 0.07	−0.10 ± 0.07 ± 0.06	+0.01 ± 0.08 ± 0.07
Ba II	5853.69	+0.04 ± 0.15 ± 0.12	−0.12 ± 0.12 ± 0.07	−0.08 ± 0.17 ± 0.11	−0.04 ± 0.15 ± 0.1
Ce II	5274.23	−0.02 ± 0.14 ± 0.08	−0.08 ± 0.1 ± 0.05	−0.06 ± 0.08 ± 0.09	+0.03 ± 0.1 ± 0.05

907 FGK dwarf stars in the solar neighbourhood. My estimates are also similar to the results by Casali et al. (2020b), who performed a detailed spectral analysis of HARPS spectra of 560 solar-type stars. The marginal discrepancies of the individual abundances could be related to the different line lists (i.e., number of lines and inclusion of HFS and isotopic splitting) and methods used (i.e., EW *vs.* spectral synthesis). The abundance values I found agree well with Casamiquela et al. (2020), who analysed a sample of GBS. They used the same spectra and *Gaia*-ESO line list as done here, but they analysed different lines (for instance, the Cu I lines at 5218.20 Å and at 5220.07 Å). Thus, the small discrepancies that can be seen in Table 4.7 (for example for [Cu/Fe] of α Cen A or for [La/Fe] of τ Cet) can be related to the different lines used. β Hyi is a slightly evolved GBS, which is in the sub-giant branch phase of its evolution. In the literature, I find few measurements of the s-process elements: my [Ba/Fe] estimate is in fair agreement with Bensby et al. (2014) and Jofré et al. (2015a). To our knowledge, these are the only results of the heavy elements abundances for β Hyi.

4.4.2 The young clusters

As already mentioned in Section4.2, besides the stars observed within the GES, I analysed three stars of IC 2391 taken from D'Orazi et al. (2017). Firstly, the atmospheric parameters were re-determined by applying the new spectroscopic approach. The final values can be found in Table 4.8. The largest differences are seen for the ξ parameter, for which I obtained a difference $\Delta\xi$(our-DS13)=-0.59 km s^{-1} for star PMM 665, -0.43 km s^{-1} for

Table 4.5: Abundances of the s−process elements derived with the lines (Cu line at 5105 Å, Y lines at 4883 Å and 5087 Å, Zr line at 5112 Å, Ce line at 5274 Å, Ba line at 5853 Å) in the 480-680nm range for the whole stellar sample. The first source of uncertainty (σ_1) is due to the best fit procedure, while the second (σ_2) is related to uncertainties in the stellar parameters (details on the computations can be found in Sec. 4.3.4).

CNAME	S/N	$v \sin i \pm \sigma$	$v \sin i_{\rm lit.}$	$[\rm Cu/Fe]_{I,5105Å} \pm \sigma_1 \pm \sigma_2$	$[\rm Y/Fe]_{II,4883Å} \pm \sigma_1 \pm \sigma_2$	$[\rm Y/Fe]_{II,5087Å} \pm \sigma_1 \pm \sigma_2$	$[\rm Zr/Fe]_{II,5112Å} \pm \sigma_1 \pm \sigma_2$	$[\rm Ce/Fe]_{II,5274Å} \pm \sigma_1 \pm \sigma_2$	$[\rm Ba/Fe]_{II,5853Å} \pm \sigma_1 \pm \sigma_2$
IC 2391									
08365498−5308342	159	8.3 ± 0.3	8.5 ± 0.8	−0.02 ± 0.10 ± 0.09	+0.26 ± 0.10 ± 0.08	+0.25 ± 0.17 ± 0.07	-	-	+0.57 ± 0.12 ± 0.08
08440521−5253171	259	18.4 ± 0.4	16.7 ± 0.8	−0.12 ± 0.10 ± 0.07	+0.24 ± 0.09 ± 0.07	+0.22 ± 0.15 ± 0.09	-	-	+0.52 ± 0.09 ± 0.08
PMM1142[a]	100	7.5 ± 0.4	7.3*	−0.02 ± 0.11 ± 0.10	+0.26 ± 0.10 ± 0.07	+0.21 ± 0.10 ± 0.07	-	−0.02 ± 0.15 ± 0.09	+0.61 ± 0.08 ± 0.07
PMM665[a]	60	8.2 ± 0.3	7.47*	−0.10 ± 0.12 ± 0.10	+0.19 ± 0.10 ± 0.07	+0.14 ± 0.15 ± 0.08	-	-	+0.46 ± 0.10 ± 0.11
PMM4362[a]	58	9 ± 0.3	8.61*	−0.09 ± 0.13 ± 0.08	+0.19 ± 0.15 ± 0.09	+0.23 ± 0.15 ± 0.07	-	-	+0.48 ± 0.10 ± 0.09
IC 2602									
10440681−6359351	92	12.1 ± 0.4	12.2 ± 0.7	−0.15 ± 0.12 ± 0.11	+0.19 ± 0.16 ± 0.11	+0.16 ± 0.17 ± 0.11	-	-	+0.40 ± 0.12 ± 0.13
10442256−6415301	110	11.1 ± 0.3	10.9 ± 0.8	−0.08 ± 0.13 ± 0.11	+0.16 ± 0.15 ± 0.09	+0.15 ± 0.12 ± 0.07	0 ± 0.35 ± 0.10	-	+0.36 ± 0.11 ± 0.08
10481856−6409537	99	14.5 ± 0.2	14.4 ± 0.8	−0.08 ± 0.13 ± 0.10	+0.22 ± 0.15 ± 0.08	+0.15 ± 0.15 ± 0.08	-	-	+0.44 ± 0.15 ± 0.11
IC 4665									
17442711+0547196	53	13.8 ± 0.3	14.5 ± 1.0	−0.02 ± 0.25 ± 0.09	+0.49 ± 0.20 ± 0.09	-	-	-	+0.64 ± 0.15 ± 0.07
17445810+0551329	64	10.3 ± 0.4	10.0 ± 0.9	+0.04 ± 0.10 ± 0.07	+0.26 ± 0.12 ± 0.08	+0.24 ± 0.16 ± 0.09	-	-	+0.56 ± 0.10 ± 0.10
17452508+0551388	54	13.5 ± 0.2	13.5 ± 0.7	+0.13 ± 0.2 ± 0.10	+0.27 ± 0.17 ± 0.12	-	-	-	+0.61 ± 0.15 ± 0.12
NGC 2264									
06405694+0948407	135	18 ± 0.6	15 ± 3.8	−0.17 ± 0.15 ± 0.09	+0.31 ± 0.15 ± 0.07	+0.24 ± 0.1 ± 0.08	-	-	+0.41 ± 0.12 ± 0.08
NGC 2516									
07544342−6024437	73	4.2 ± 0.5	3**	−0.03 ± 0.11 ± 0.09	+0.12 ± 0.10 ± 0.07	+0.03 ± 0.10 ± 0.08	-	+0.03 ± 0.25 ± 0.10	+0.23 ± 0.16 ± 0.08
07550592−6104294	110	12.2 ± 0.3	11.8 ± 0.8	−0.17 ± 0.15 ± 0.1	+0.09 ± 0.12 ± 0.09	+0.06 ± 0.13 ± 0.08	-	-	+0.34 ± 0.10 ± 0.08
07551977−6104200	129	14.5 ± 0.4	14.6 ± 1.1	−0.15 ± 0.10 ± 0.09	+0.17 ± 0.15 ± 0.08	+0.15 ± 0.13 ± 0.07	-	-	+0.22 ± 0.10 ± 0.07
07553236−6023094	82	9.6 ± 0.4	9.2 ± 1.2	+0.08 ± 0.15 ± 0.11	+0.05 ± 0.13 ± 0.09	+0.06 ± 0.17 ± 0.10	-	-	+0.34 ± 0.09 ± 0.10
07564410−6034523	56	8.7 ± 0.4	7.9 ± 0.8	−0.12 ± 0.20 ± 0.09	+0.10 ± 0.20 ± 0.08	+0.05 ± 0.20 ± 0.10	-	-	+0.36 ± 0.15 ± 0.09
07573608−6048128	50	5.4 ± 0.8	4.6 ± 1.0	−0.02 ± 0.16 ± 0.10	+0.08 ± 0.20 ± 0.10	+0.06 ± 0.17 ± 0.09	-	-	+0.34 ± 0.15 ± 0.12
07574792−6056131	68	5 ± 0.4	3.2 ± 1.7	−0.04 ± 0.17 ± 0.07	+0.15 ± 0.13 ± 0.08	+0.13 ± 0.15 ± 0.09	-	-	+0.25 ± 0.10 ± 0.10
07575215−6100318	51	6 ± 0.8	5.5 ± 0.9	+0.05 ± 0.18 ± 0.12	-	+0.02 ± 0.15 ± 0.12	-	-	+0.24 ± 0.11 ± 0.09
07583485−6103121	100	12.5 ± 0.4	11.7 ± 1.3	-	+0.15 ± 0.20 ± 0.07	+0.03 ± 0.20 ± 0.08	-	-	+0.30 ± 0.10 ± 0.10
07584257−6040199	83	9.2 ± 0.3	8.8 ± 0.7	−0.12 ± 0.12 ± 0.07	+0.13 ± 0.20 ± 0.08	+0.11 ± 0.20 ± 0.08	-	-	+0.38 ± 0.10 ± 0.09
08000944−6033355	81	8.2 ± 0.4	7.2 ± 1.1	−0.13 ± 0.12 ± 0.09	+0.11 ± 0.10 ± 0.07	+0.07 ± 0.13 ± 0.08	-	-	+0.34 ± 0.15 ± 0.07
08013658−6059021	69	9.4 ± 0.3	8.9 ± 0.9	−0.17 ± 0.15 ± 0.08	+0.11 ± 0.20 ± 0.07	+0.04 ± 0.20 ± 0.09	-	-	+0.32 ± 0.12 ± 0.10
NGC 2547									
08102854−4856518	90	16 ± 0.4	15.3 ± 0.8	−0.12 ± 0.13 ± 0.09	+0.19 ± 0.17 ± 0.09	+0.12 ± 0.18 ± 0.09	-	-	+0.54 ± 0.15 ± 0.13
08110139−4900089	77	8.8 ± 0.3	8.8 ± 0.8	−0.02 ± 0.12 ± 0.09	+0.17 ± 0.15 ± 0.11	+0.15 ± 0.13 ± 0.09	-	-	+0.52 ± 0.12 ± 0.10

[a]: the identification name are taken from De Silva et al. (2013)

∗ : velocities taken from De Silva et al. (2013)

∗∗: values reported both in the DR5 and DR6, no error provided because it is an upper limit (VSINI FLAG=1);

Table 4.6: Individual abundances of the $s-$process elements derived with the lines in the 380-480 nm range. The first source of uncertainty (σ_1) is due to the best fit procedure, while the second (σ_2) is related to uncertainties in the stellar parameters (details on the computations can be found in Sec. 4.3.4).

	IC 2391						*IC 2602*
CNAME	08440521−5253171	08440521−5253171	08440521−5253171	PMM1142	PMM665	PMM4362	10440681−6359351
Instrument	UVES	FEROS	HARPS	UVES	UVES	UVES	HARPS
S/N	70	68	53	66	25	29	46
$v \sin i \pm \sigma$	18.4 ± 0.4	18.4 ± 0.4	18.4 ± 0.4	7.5 ± 0.4	8.2 ± 0.3	9 ± 0.3	12.1 ± 0.4
$v \sin i_{\text{lit.}}$	16.7 ± 0.8	16.7 ± 0.8	16.7 ± 0.8	7.3*	7.47*	8.61*	12.2 ± 0.7
$[\text{Sr/Fe}]_{\text{I}} \pm \sigma_1 \pm \sigma_2$	-	−0.05 ± 0.15 ± 0.08	−0.1 ± 0.20 ± 0.07	-	-	-	+0.03 ± 0.15 ± 0.09
$[\text{Sr/Fe}]_{\text{II}} \pm \sigma_1 \pm \sigma_2$	-	−0.08 ± 0.17 ± 0.09	−0.05 ± 0.20 ± 0.09	-	+0.03 ± 0.17 ± 0.10	−0.01 ± 0.17 ± 0.08	−0.04 ± 0.18 ± 0.08
$[\text{Y/Fe}]_{4398\text{Å}} \pm \sigma_1 \pm \sigma_2$	+0.3 ± 0.2	+0.25 ± 0.20 ± 0.08	+0.3 ± 0.25 ± 0.09	+0.31 ± 0.12 ± 0.10	+0.29 ± 0.16 ± 0.10	+0.20 ± 0.15 ± 0.11	+0.37 ± 0.30 ± 0.09
$[\text{Zr/Fe}]_{4050\text{Å}} \pm \sigma_1 \pm \sigma_2$	-	-	-	−0.01 ± 0.10 ± 0.08	+0.01 ± 0.17 ± 0.09	-	-
$[\text{Zr/Fe}]_{4208\text{Å}} \pm \sigma_1 \pm \sigma_2$	-	-	-	+0.03 ± 0.12 ± 0.07	+0.04 ± 0.20 ± 0.07	+0.03 ± 0.15 ± 0.08	-
$[\text{La/Fe}]_{3988\text{Å}} \pm \sigma_1 \pm \sigma_2$	−0.1 ± 0.10 ± 0.07	−0.10 ± 0.15 ± 0.07	−0.05 ± 0.20 ± 0.07	−0.11 ± 0.10 ± 0.08	−0.01 ± 0.12 ± 0.06	−0.06 ± 0.12 ± 0.07	−0.03 ± 0.25 ± 0.08
$[\text{La/Fe}]_{4087\text{Å}} \pm \sigma_1 \pm \sigma_2$	-	-	-	−0.06 ± 0.15 ± 0.06	−0.09 ± 0.13 ± 0.07	−0.08 ± 0.16 ± 0.08	+0.02 ± 0.30 ± 0.08
$[\text{Ce/Fe}]_{4073\text{Å}} \pm \sigma_1 \pm \sigma_2$	-	-	-	−0.03 ± 0.20 ± 0.07	+0.01 ± 0.15 ± 0.08	-	-

$*$: velocities taken from De Silva et al. (2013)

Table 4.7: Mean values of the abundance ratios [X/Fe] of the GBS and the YOCs, and comparison with the literature. The uncertainties for the GBS stars is the standard deviation of different lines (for Cu and Ba, for which we only analysed one line, the error is the quadratic sum of σ_1 and σ_2). The uncertainties of the mean abundances computed for our clusters are the errors on the mean, representing the star-to-star variation.

Star/Cluster	[Cu/Fe]	[Sr/Fe]	[Y/Fe]	[Zr/Fe]	[Ba/Fe]	[La/Fe]	[Ce/Fe]
α Cen A	+0.15 ± 0.20	−0.01 ± 0.01	+0.01 ± 0.04	−0.01 ± 0.04	+0.04 ± 0.15	−0.06 ± 0.03	−0.01 ± 0.01
Luck (2018)	+0.18±0.07	−0.08 ± 0.17	−0.01 ± 0.04	−0.07 ± 0.04	−0.12 ± 0.03	−0.07 ± 0.02	−0.04 ± 0.03
Casamiquela et al. (2020)	+0.07 ± 0.02	-	−0.07 ± 0.02	-	−0.11 ± 0.02	−0.01 ± 0.03	−0.11 ± 0.03
Casali et al. (2020b)	+0.11 ± 0.03	+0.03 ± 0.01	−0.01 ± 0.01	−0.07 ± 0.02	−0.07 ± 0.01	-	−0.06 ± 0.02
τ Cet	−0.08 ± 0.20	−0.06 ± 0.01	−0.11 ± 0.03	−0.04 ± 0.03	−0.12 ± 0.12	−0.03 ± 0.03	−0.03 ± 0.08
Luck (2018)	+0.08 ± 0.08	−0.12	−0.09 ± 0.02	+0.07 ± 0.05	−0.08 ± 0.01	+0.17 ± 0.06	+0.07 ± 0.04
Casamiquela et al. (2020)	+0.05 ± 0.02	-	−0.02 ± 0.02	-	−0.09 ± 0.02	+0.11 ± 0.04	−0.14 ± 0.08
β Hyi	−0.01 ± 0.15	−0.06 ± 0.01	−0.05 ± 0.01	−0.05 ± 0.04	−0.08 ± 0.17	−0.04 ± 0.02	−0.03 ± 0.03
Jofré et al. (2015a)	-	-	-	-	+0.09 ± 0.10	-	-
Bensby et al. (2014)	-	-	−0.12 ± 0.11	-	+0.03 ± 0.05	-	-
18 Sco	−0.02 ± 0.10	+0.055 ± 0.005	−0.06 ± 0.05	0.00 ± 0.01	−0.04 ± 0.15	+0.08 ± 0.03	+0.06 ± 0.04
Luck (2018)	−0.06 ± 0.04	−0.04 ± 0.17	+0.02 ± 0.02	+0.01 ± 0.09	+0.02 ± 0.01	+0.01 ± 0.02	+0.02 ± 0.03
Casamiquela et al. (2020)	−0.04 ± 0.02	-	+0.04 ± 0.01	-	+0.02 ± 0.01	−0.06 ± 0.03	−0.01 ± 0.04
Casali et al. (2020b)	−0.03 ± 0.02	+0.09 ± 0.01	+0.07 ± 0.01	+0.06 ± 0.01	+0.04 ± 0.01	-	+0.07 ± 0.01
IC 2391	−0.07 ± 0.02	−0.04 ± 0.05	+0.23 ± 0.03	+0.02 ± 0.02	+0.53 ± 0.02	−0.07 ± 0.03	−0.01 ± 0.02
D'Orazi et al. (2009a)	-	-	-	-	+0.68 ± 0.07	-	-
De Silva et al. (2013)	-	-	-	-	+0.62 ± 0.07	-	-
D'Orazi et al. (2017)	-	-	+0.08 ± 0.02	+0.09 ± 0.03	-	+0.14 ± 0.02	+0.15 ± 0.05
IC 2602	−0.10 ± 0.02	−0.01 ± 0.05	+0.19 ± 0.04	0.0 ± 0.35**	+0.40 ± 0.02	−0.01 ± 0.04**	
D'Orazi et al. (2009a)	-	-	-	-	+0.64 ± 0.07	-	-
D'Orazi et al. (2017)	-	-	+0.08 ± 0.02	+0.06 ± 0.01	-	+0.10 ± 0.02	+0.02 ± 0.02
Spina et al. (2021)	−0.15 ± 0.05	-	+0.17 ± 0.11	-	+0.34 ± 0.14	-	-
IC 4665	+0.05 ± 0.04	-	+0.34 ± 0.1	-	+0.60 ± 0.02	-	-
Spina et al. (2021)	−0.27 ± 0.05	-	+0.29 ± 0.16	-	+0.37 ± 0.16	+0.48 ± 0.05***	
NGC 2264*	−0.17 ± 0.15	-	+0.28 ± 0.05	-	+0.41 ± 0.12	-	-
NGC 2516	−0.06 ± 0.03	-	+0.09 ± 0.04	-	+0.31 ± 0.03	-	+0.03 ± 0.25**
D'Orazi et al. (2009a)	-	-	-	-	+0.41 ± 0.04	-	-
Maiorca et al. (2011)	-	-	+0.16 ± 0.03	-	-	-	+0.18 ± 0.02
Magrini et al. (2018)	-	-	+0.11 ± 0.06	+0.58 ± 0.07	+0.20 ± 0.08	-	+0.38 ± 0.10
NGC 2547	−0.07 ± 0.05	-	+0.16 ± 0.01	-	+0.53 ± 0.01	-	-

*: since we analysed only one star in this SFR, we reported the individual abundance values and the uncertainties on the fitting procedure.
**: measurement based on only one target
***: values affected by strong blends (Buder et al. 2020)

PMM 4362, and $-0.55\,\mathrm{km\,s^{-1}}$ for star PMM 1142, respectively. Such significant differences in ξ parameter reflect on the abundances derived. An increase of $\sim 0.6\,\mathrm{km\,s^{-1}}$ in the ξ values results in decrease of $\sim$ 0.2 dex in [Fe/H] and of $\sim$ 0.3 dex in Y abundance, which is derived from moderately strong lines. Instead, the same variation produces a negligible change of La abundance, for which only weak lines have been used. Thus, the sensitivity to variations of the ξ parameter depends mainly on the strength of the line. For star PMM 1142 the new spectroscopic T_{eff} value is 300 K lower than what found by DS13, mostly due to the different line lists used. However, my spectroscopic T_{eff} is corroborated by the estimates derived using 2MASS photometry (Cutri et al. 2003) and using the relations by Casagrande et al. (2010), which are equal to $T(J-K) = 5378 \pm 105$ K, $T(V-J) = 5386 \pm 135$ K, $T(V-H) = 5408 \pm 153$ K and $T(V-K) = 5380 \pm 155$ K.

The final abundances of the individual stars can be found in Table 4.5 for the red spectral setup and Table 4.6 for the blue range, respectively. The uncertainties σ_1 and σ_2 indicated in both tables are calculated as described in Sec.4.3.4. The mean cluster abundances for each elements are given in Table 4.7; in this case, the uncertainties were computed as the error on the mean. Note that these mean values come from the averaged abundances of redder and bluer spectral ranges. For NGC 2264 I analysed only one star, therefore, I assumed as a conservative error value the uncertainty in the fitting procedure. For completeness, I report also the $v\sin i$ measured as described in Section 4.3.3 along with values derived by the OACT node of the *Gaia*-ESO consortium ($v\sin i_{\mathrm{lit.}}$), as well as the S/N ratios. The mean difference (and error on the mean) between my $v\sin i$ and the OACT values is equal to $0.6 \pm 0.2\,\mathrm{km\,s^{-1}}$, with a standard deviation σ=0.8 $\mathrm{km\,s^{-1}}$: overall my measurements are in good agreement with the OACT node results.

As it can be seen in Table 4.7, only IC 2391, IC 2602 and NGC 2516 were previously extensively studied. Regarding the first two clusters, the mean values of [Ba/Fe] obtained here confirm the overabundance already pointed out by D'Orazi et al. (2009a) (for IC 2391 and IC 2602) and De Silva et al. (2013) (for IC 2391 only). My estimate is lower by 0.15 dex for IC 2391 and by 0.24 dex for IC 2602 than the value reported by D'Orazi et al. (2009a). Such difference could be related to different techniques and lines used, since D'Orazi et al. (2009a) derived the Ba abundance from the EW of lines at 5853.7 Å and at 6496.9 Å, while here we use the spectral synthesis only for line at 5853.7 Å. Moreover, there is a difference in the adopted solar abundances between the two studies: D'Orazi et al. (2009a) derived a $\log(\mathrm{Ba})_{\odot}$ equal to 2.22 dex, which is 0.09 dex lower than our adopted value. For IC 2391 I found a value of [Ba/Fe] lower than De Silva et al. (2013) by 0.09 dex, which is in fair agreement within the observational uncertainties.

When focusing on the other *s*-process elements, I detect a mild enhancement for [Y/Fe], at $\sim$ 0.3 dex level, higher with respect to the values reported by D'Orazi et al.

Table 4.8: Atmospheric parameters and abundances of Fe and Ti derived with the new approach of the stars from D'Orazi et al. (2017). The uncertainties are due to the dispersion among different atomic lines (first value) and to uncertainties on the stellar parameters (second value).

ID	$T_{\rm eff}$	log g	ξ	$[\rm Fe/H]_{I}$	$[\rm Fe/H]_{II}$	$[\rm Ti/H]_{I}$	$[\rm Ti/H]_{II}$
PMM 1142	5400 ± 100	4.28 ± 0.07	0.95 ± 0.10	0.00 ± 0.02 ± 0.07	+0.11 ± 0.03 ± 0.06	+0.04 ± 0.02 ± 0.10	+0.06 ± 0.03 ± 0.05
PMM 665	5425 ± 100	4.47 ± 0.05	1.01 ± 0.15	+0.08 ± 0.02 ± 0.07	+0.14 ± 0.05 ± 0.06	+0.10 ± 0.02 ± 0.11	+0.11 ± 0.05 ± 0.05
PMM 4362	5550 ± 100	4.35 ± 0.05	0.97 ± 0.15	+0.13 ± 0.02 ± 0.08	+0.14 ± 0.04 ± 0.06	+0.09 ± 0.03 ± 0.11	+0.12 ± 0.02 ± 0.05

(2017) by Δ[Y/Fe]=+0.15 dex and Δ[Y/Fe]=+0.11 dex for IC 2391 and IC 2602, respectively. This can be simply explained by the difference in the ξ values, which impacts the abundances derived from strong lines. Instead, [Zr/Fe], [La/Fe] and [Ce/Fe] exhibit solar values, as in D'Orazi et al. (2017). For [La/Fe] of IC 2602, the mean value is calculated only on the values derived from the two lines in the blue range measured in the star 10440681−6359351. Regarding the abundances in the red for Zr in IC 2602, I rely only on one measurement, for the star 10442256−6415301. For this star, I obtained [Zr/Fe]=0.0 ± 0.35 ± 0.1, where the large uncertainty on the fit is due to the poor quality of the spectrum. On the other hand, the determination of Zr abundance measurement for the star 10440681−6359351 (in the blue wavelength domain) is hampered by the very low S/N ratio in the HARPS spectrum.
For both IC 2391 and IC 2602, I present in this work the first estimates of [Cu/Fe] and [Sr/Fe].

For NGC 2516, the third most studied cluster in the list, my mean [Ba/Fe] estimate of +0.31±0.03 lies in between the results of D'Orazi et al. (2009a) (+0.41 ± 0.04, determined through EWs) and Magrini et al. (2018) (+0.20 ± 0.08, the average value of the results in the *Gaia*-ESO iDR5 catalogue). The new [Y/Fe] is in very good agreement within the errors with Maiorca et al. (2011) (+0.16 ± 0.03), while larger differences for [Ce/Fe] could be noted between the two studies. My findings confirm a solar [Ce/Fe] for NGC 2516, while Maiorca et al. (2011) and Magrini et al. (2018) reported +0.18 ± 0.02 and +0.38 ± 0.10, respectively. However, I measured Ce only in one star, namely 07544342−6024437. The discrepancy between my results and the literature values could be due to the different techniques used.

The cluster IC 4665 was recently used by Spina et al. (2021) in his study of Galactic OCs observed within the GALAH survey (Buder et al. 2020) (for which I considered only the results obtained with the dwarf stars). As it can be seen in Table 4.7, there is a large discrepancy between my [Cu/Fe] and the value of Spina et al. (2021), possibly due to the different line lists, techniques, stars per clusters analysed and the lower resolution of the spectra analysed, which can affect the measurements in crowded regions. The measured [Y/Fe] ratios in both studies agree very well and we found fairly good agreement also for [Ba/Fe]. In the Table, we reported also the value of [La/Fe], for which however caution should be paid, as stated in Buder et al. (2020). These measurements could be affected by heavy blends of La lines used in the analysis in the GALAH survey.

Finally, for NGC 2547, and the SFR NGC 2264, this is the first time the abundances of the s-process elements are determined. I obtained over-solar abundances of [Ba/Fe], mild enhancement of [Y/Fe] and solar values of [Cu/Fe].

4.4.3 Trends with stellar parameters

In Figure 4.2, 4.3 and 4.4, the [X/Fe] ratios as a function of the stellar parameters $T_{\rm eff}$, $\log g$ and $v\sin i$, respectively, are plotted. In these plots, the points are colour-coded according to the age. There are no significant trends with the stellar parameters, which validates the spectroscopic analysis. As it can be seen from the bottom-left panel, I obtained the super-solar [Ba/Fe] ratios, more evident at younger ages, with values between roughly +0.25 and 0.65-0.70 dex. Curiously, my [Y/Fe] estimates (top-right and bottom-right panels) indicate also a mild enhancement going toward younger ages, ranging between +0.1 up to +0.25 dex, at variance with the solar values previously found by some authors (e.g., D'Orazi et al. 2012, 2017). Regarding Y, none of the trends with the stellar parameters is significant.

For both elements (Y and Ba), a sharp separation between the blue dots (the youngest stars, with ages less than 50 Myr) and the red dots (the oldest stars in the sample with an age of ~150 Myr) can be seen. For Cu, instead, the results are homogeneously distributed with the age.

4.5 Discussion

As already mentioned in Section 4.1, it is not possible to reconcile the super-solar abundances of Ba together with solar La and Ce abundances with the predictions of the *s*-process and *r*-process nucleosynthesis models (e.g., Kobayashi et al. 2020 and references therein), without invoking other processes. On the other hand, the enrichment of Y with respect to Sr and Zr is less clear, and need to be studied in more details. A large variety of processes can contribute to the production of elements in the Sr-Y-Zr region, which could have caused the variations observed in YOCs. Together with the nucleosynthesis processes mentioned in the previous sections (the *s*-process, the *i*-process and the *r*-process), elements in this mass region may be also made in different neutrino-wind components from CCSNe (e.g., Farouqi et al. 2009; Roberts et al. 2010; Arcones & Montes 2011) and in electron-capture supernovae (e.g., Wanajo et al. 2011; Jones et al. 2019). However, as discussed in this work, the Y enhancement could be caused by some observational issue.

The difficulty may be related to the spectral analysis and mechanisms that are at work on the photosphere of a young star to magnify the Ba abundance, and/or to the nucleosynthesis processes that produce the elements heavier than Fe in the Galaxy. Below, I discuss both possibilities: in Section 4.5.1, the problems that may be related to the spectra lines and in Section 4.5.2 the potential issues with GCE models.

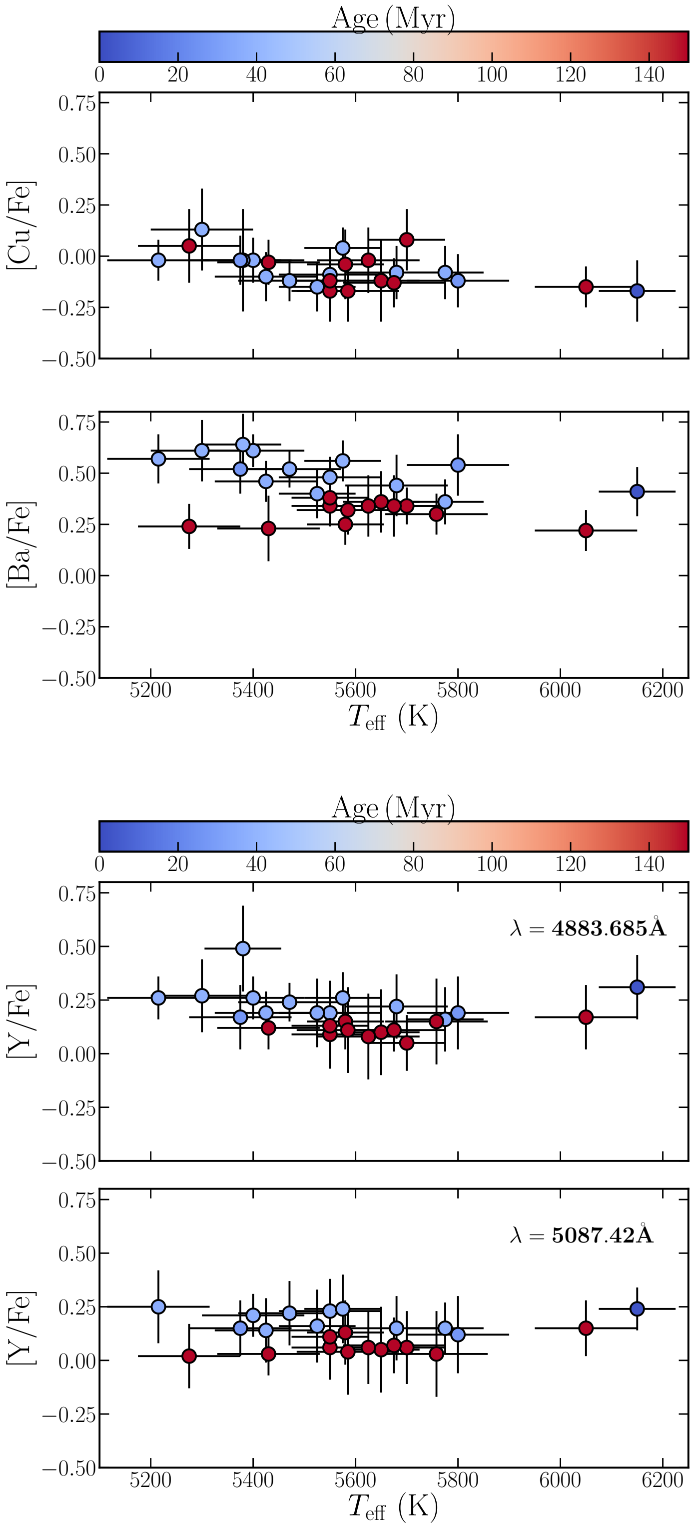

Figure 4.2: [X/Fe] as a function of $T_{\rm eff}$, where the points are colour-coded according to the age.

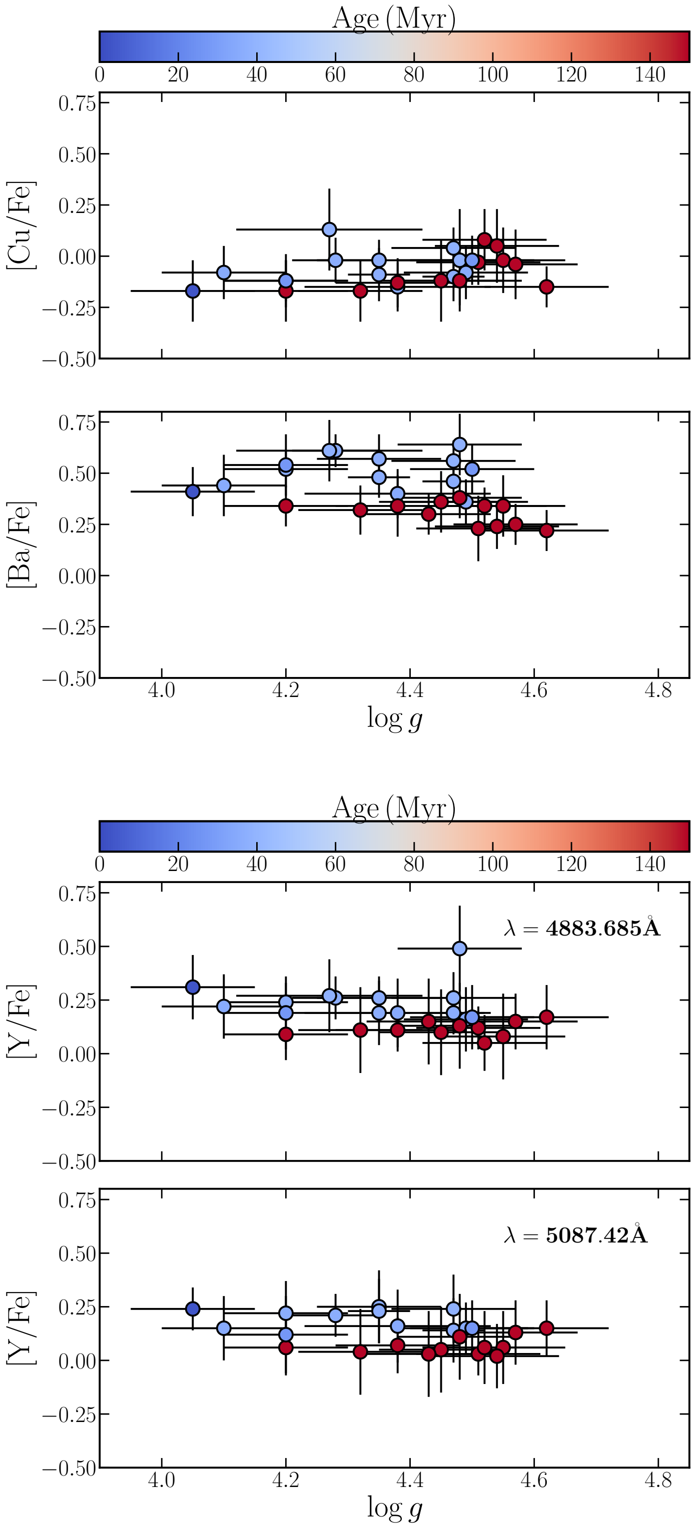

Figure 4.3: [X/Fe] as a function of log g, where the points are colour-coded according to the age.

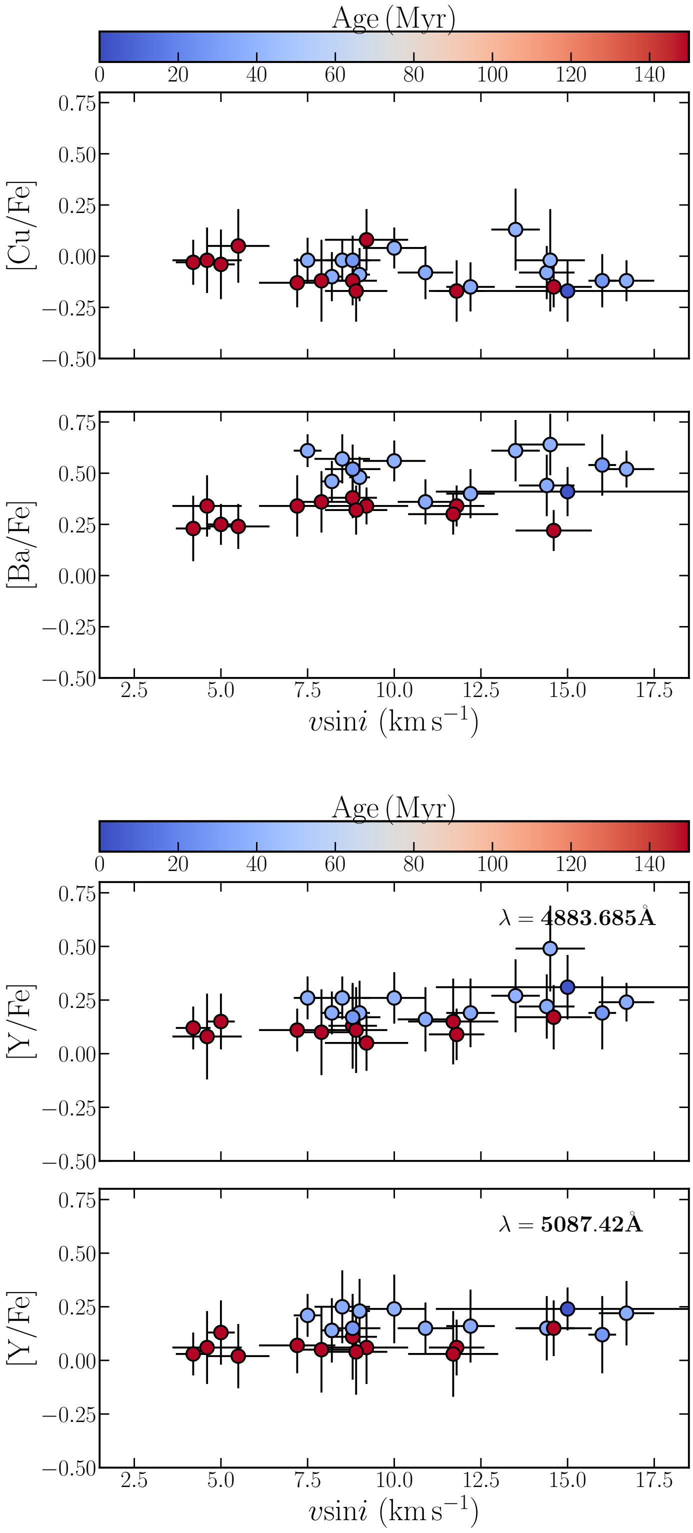

Figure 4.4: [X/Fe] as a function of $v \sin i$, where the points are colour-coded according to the age.

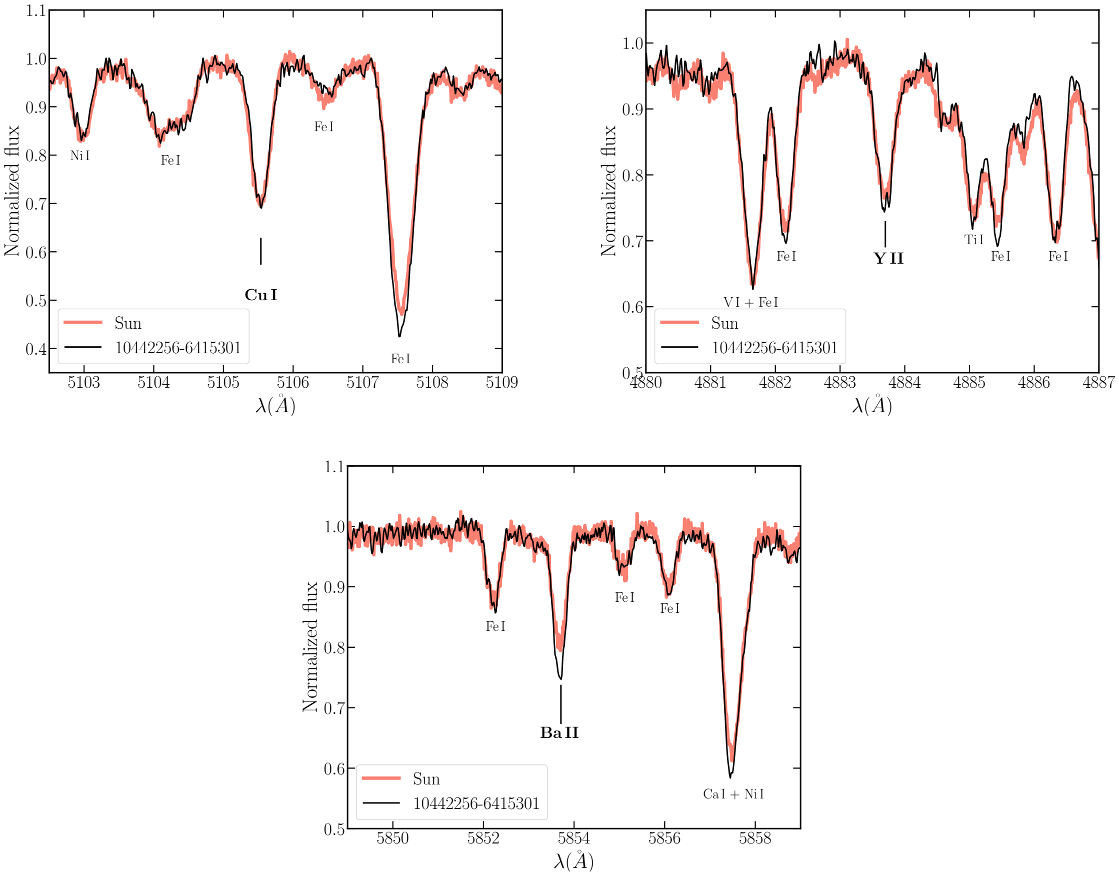

Figure 4.5: Comparison of Cu I line at 5105.54 Å (top-left panel), Y II line 4883.69Å (top-right panel) and Ba II line at 5853.7 Å (bottom panel) between the Sun (light pink line, age ~4 Gyr) and the young star 10442256−6415301 (black line, age ~35 Myr).

4.5.1 Behaviour of spectral lines

Since the observed Ba overabundance and the slightly super-solar values of Y cannot be reconciled with nucleosynthesis models predictions, we believe that the key in understanding the Ba puzzle might rely in the age of the stars. The younger the star, the higher the levels of its activity, both at the level of the chromosphere and/or of photospheric magnetic fields. This in turn can result in an alteration of the photospheric structure and, consequently, an alteration of the profile (i.e., strengths) of the spectral lines. Thus, in young stars it is important to know where the line forms in the photosphere and how it is affected by magnetic activity, as already demonstrated by Spina et al. (2020).

Looking at Table 4.2, where the optical depths of line formation are listed, it is evident that the line at 5105.54 Å of Cu and line at 5853.7 Å of Ba form at similar depths, with $\log \tau_{5000\ \mathrm{core}}$ of −3.4 and −3.2, respectively. Thus, I would expect to observe the same effects in both elemental abundances derived through these lines. Nonetheless, I obtained solar values of [Cu/Fe], while [Ba/Fe] is enhanced (between +0.25 and +0.70 dex). This is also confirmed from Figure 4.5, where the spectrum of the Sun (light pink line) with the solar analog 10442256−6415301 (black line) that belongs to IC 2602 (age ~ 35 Myr) are compared. In these plots, the solar spectrum is convolved with a rotational profile with $v \sin i = 11\ \mathrm{km\,s^{-1}}$, to match the $v \sin i$ of the young star, and a Gaussian noise is added to obtain S/N=110 (I used the iSpec tool by Blanco-Cuaresma et al. 2014a). Both lines are strong, but the Ba line (bottom panel) is deeper in the younger stars, while the profiles of Cu line (top panel) are identical. In fact, for the star 10442256−6415301 I obtained [Ba/Fe]=+0.36 ± 0.11, while [Cu/Fe]=−0.08 ± 0.13, solar within the uncertainties. Nevertheless, the different ionisation stages of the two species (i.e., neutral Cu *vs.* singly-ionised Ba) could (at least partially) explain the observed behaviour. In the following I investigate neutral and ionised lines of other species.

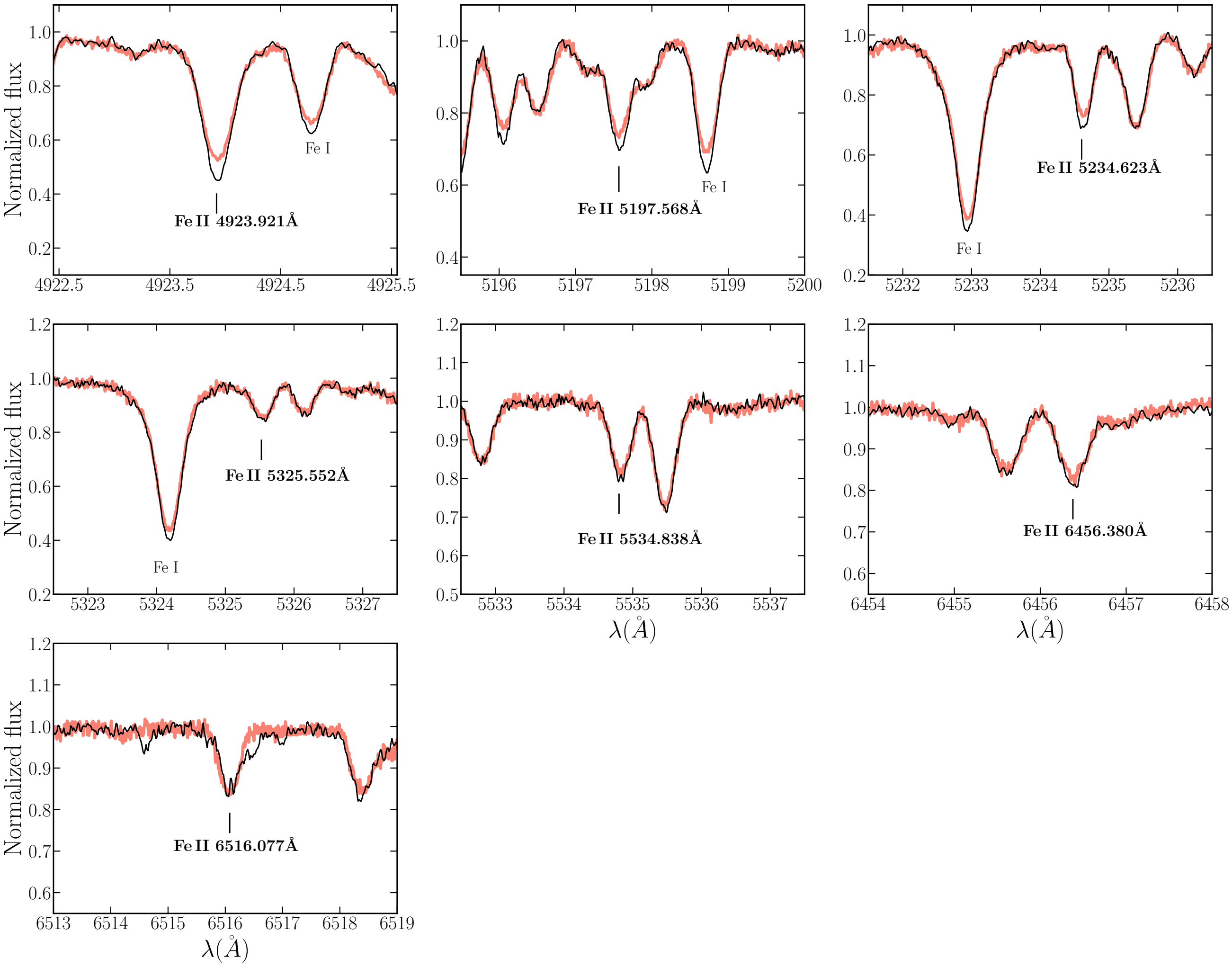

Figure 4.6: Comparison of Fe II line profiles in the Sun (light pink), with a rotational profile of $11\ v \sin i\ \ \mathrm{km\,s^{-1}}$, and star 10442256−6415301 (black).

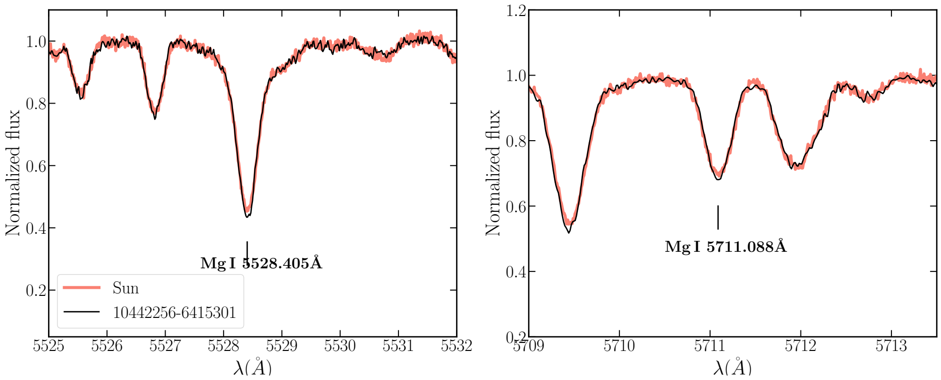

Figure 4.7: Comparison of Mg lines in the Sun (light pink) and star 10442256-6415301 (black).

It has been observed that strong ionised lines of Fe, Ti and Cr yield large abundances in young and cool ($T_{\rm eff}$ <5400 K) stars (see e.g., D'Orazi et al. 2009a; Schuler et al. 2010; Tsantaki et al. 2019; Baratella et al. 2020a). This is referred to as the ionisation balance problem. Aleo et al. (2017) explain this effect as due to the presence of undetected blends in the ionised lines (in particular of Fe) that become more severe in the cool regime. To investigate this, I selected a set of seven strong Fe II lines that have been initially excluded from the analysis in Chapter 2. For each line in Figure 4.6 I compare the spectra of the Sun and star 10442256−46415301, as done in Figure 4.5. The majority of Fe II lines (butnot all of them) is deeper in the young star than in the Sun, as observed for the Ba II line. This is also corroborated by the measured EWs and abundances obtained from the Fe II lines (computed by adopting the stellar parameters of Paper I), as it can be seen in Table 4.9.

However, even lines of neutral species show a behaviour similar to the ionised lines. From Figure 4.6 it is evident that Fe I (e.g., in the first and second panel of the figure) are stronger in the young star than in the Sun. In the bottom panel of Figure 4.5 the blend Ca I+Ni I at 5857.5 Å behaves similarly to Fe I. I then compared the two spectra in small windows around two Mg I lines, in Figure 4.7, and eight Ca I lines, Figure 4.8. As it can be seen, the profiles of Mg lines are almost identical. Instead, for Ca the weak lines (panels

Table 4.9: Abundances of the individual strong Fe II lines from EW measurements in the Sun (Column 4 and 5) and the young solar-analog 10442256−6415301 (IC 2602, age ~ 35 Myr, Column 6 and 7).

λ	E.P. (eV)	log gf	EW$_\odot$ (mÅ)	log(Fe)$_\odot$	EW$_\star$ (mÅ)	log(Fe)$_\star$
4923.92	2.89	-1.26	157.00	7.06	186.00	7.24
5197.57	3.23	-2.22	89.60	7.37	104.00	7.55
5234.62	3.22	-2.18	85.57	7.36	95.24	7.48
5325.55	3.22	-3.16	40.38	7.34	43.25	7.39
5534.84	3.25	-2.87	62.66	7.45	73.40	7.61
6456.38	3.90	-2.19	64.30	7.51	68.00	7.54
6516.08	2.89	-3.31	63.83	7.64	76.70	7.85

on the left) have similar depths, while the strong lines (panels on the right) are deeper in the young star (black line) than in the Sun (light pink line).

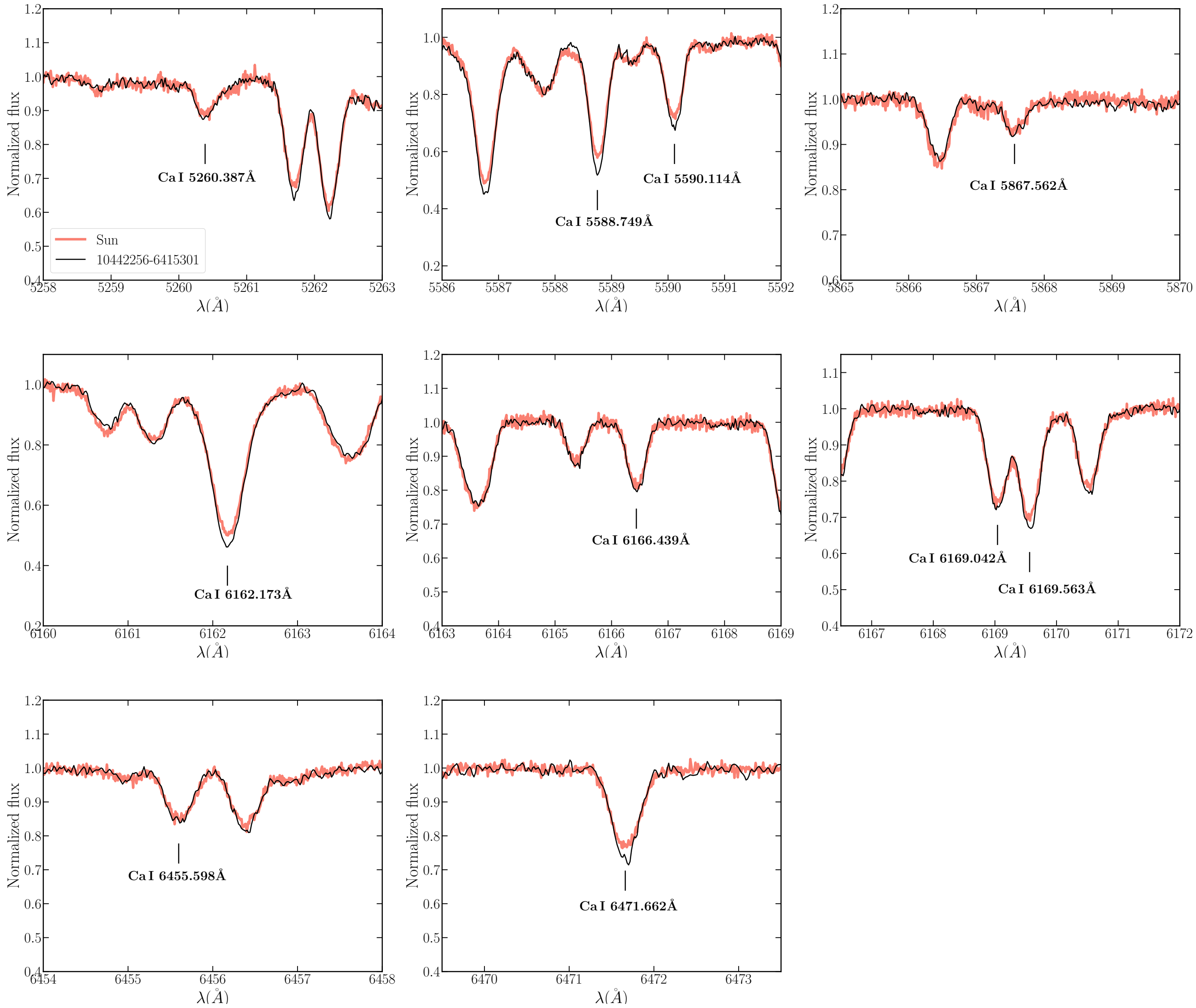

Figure 4.8: Comparison of Ca lines in the Sun (light pink) and star 10442256-6415301 (black).

Barium and Sr belong to the same group in the periodic table, so they have similar outermost electron shell configurations and they share similar nucleosynthetic origins. Hence, we should witness some effects also on Sr abundances, for which I exploited lines at 4607.33 Å of Sr i (Δ_{NLTE}=+0.1 dex) and 4215.52 Å of Sr ii. As it can be seen in Table 4.6, there is good agreement between the Sr i and Sr ii abundances, at least in stars 0844052−5253171 (IC 2391) and 10440681−6359351 (IC 2602). In general, [Sr/Fe] is solar in both cases. Looking at the depth of formation (Table 4.2), the Sr i line forms deeper in the photosphere than the Ba line. This might in principle explains why I obtained solar-scaled abundances. Conversely, the Sr ii line forms at $\log\tau_{5000}$ =−5.2, so in the upper layers. However, when deriving the abundance of Sr ii, I obtained again a solar composition, as it can be seen from Figure 4.9, where I plot the best-fit models of Sr ii lines in the Sun, star 08440521-5253171 (IC 2391) and τ Cet.

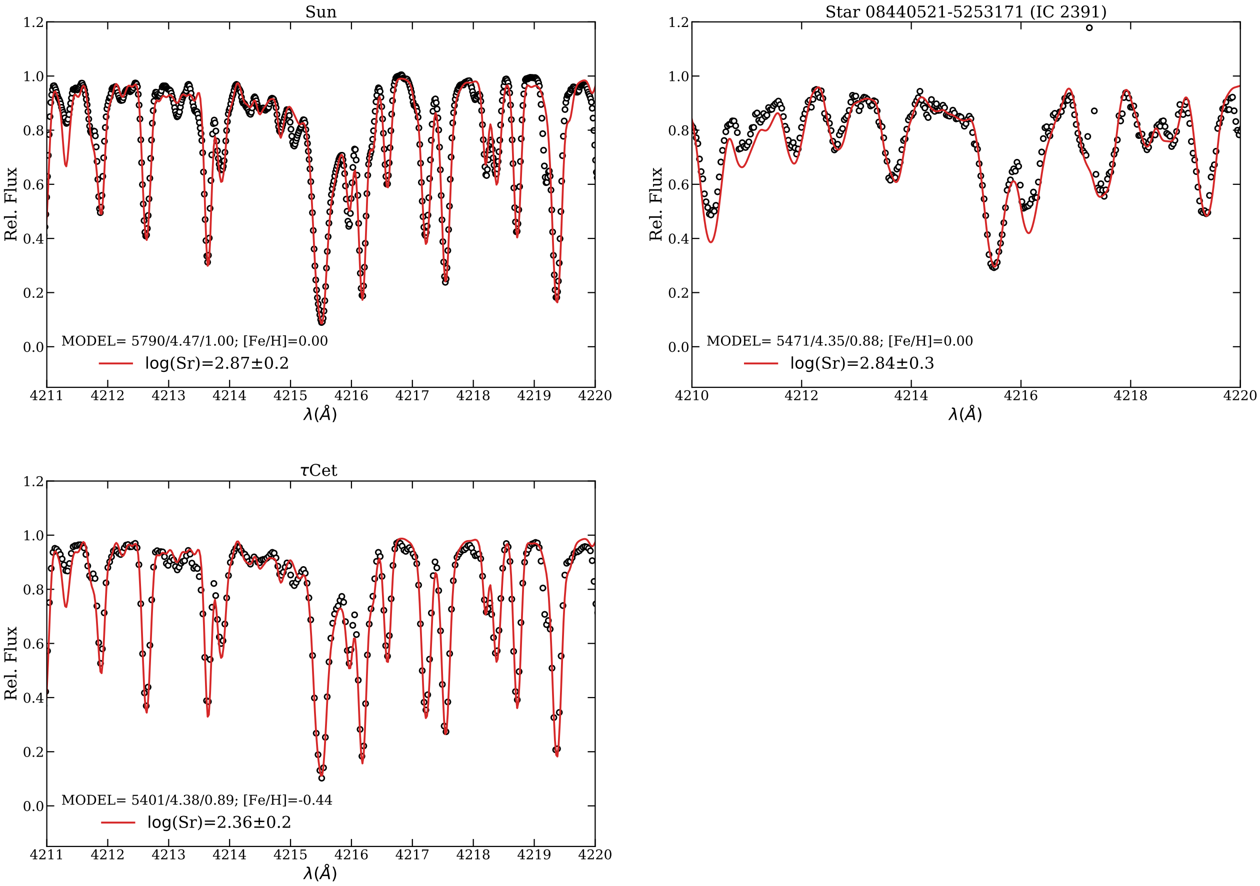

Figure 4.9: Best fit models (full-red lines) of Sr ii lines in the Sun (UVES spectrum – top-left panel), star 08440521-5253171 of IC 2391 (FEROS spectrum – top-right panel) and τ Cet (FEROS spectrum – bottom panel). The open circles represent the observed spectra.

Regarding the Y lines at 4883.69 Å and at 5087.42 Å, they form at a similar depth, with $\log\tau_{5000\ \mathrm{core}}$ equal to −2.6 and −2.1, respectively. From the comparison of the solar and the young solar-analog spectra in Figure 4.5 (central panel), it can be seen that the Y II line at 4883.69 Å is stronger in the young star than in the Sun. This is in compliance with the derived abundance estimates. Interestingly, La II lines analysed in this work should exhibit a behaviour similar to the Y II features (they share formation depths, ionisation stage and nucleosynthesis channels). Nevertheless, La abundances are solar, whereas [Y/Fe] are enhanced.

Finally, in Figure 4.10 I compare Sc I and Sc II lines in the same way as in Figure 4.5. Scandium has the same electronic configuration as Y and similar to La, so it is expected that these elements show a similar behaviour. Instead, from Figure 4.10 it is evident how the profile of both neutral and ionised Sc lines are the same in the Sun and in the young star. In this case, there are no differences between the two spectra, for any line, with the exception of line 5658.361 Å. The small difference seen in this line may be due to a blend with a nearby Fe I line.

In conclusion, line formation depth and ionisation stages of the elements are not able to fully explain the very peculiar pattern of *s*-process elements in young open clusters. On the other hand, we cannot exclude that different (conspiring) mechanisms could be simultaneously at work. Looking at Figure 4.11, there seems to be a correlation between the larger abundances of Y and Ba with decreasing log R'_{HK} (i.e., higher levels of stellar activity). I considered the log R'_{HK} values computed previously , which were derived from the X-ray luminosities found in literature and using the conversion relation by Mamajek & Hillenbrand (2008). The X-ray luminosities (and hence the log R'_{HK} values) are not synchronous to our spectra, and consequently, to the derived abundances. Nevertheless, globally, we could conclude that indeed there is an *indication* of a correlation between the [Y/Fe] and [Ba/Fe] and log R'_{HK} (not so evident for [Cu/Fe]). This plot surely deserve an in-depth investigation and further observations are needed to study the behaviour at log $R'_{HK} > -4.0$ and log $R'_{HK} < -4.4$.

Spina et al. (2020) proposed magnetic intensification as a possible explanation of the anomalous Ba (and of other elements) abundances. In Biazzo et al. (2017), this possibility is also explored. Indeed, given the young age of our targets, this seems to be a promising solution. The presence of magnetic fields cause the atomic levels to be split in different component according to the Zeeman effect. This results in a broadening of the spectral line, with increased EWs and reduced line depth, which however is not seen in our lines (see Figure4.5). The amount of splitting is directly proportional to g_L, the square of the wavelength and the magnitude B of the magnetic field. To evaluate the sensitivity to magnetic fields of each line, I computed the Landé factor g_L (Column 7 of Table 4.1) as described in Section 4.3.1. The selected lines have globally $g_L < 1.3$, which are relatively low. Looking at the Ba and Cu lines, they have very similar g_L, equal to 1.07 and 1.10,

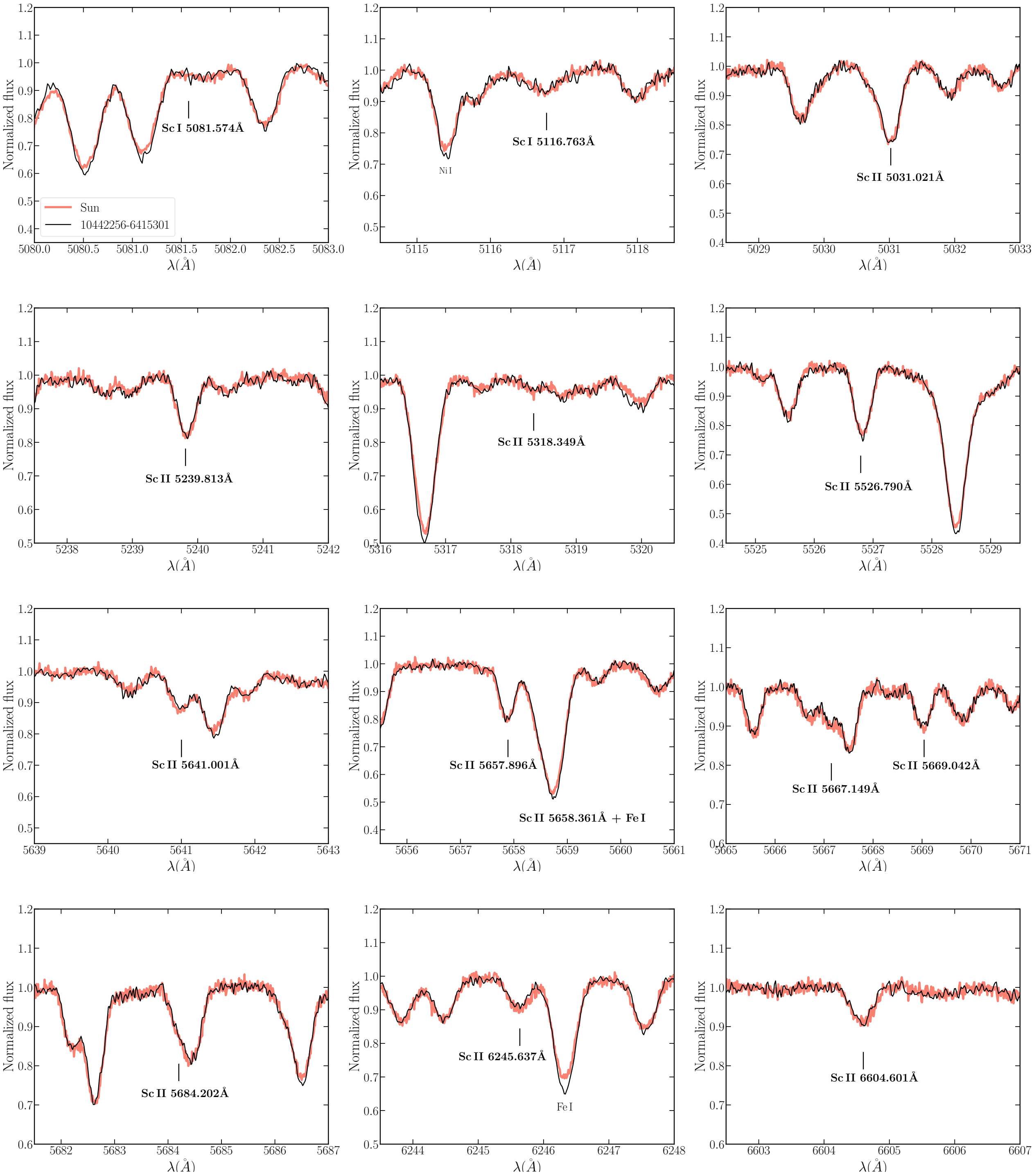

Figure 4.10: Comparison of Sc line profiles in the Sun (light pink line), with a rotational broadened profile of 11 km s^{-1}, and star 10442256-6415301 (black line).

respectively. Nevertheless, I obtained super-solar Ba abundance and solar Cu. The La line at 3988.5 Å has $g_{\rm L}$ = 1.33, which is the largest value, but I obtained solar abundance. Thus, the magnetic intensification cannot explain the large values obtained.

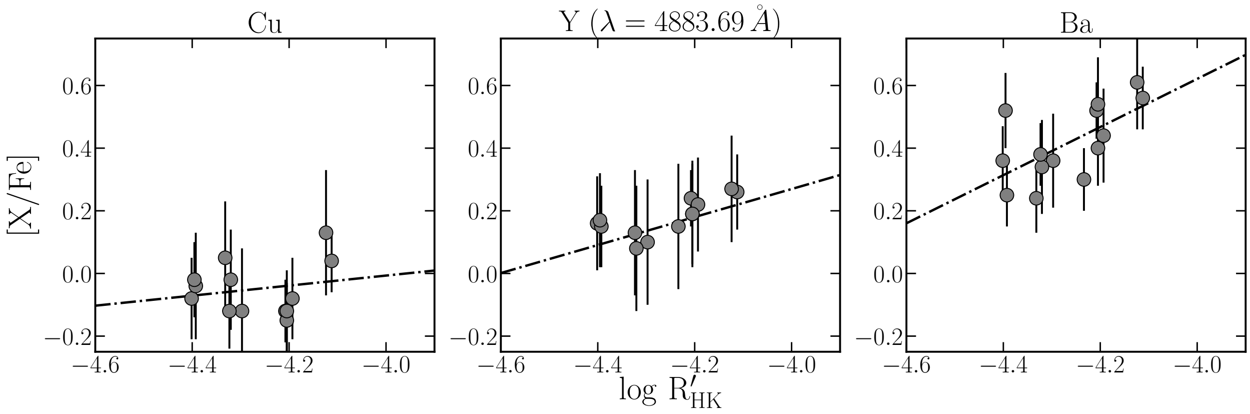

Figure 4.11: [X/Fe] as a function of log R$'_{\rm HK}$, computed following Mamajek & Hillenbrand (2008) from the log ($L_{\rm X}/L_{\rm bol}$) (details on the computation could be found in Paper I). The dot-dashed lines are the linear fit of the measurements.

Another possibility is the first ionisation potential (FIP) effect, and the lines used in the analysis, in particular Ba, seem to be a suitable candidate to show this. It has been shown that the coronal abundances derived from lines with FIP below 10 eV in the Sun are enhanced with respect to the photospheric values (see, e.g., the review by Laming 2015). Sheminova & Solanki (1999) explored the idea that the gas exhibiting the FIP effect in the corona is connected to the photosphere through magnetic flux tubes, generated from magnetic elements or sunspots present on the surface. In principle, the enhancement observed in the corona could be reflected also on photospheric abundances. The FIP values (Column 8 of Table 4.1) were retrived from Gray (1992). As it can be seen, Ba and La lines have similar FIP, therefore, this does not explain their discrepant abundances. However, the higher levels of activity due to the very young ages of our stars could be completely different than what is observed in other active, older stars.

In summary, all the possible effects described above may play a role, however, there is no convincing evidence that any of them provide a definitive solution, yet.

4.5.2 The Galactic chemical evolution of *s*-process elements at young ages.

In Figure 4.12 the Ba (top-left panel), Y (top-right panel), La (bottom-left panel) and Cu (bottom-right panel) abundance ratios are plotted as a function of the age of the Galactic OCs. My measurements are compared with different studies found in the literature, as indicated in the caption of the figure. For all the clusters in the different samples, I considered the ages from Cantat-Gaudin et al. (2020),who reported that the uncertainties in log t for young clusters ranges from 0.15 to 0.25, while for old cluster from 0.1 to 0.2.

The [Ba/Fe] time evolution, with increasing values at decreasing ages, is well confirmed by the observational data and now a significant scatter at young ages can be also detected. In particular, for the SFR NGC 2264 (age ≈ 5 Myr), the Lupus region (age ~3 Myr), and for Orion subgroup Ic (age ~3 Myr), the values are [Ba/Fe]≈+0.4 dex (this study), [Ba/Fe]≈0.7 dex (Biazzo et al. 2017), and [Ba/Fe]≈0.1 dex (Reddy & Lambert 2015), respectively. This large scatter between the different [Ba/Fe] at $\log t \sim 6.5$ can not be fully explained with the adopted microturbulence values and it certainly reflects fundamental issues in the analysis of such young stars. The solution of magnetic intensification proposed by Spina et al. (2020) can only partly explain the problem: the analysis presented in this work suggests that we are witnessing an additional effect. A similar rising trend, although of much smaller extent, emerges when Y is considered. Like Ba, La belongs to the second peak of the *s*-process elements. As it can be seen in the bottom-left panel of Figure 4.12, my measurements confirm solar values even at ages where [Ba/Fe] is extremely enhanced, as indicated in previous works (e.g., D'Orazi et al. 2012; Reddy & Lambert 2015; Mishenina et al. 2015). Finally, I found in literature only few studies where Cu abundance was derived for OCs, namely Frasca et al. (2019), Casamiquela et al. (2020), Donor et al. (2020) (near-infrared measurements), and Spina et al. (2021). From the bottom right-hand panel of Figure 4.12, it is evident that [Cu/Fe] is solar (within uncertainties) at all ages; note the large scatter of the measurements, especially at younger ages.

In Figure 4.13 the individual [X/H] of Ba, Y and La, [Cu/Mg], [Ba/La] and [Y/Mg] ratios are displayed as a function of age, and they are compared with the predictions from the GCE models of Magrini et al. (2021). The recent production of the first-peak, Y, and second peak, La and Ba, *s*-process elements is mainly driven by the evolution of AGB stars, with lower percentages coming from massive stars in the early Galactic epochs (see, e.g., Cescutti & Chiappini 2014 for a summary of the variety of possible scenarios). In low-mass AGB stars, the neutrons necessary to the production of *s*-process elements are mainly provided by the so-called ^{13}C pocket, which forms at the bottom of the convective envelope after each third dredge-up episode (Cristallo et al. 2009). The extension of the ^{13}C pocket plays a major role in the final production of neutron capture elements, and it can be parametrised in different ways. The GCE models adopted here consider the *s*-process yields from the FRUITY models, calculated by applying a simple exponentially decreasing profile of the convective velocities at the inner border of the convective envelope (Cristallo et al. 2009), and the MAGN models, a recent revision of the FRUITY yields which include the mixing triggered by magnetic fields (Vescovi et al. 2020), which could explain the behaviour of [Y/Mg] in open clusters at different Galactocentric distances (Magrini et al. 2021).

As it can be seen, the GCE models considered here cannot reconcile the time evo-

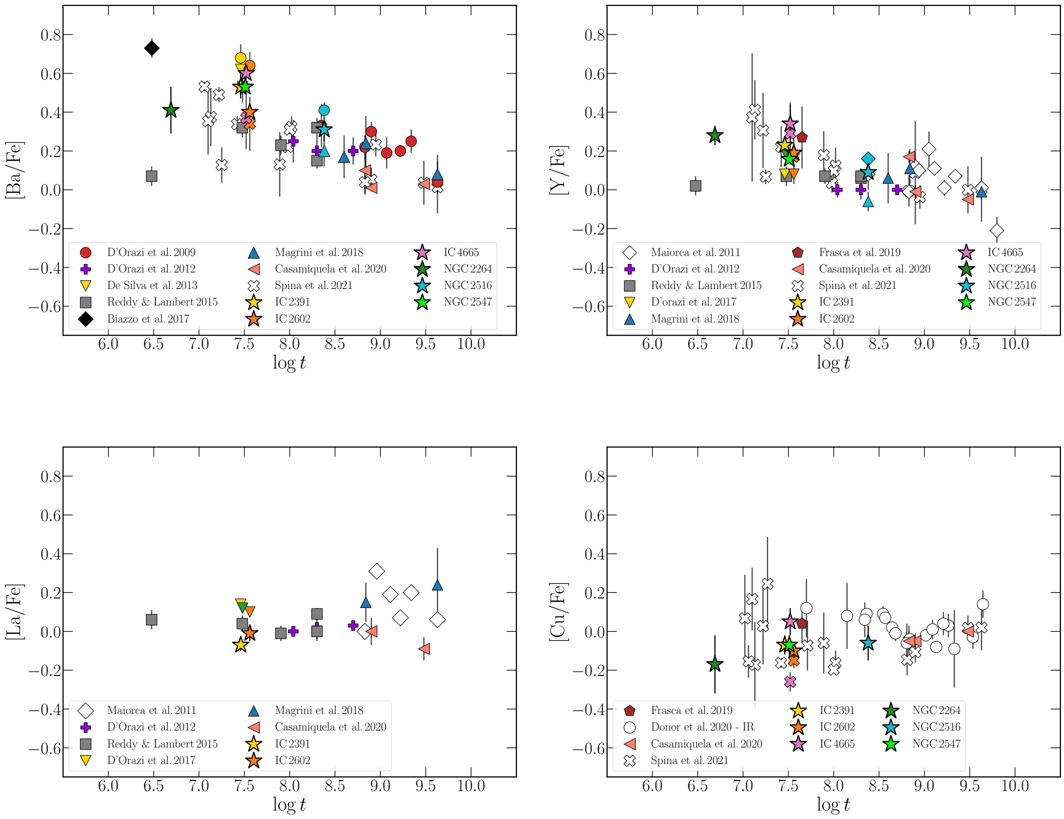

Figure 4.12: [Ba/Fe] (top-left panel), [Y/Fe] (top-right panel), [La/Fe] (bottom-left panel) and [Cu/Fe] (bottom-right panel) as a function of the age of Galactic open clusters with $7.5{<}R_{GC}{<}9$ kpc. The ages are from Cantat-Gaudin et al. (2020): the typical uncertanties for $\log t$ young clusters is 0.15-0.25, while for old OCs is 0.1-0.2 . Star-like symbols are the estimates derived in this work. Red circles are from D'Orazi et al. (2009a); empty diamonds are taken from Maiorca et al. (2011); purple crosses are from D'Orazi et al. (2012); inversed triangles are from De Silva et al. (2013); grey squares are from Reddy & Lambert (2015); black diamond is from Biazzo et al. (2017); blue triangles are from Magrini et al. (2018); brown pentagon is from Frasca et al. (2019); light pink triangle are from Casamiquela et al. (2020); empty circles are from Donor et al. (2020), for which we considered only the measurements for those clusters with reliable membership determination (q_flag=1,2); empty x-crosses are from Spina et al. (2021).

lution of Ba with that of La. In Figure 4.13 the [Ba/La] time-evolution is shown: as expected, the production of both Ba and La in the models is the same, thus neither of them can predict the (apparent) massive Ba production and the observed [Ba/La] rise in the last 100 Myr. As discussed in Mishenina et al. (2015), according to any *s*-process predictions high Ba yields should always be accompanied by high La and Ce yields, due to the presence of the magic number of neutron of 82 in correspondence of these elements (e.g., Busso et al. 2001). This is at odds with what is observed in OCs. Mishenina et al. (2015) proposed that the intermediate neutron-capture (*i*-) process, which proceeds along a different path of neutron captures than the *s*-process, is an additional source of Ba. According to their analysis, a combination of s, r, and *i*- processes may be able to reproduce the [Ba/La]> +0.20 dex observed in OCs for [Eu/La] ranging from −0.4 and +0.4 dex (see Figure 5 and Figure 6 in Mishenina et al. 2015). This hypothesis cannot be confirmed in this analysis in more detail because the Eu cannot be measured in the considered stellar sample: the available Eu lines are too weak to be detected in stars with mild rotations as those in the sample. The *i*-process is an interesting solution, however there are still large uncertainties concerning what stellar sources can host the process, and their efficiency in producing heavy elements. In particular, to explain the Ba excess in the YOCs a site that becomes relevant only in the last 200 Myr would be needed, and that was not yet effective in contributing to the Ba abundance in the solar system. The discovery that the Ba enhancement could be explained by some observational issues (i.e., alteration of the spectral line) would help us solving the Ba puzzle, without affecting the present understanding of the nucleosynthesis of Ba and La in the Galactic disc. From our discussion presented above we cannot make this conclusion either, and therefore the Ba puzzle remain unsolved.

Since the analysis has provided no clear answer for the excess of Ba, we suggest that to trace the *s*-process element abundances at young ages, in particular for ages less than 500 Myr, we should look for other elements and investigate further La and Ce. Theoretical models for Galactic chemical enrichment of heavy elements and theoretical GCE models including the *s*-process only should consider Ba and Y with extreme caution. The anomalous abundances of Y can also have an impact on the use of some chemical clocks, [Y/Mg] for example, as a age indicators for young stars. As different studies demonstrated (see, e.g., Nissen 2015; Spina et al. 2018; Casamiquela et al. 2021 for solar twin stars), the [Y/Mg] ratio traces well the age up to 500-700 Myr. Unfortunately, both studies do not consider ages as young as the clusters I have analysed in this work. My analysis suggests that the effects of alteration of the spectral lines could affect the relation [Y/Mg] *vs.* age, with larger impact below 100 Myr, but probably also between 100-500 Myr. This is particularly evident from the bottom-right panel in Figure 4.13, where it is clear that the adopted GCE models cannot reproduce the increased abundance at young ages. Thus, we suggest that caution should be payed in using Y as tracer of the s-process and as an age indicator below 500 Myr (as [Y/Mg] and all the other ratios based on the Y abundances).

4.5.3 The time evolution of Cu

To follow the evolution of Cu, the GCE models presented by Romano & Matteucci (2007) and Romano et al. (2010, 2019) are considered. We have seen that most of Cu production on Galactic scales is due to the weak s-process acting in massive stars. This mechanism depends on the initial metallicity of the stars. The neutrons originate mainly from the reaction ^{22}Ne(α,n)^{25}Mg; the large abundance of ^{22}Ne during He-burning core derives from the original CNO nuclei transmuted into ^{14}N in the H-burning ashes, followed by double α-capture on ^{14}N. Copper produced in this way is thus a secondary-like element. A small primary yield of Cu, 5 to 10% of its solar abundance derives from explosive nucleosynthesis in the inner regions of core-collapse supernovae (see, e.g., Woosley & Weaver 1995, Rauscher et al. 2002, Pignatari et al. 2010). SN Ia models predict a negligible production of Cu during thermonuclear explosions (e.g. Iwamoto et al. 1999; Travaglio et al. 2005). Low- and intermediate-mass stars produce minor quantities of Cu as well. Thus, the models adopted in this paper assume that almost all Cu comes from massive stars, with a minor contribution from SNe Ia. After a short, early phase in which the primary contribution from explosive nucleosynthesis in core-collapse SNe dominates, the evolution of Cu is regulated by the weak s-process. The models shown in Figure4.13 include massive star yields from (i) Woosley & Weaver (1995) (green curve), (ii) Kobayashi et al. (2006) with (orange curve) or (iii) without (blue curve) the contribution from hypernovae (cfr. models 4 and 5 of Romano et al. 2010), and (iv) the yields from rotating (for $[\mathrm{Fe/H}] < -1$) and non-rotating (for $[\mathrm{Fe/H}] > -1$) core-collapse SN progenitor provided by Limongi & Chieffi (2018) (red line, corresponding to model MWG-11 of Romano et al. 2019 to which we refer the reader for more details). Note that some data in the range $\log t \sim 7.5 - 8$ (from this work and from Spina et al. 2021) fall below the predictions of the GCE models by about 10-60% (corresponding to 0.05-0.2 dex). Considering the uncertainties in the atomic physics affecting the measured abundances from Cu or Mg (or both), all the abundance ratios could be risen by 20-30%. Both Mg and Cu are mostly made in CCSNe, but they are produced through different nucleosynthesis processes. For instance, the present uncertainties in the ^{22}Ne(α,n)^{25}Mg reaction (responsible for the Cu production) could justify a reduction of the [Cu/Mg] curve (see Figure 18 in Talwar et al. 2016). Additional variations of the order of the discrepancy observed could derive from the limitations of the GCE simulations adopted here, which predict average trends and cannot deal with local inhomogeinities that could play a role at this level of variation. Overall, taking into ac-

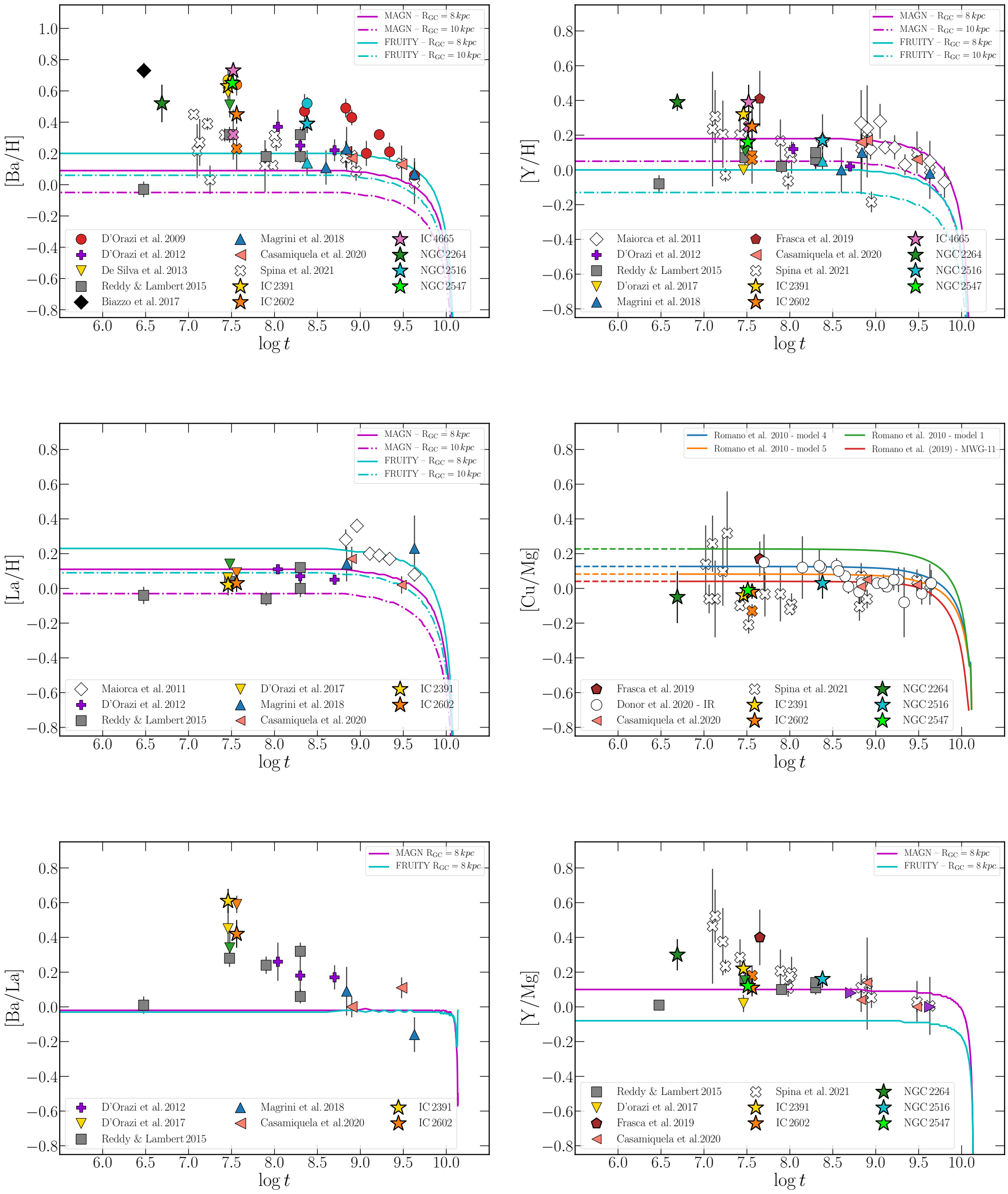

Figure 4.13: [Ba/H] (top-left panel), [Y/H] (top-right panel), [La/H] (central-left panel), [Cu/Mg] (central-right panel), [Ba/La] (bottom-left panel) and [Y/Mg] (bottom-right panel) as a function of the age of Galactic open clusters with $7.5<\mathrm{R_{GC}}<9$ kpc. The cluster symbols are the same as in Figure4.12. The cyan and magenta lines are the GCE models described in Magrini et al. (2021) with the MAGN stellar yields (Vescovi et al. 2020; continuous curves) and FRUITY (Cristallo et al. 2009; dot-dashed curves). In the [Cu/Mg] *vs.* $\log t$ the models from Romano et al. (2010) with different stellar yields are considered: model 1 (green curve) with Woosley & Weaver (1995) yields , model 5 with yields from Kobayashi et al. (2006) with (orange line) or model 4 without (blue line) hypernovae contribution and finally Romano et al. (2019) (red line) with yields from Limongi & Chieffi (2018). See the text for further details .

count the observational uncertainties and the limitations of the models, the red line (model MWG-11 adopting the yields by Limongi & Chieffi 2018) is in fair agreement with the full dataset.

4.6 Concluding remarks

In this Chapter, the behaviour of the neutron-capture elements is investigated, continuing the study started in Baratella et al. (2020b). The main goal was to shed light on the peculiar composition of YOCs. In particular, I derived abundances of Cu i, Sr i and ii, Y ii, Zr ii, Ba ii, La ii and Ce ii. For all the clusters I reported the very first determinations of [Cu/Fe]. Regarding IC 2391 and IC 2602, which are the most studied clusters in our sample, I presented the first determinations of [Sr/Fe]. On the other hand, I presented for the first time heavy-element abundances for NGC 2264 and NGC 2547.

My measurements confirm the super-solar (0.25-0.70 dex) [Ba/Fe] abundances in the youngest population, a mild enhancement of [Y/Fe] (between 0 and 0.30 dex) and a solar-scaled abundance pattern for all the other *s*-process elements. I investigated several aspects in order to envisage possible solutions to the anomalous behaviour of the *s*-process element Ba.

From the comparison of spectral lines in the Sun and a solar analog of $\sim$ 30 Myr, it is evident that the lines of some elements, like Fe ii, Ca i, Ba ii, Y ii are stronger in the young star than in the Sun. On the other hand, La, Sr and relatively weak lines of other elements, like Sc i or Sc ii, are almost identical. Sc lines can form at different depths as the other elements for which I observe a remarkable difference. Looking at the results obtained for the GBS, which are old and quiet stars, I do not reveal any anomalous trend. It is not clear what is altering the structure of the photosphere in very young stars and how this can modify the profiles of the spectral lines. From my analysis, the situation appears rather complex: the magnetic intensification is not sufficient to explain fully the large abundances. Both ionised and neutral lines are altered in the same way, but this alteration may vary with the optical depth, in the sense that lines at smaller $\log \tau_{5000}$ (i.e., in the upper layers) are more affected than lines forming deeper in the photosphere.

The solution proposed by Spina et al. (2020) of magnetic intensification and a pure photospheric, 1D-LTE treatment involving microturbulence seem to be not sufficient to account for the observed pattern, since in this case, we are dealing with much younger stars ($t \lesssim 200$ Myr). Recently, Şenavcı et al. (2021) analysed the young ($\sim$ 30 Myr), active and relatively fast-rotator ($\sim$ 17km s^{-1}) solar-analog EK Draconis. They derived precise atmospheric parameters and chemical abundance and they studied the spots distribution on the stellar surface. They found a significant overabundance of Ba ([Ba/H]=+0.63 dex) and values of [Cu/H], [Sr/H], [Y/H] and [Ce/H] which are solar within the uncertainties. Following Reddy & Lambert (2017), they concluded that the Ba overabundance is likely due to the assumption of depth-independent microturbulence velocity, but my analysis suggests that the explanation may be far more complex.

Overall, the anomalous behaviour of the *s*-process elements, in particular Ba and Y and relatively to La, cannot be reconciled with only nucleosynthesis models and Galactic chemical evolution predictions. NLTE effects can not be similarly invoked, since the corrections are not sufficiently large. Thus, I suggest that Ba should not be used as a tracer of the *s*-process elements for young stars, along with Y. Instead, we promote the use of La or Ce, as the most reliable tracer for the investigation of time evolution of the *s*-process elements (especially at recent Galactic ages). Possible solutions of the Ba puzzle, both from the spectra and the nucleosynthesis prospective, are still under investigation. Masseron et al. (2020b) reported anomalous Ba enhancements (10 times higher than the other *s*-process elements) in stars that are also anomalous in the lighter elements, specifically rich in P (Masseron et al. 2020a). As discussed above, this pattern cannot be reproduced by any *s*-process model because of the nuclear properties of the isotopes involved. On the one hand, it remains to be seen if the Ba anomaly in these P-rich stars has any connection with the Ba anomaly in YOCs: while the P-rich stars have [Fe/H] roughly -1, and therefore they are not young, their overall puzzling nucleosynthetic pattern may represent a clue to the site of the *i*-process.

Finally, we note that Zr lines might provide us with reliable diagnostics for the first-peak elements, because its lines form deeper in the photosphere than the two Y lines we have used here. However, we should also increase the number of spectroscopic observations of very young objects in the 3000-5000 Å, where the best La, Zr and Ce lines are. Next-coming multi-object, high-resolution spectrographs in the blue wavelength domain will give fundamental contribution in this framework.

CHAPTER 5

Conclusions

In this Thesis fundamental issues related to the spectroscopic analysis of young stars (with ages less than the Hyades, ∼ 600 Myr) have been investigated. Our working hypothesis stems from previous works (Flores et al. 2016; Reddy & Lambert 2017; Yana Galarza et al. 2019; Spina et al. 2020) that suggested the possible link between chemical anomalies and stellar activity. The activity of young stars is strong enough to alter the line formation and/or the structure of the atmosphere itself.

In my investigation I confirmed (observationally) this hypothesis: essentially, the three main problems of young stellar systems (the local anaemia, the overabundance of ionised atoms, and the Ba puzzle) *are* due to limitation of the standard abundance analysis. However, what is the main mechanism causing such limitations (is it the photospheric magnetic field? are the dark spots? are the bright spots?) remains unknown. While waiting for further studies to explore this, we must find other ways to overcome these issues to obtain more reliable stellar parameters and chemical abundances.

High-resolution, high S/N UVES at ESO and HARPS-N + Giano-B at the TNG spectra of stars belonging to a variety of young clusters (IC 2391, IC 2601, IC 4665, NGC 2516, NGC 2547), star forming region (NGC 2264) and moving groups (Ursa Major, Hercules-Lyrae, Coma Berenices) have been analysed.

The results are presented and discussed in each Chapter, here I briefly summarize the main conclusions:

- *Is the metal-poor nature of nearby YOCs and SFRs intrinsic or related to analysis techniques? What are the implications for the search of Jupiter-like planets in these systems, in light of the giant planet-metallicity relation?*

  To answer these questions, I have analysed in Chapter 2 a sample of 23 dwarf stars in five YOCs and one SFR included in the *Gaia*-ESO Survey. My investigation showed that the strong Fe lines, which typically form in the upper layers of the photosphere, are systematically deeper in a young solar-analog (in IC 2602) than in the old Sun (confirming what has been found by Reddy & Lambert 2017). An EW analysis that uses Fe I lines returns a value of ξ parameter that is too large with respect to the expected values for a dwarf star. This translates into a poor fit of the observed line with synthetic profiles and an under-estimation of the chemical abundances ([Fe/H] and all the [X/Fe] ratios that rescale accordingly). To overcome this, I developed a new spectroscopic approach that consists of a combination of Fe and Ti lines to derive $T_{\rm eff}$, while using Ti lines *only* to derive $\log g$ and ξ. We chose Ti lines because they have very precise atomic data from laboratory measurements (Lawler et al. 2013) and because (on average) they form deeper in the photosphere than Fe lines. Thus, they are less sensitive to the increased level of chromospheric activity and magnetic fields. The comparison with *Gaia*-ESO iDR5 results (i.e., obtained with the standard analysis) shows that while $T_{\rm eff}$ and $\log g$ have comparable measurements, the most dramatic effect is seen for ξ parameter, with the over-estimation being larger below 100 Myr (see for example the third panel of the first row in Figure 2.6). Moreover, it is evident also the correlation of the ξ values from standard analysis with stellar activity, which is instead missing for the new ξ. In the Galactic evolution framework, the new estimates of [Fe/H] agree well with the predictions of the GCE model (e.g., by Minchev et al. 2013), without invoking peculiar and complex chemical evolution scenarios. This new method has become the main strategy to analyse young stars observed by the GAPS-YO group, in particular by the stellar characterisation team. The results of a first sample of stars is presented in Chapter 3, where the connection between the anomalous over-abundances and the stellar activity has been explored.

- *What is the reason for the overabundance of ionised atoms?*

  Beyond the issues related to the overestimation of ξ and consequent lower [Fe/H], young and cool ($T_{\rm eff} < 5400$ K) stars present anomalous over-abundance of ionised atoms and high-excitation potential lines. This topic is discussed extensively in Chapter 3, where a sample of seven young targets, and two RV standard stars have been analysed. In particular, I derived abundances of different atomic species, including Cr II and C (from atomic lines with $\chi > 7.5$ eV found in the optical spectral range). For Cr, I found that it reaches a value of +0.15 dex at $T_{\rm eff}$ around ≈ 4800 K: this is explained as a manifestation of the overionisation problem (Schuler et al. 2010). It is clear that chemical peculiarities at these young ages are related to stellar activity, since the Cr II abundances show a positive correlation with the $\log R'_{\rm HK}$. Similar behaviour is also found for C abundances in optical: dramatic increase of abundance at decreasing $T_{\rm eff}$ (the effect is more evident than Cr) and positive correlation with increasing log R'_{HK}. The trend with T_{eff} has been also confirmed recently in Delgado Mena et al. (2021) for a sample of 1111 FGK stars. Because C (and the C/O ratio) is extremely important especially to study exoplanetary systems and their formation mechanisms, we must use a different indicator, rather than atomic C lines. My analysis suggests that CH molecular bands are good diagnostics to infer C abundances, as no correlation with T_{eff} and log R'_{HK} have been found. This results are presented in Maldonado et al. (2020), where I derived C abundance from CH band at 4300 Å for a sample of 19 FGK stars.

- *How can we explain the observed overabundance of Ba? Do the other s-process elements behave like Ba?*

  To continue the study started in the previous Chapters, I have investigated the behaviour of different neutron-capture elements (Cu I, Sr I and II, Y II, Zr II, Ba II, La II and Ce II) in the same stars analysed in Chapter 2. My measurements confirm the over-solar [Ba/Fe] (between 0.25 and 0.65 dex), but display also a mild enhancement of [Y/Fe] (between 0 and 0.30 dex), while solar-scaled abundances for the other elements. While the mild enrichment of [Y/Fe] could be explained with the adopted ξ values, the situation with Ba is more complex. I investigated different solutions, both from a spectral and a nucleosynthesis point of view. In the first case, from the comparison between the spectra of the Sun and the young solar analog, it is clear that Ba and Y lines are stronger in the young stars, while the lines of the other elements (typically weaker than Ba and Y) are almost identical. This has been confirmed by comparing the lines of other elements (Fe, Ca and Sc, neutral and ionised). For the GSB stars, I do not reveal any anomalous trend. Indeed, the Ba and Y abundances show a positive correlation with the log R'_{HK}. Therefore, from a spectral point of view, the optical depth of line formation and overionisation alone cannot explain the behaviour of *s*-elements. On the other hand, the nucleosynthesis models cannot predict the Ba production completely disentangled from La, as these elements are produced through the same reaction channel (they belong to the second peak of the s process elements). This is also reflected by the inability of the GCE models to reproduce the Galactic time evolution of these elements. A possible solution could be the activation of the *i*-process, but more studies are needed to confirm this. In general, the main conclusion of our investigation is that Ba and Y cannot be used as tracers of the *s*-process elemebts at you ages. Conversely, we promote the use of La and Ce for the second peak and Zr for the first peak, while possible solutions to the issue are still under investigation.

The general conclusion of my thesis is that the spectroscopic analysis of young stars is not straightforward and a standard analysis cannot be safely applied to study the young stars. We can overcome all the analytical issues by adopting new strategies (i.e., the Ti approach) or we could refine the master line list (i.e., selecting the lines by taking only those weaker than some value of EW). This is particularly important in the large spectroscopic surveys framework, where stars of different ages are routinely analysed in the same way. At the same time, we must extensively investigate the effects of stellar activity on spectral line formation and finally pinpoint the main mechanism. In this sense, we are analysing a number of simulated spectra of the Sun in which surface magnetic fields, and dark/bright spot coverage have been varied. This work is in progress and results will be published in a forthcoming paper.

Bibliography

Adibekyan, V. 2019, Geosciences, 9, 105

Aleo, P. D., Sobotka, A. C., & Ramírez, I. 2017, ApJ, 846, 24

Alibert, Y., Mordasini, C., & Benz, W. 2004, A&A, 417, L25

Amarsi, A. M., Nissen, P. E., & Skúladóttir, Á. 2019, A&A, 630, A104

Ammler-von Eiff, M. & Guenther, E. W. 2009, A&A, 508, 677

Arcones, A. & Montes, F. 2011, ApJ, 731, 5

Asplund, M., Grevesse, N., Sauval, A. J., & Scott, P. 2009, ARA&A, 47, 481

Bailer-Jones, C. A. L., Rybizki, J., Fouesneau, M., Mantelet, G., & Andrae, R. 2018, AJ, 156, 58

Bailey, J. I., Mateo, M., White, R. J., Shectman, S. A., & Crane, J. D. 2018, MNRAS, 475, 1609

Banerjee, P., Qian, Y.-Z., & Heger, A. 2018, ApJ, 865, 120

Baratella, M., Carraro, G., D'Orazi, V., & Semenko, E. A. 2018, AJ, 156, 244

Baratella, M., D'Orazi, V., Biazzo, K., et al. 2020a, A&A, 640, A123

Baratella, M., D'Orazi, V., Carraro, G., et al. 2020b, A&A, 634, A34

Baratella, M., D'Orazi, V., Sheminova, V., et al. 2021, A&A, 653, A67

Barklem, P. S., Piskunov, N., & O'Mara, B. J. 2000, A&AS, 142, 467

Barrado y Navascués, D., Stauffer, J. R., & Jayawardhana, R. 2004, ApJ, 614, 386

Barrado y Navascués, D., Stauffer, J. R., & Patten, B. M. 1999, ApJ, 522, L53

Bensby, T., Feltzing, S., & Oey, M. S. 2014, A&A, 562, A71

Bergemann, M. 2011, MNRAS, 413, 2184

Bergemann, M., Hansen, C. J., Bautista, M., & Ruchti, G. 2012, A&A, 546, A90

Bertolli, M. G., Herwig, F., Pignatari, M., & Kawano, T. 2013, arXiv e-prints, arXiv:1310.4578

Biazzo, K., D'Orazi, V., Desidera, S., et al. 2012, MNRAS, 427, 2905

Biazzo, K., Frasca, A., Alcalá, J. M., et al. 2017, A&A, 605, A66

Biazzo, K., Randich, S., & Palla, F. 2011a, A&A, 525, A35

Biazzo, K., Randich, S., Palla, F., & Briceño, C. 2011b, A&A, 530, A19

Bisterzo, S., Pompeia, L., Gallino, R., et al. 2005, Nucl. Phys. A, 758, 284

Bisterzo, S., Travaglio, C., Gallino, R., Wiescher, M., & Käppeler, F. 2014, ApJ, 787, 10

Blanco-Cuaresma, S., Soubiran, C., Heiter, U., et al. 2015, A&A, 577, A47

Blanco-Cuaresma, S., Soubiran, C., Heiter, U., & Jofré, P. 2014a, A&A, 569, A111

Blanco-Cuaresma, S., Soubiran, C., Jofré, P., & Heiter, U. 2014b, A&A, 566, A98

Bossini, D., Vallenari, A., Bragaglia, A., et al. 2019, A&A, 623, A108

Bovy, J. 2016, ApJ, 817, 49

Brewer, J. M., Fischer, D. A., & Madhusudhan, N. 2017, AJ, 153, 83

Brewer, J. M., Fischer, D. A., Valenti, J. A., & Piskunov, N. 2016, ApJS, 225, 32

Buder, S., Sharma, S., Kos, J., et al. 2020, arXiv e-prints, arXiv:2011.02505

Burbidge, E. M., Burbidge, G. R., Fowler, W. A., & Hoyle, F. 1957, Reviews of Modern Physics, 29, 547

Burkhart, C. & Coupry, M. F. 2000, A&A, 354, 216

Busso, M., Gallino, R., Lambert, D. L., Travaglio, C., & Smith, V. V. 2001, ApJ, 557, 802

Caffau, E., Bonifacio, P., Oliva, E., et al. 2019, A&A, 622, A68

Cantat-Gaudin, T., Anders, F., Castro-Ginard, A., et al. 2020, A&A, 640, A1

Cantat-Gaudin, T., Jordi, C., Vallenari, A., et al. 2018, A&A, 618, A93

Cargile, P. A. & James, D. J. 2010, AJ, 140, 677

Carleo, I., Malavolta, L., Lanza, A. F., et al. 2020, arXiv e-prints, arXiv:2002.10562

Carleo, I., Sanna, N., Gratton, R., et al. 2016, Experimental Astronomy, 41, 351

Carraro, G., Semenko, E. A., & Villanova, S. 2016, AJ, 152, 224

Carrera, R. & Pancino, E. 2011, A&A, 535, A30

Casagrande, L., Ramírez, I., Meléndez, J., Bessell, M., & Asplund, M. 2010, A&A, 512, A54

Casali, G., Magrini, L., Frasca, A., et al. 2020a, A&A, 643, A12

Casali, G., Spina, L., Magrini, L., et al. 2020b, A&A, 639, A127

Casamiquela, L., Blanco-Cuaresma, S., Carrera, R., et al. 2019, MNRAS, 490, 1821

Casamiquela, L., Carrera, R., Jordi, C., et al. 2016, MNRAS, 458, 3150

Casamiquela, L., Soubiran, C., Jofré, P., et al. 2021, arXiv e-prints, arXiv:2103.14692

Casamiquela, L., Tarricq, Y., Soubiran, C., et al. 2020, A&A, 635, A8

Castelli, F. & Kurucz, R. L. 2003, in IAU Symposium, Vol. 210, Modelling of Stellar Atmospheres, ed. N. Piskunov, W. W. Weiss, & D. F. Gray, A20

Cescutti, G. & Chiappini, C. 2014, A&A, 565, A51

Chen, Y. Q., Zhao, G., Izumiura, H., et al. 2008, AJ, 135, 618

Choplin, A., Siess, L., & Goriely, S. 2021, arXiv e-prints, arXiv:2102.08840

Claret, A. 2019, Research Notes of the American Astronomical Society, 3, 17

Clarkson, O., Herwig, F., & Pignatari, M. 2018, MNRAS, 474, L37

Claudi, R., Benatti, S., Carleo, I., et al. 2017, European Physical Journal Plus, 132, 364

Cosentino, R., Lovis, C., Pepe, F., et al. 2014, Society of Photo-Optical Instrumentation Engineers (SPIE) Conference Series, Vol. 9147, HARPS-N @ TNG, two year harvesting data: performances and results, 91478C

Côté, B., Denissenkov, P., Herwig, F., et al. 2018, ApJ, 854, 105

Covino, E., Esposito, M., Barbieri, M., et al. 2013, A&A, 554, A28

Cowan, J. J. & Rose, W. K. 1977, ApJ, 212, 149

Cowan, J. J., Sneden, C., Lawler, J. E., et al. 2021, Reviews of Modern Physics, 93, 015002

Cristallo, S., Karinkuzhi, D., Goswami, A., Piersanti, L., & Gobrecht, D. 2016, ApJ, 833, 181

Cristallo, S., Straniero, O., Gallino, R., et al. 2009, ApJ, 696, 797

Şenavcı, H. V., Kılıçoğlu, T., Işık, E., et al. 2021, arXiv e-prints, arXiv:2101.07248

Cunha, K., Frinchaboy, P. M., Souto, D., et al. 2016, Astronomische Nachrichten, 337, 922

Cutri, R. M., Skrutskie, M. F., van Dyk, S., et al. 2003, 2MASS All Sky Catalog of point sources.

Davenport, J. R. A., Covey, K. R., Clarke, R. W., et al. 2019, ApJ, 871, 241

De Silva, G. M., D'Orazi, V., Melo, C., et al. 2013, MNRAS, 431, 1005

De Silva, G. M., Freeman, K. C., Bland-Hawthorn, J., et al. 2015, MNRAS, 449, 2604

Delgado Mena, E., Adibekyan, V., Santos, N. C., et al. 2021, arXiv e-prints, arXiv:2109.04844

Denissenkov, P. A., Herwig, F., Battino, U., et al. 2017, ApJ, 834, L10

Denissenkov, P. A., Herwig, F., Perdikakis, G., & Schatz, H. 2021, MNRAS, 503, 3913

Denissenkov, P. A., Herwig, F., Woodward, P., et al. 2019, MNRAS, 488, 4258

Donor, J., Frinchaboy, P. M., Cunha, K., et al. 2020, AJ, 159, 199

D'Orazi, V., Biazzo, K., Desidera, S., et al. 2012, MNRAS, 423, 2789

D'Orazi, V., Biazzo, K., & Randich, S. 2011, A&A, 526, A103

D'Orazi, V., Desidera, S., Gratton, R. G., et al. 2017, A&A, 598, A19

D'Orazi, V., Magrini, L., Randich, S., et al. 2009a, ApJ, 693, L31

D'Orazi, V., Oliva, E., Bragaglia, A., et al. 2020, A&A, 633, A38

D'Orazi, V., Randich, S., Flaccomio, E., et al. 2009b, A&A, 501, 973

Dutra-Ferreira, L., Pasquini, L., Smiljanic, R., Porto de Mello, G. F., & Steffen, M. 2016, A&A, 585, A75

Eisenbeiss, T., Ammler-von Eiff, M., Roell, T., et al. 2013, A&A, 556, A53

Fabbian, D., Khomenko, E., Moreno-Insertis, F., & Nordlund, Å. 2010, ApJ, 724, 1536

Farouqi, K., Kratz, K. L., Mashonkina, L. I., et al. 2009, ApJ, 694, L49

Fenner, Y., Gibson, B. K., Lee, H. c., et al. 2003, PASA, 20, 340

Fischer, D. A. & Valenti, J. 2005, ApJ, 622, 1102

Flores, M., González, J. F., Jaque Arancibia, M., Buccino, A., & Saffe, C. 2016, A&A, 589, A135

Folsom, C. P., Petit, P., Bouvier, J., et al. 2016, MNRAS, 457, 580

Frasca, A., Alonso-Santiago, J., Catanzaro, G., et al. 2019, A&A, 632, A16

Frasca, A., Biazzo, K., Lanzafame, A. C., et al. 2015, A&A, 575, A4

Friel, E. D. 1995, ARA&A, 33, 381

Friel, E. D. & Boesgaard, A. M. 1992, ApJ, 387, 170

Froese Fischer, C. & Tachiev, G. 2012, Multiconfiguration Hartree-Fock and Multiconfiguration Dirac-Hartree-Fock Collection, Version 2, available online at http://physics.nist.gov/mchf/

Gadun, A. S. & Sheminova, V. A. 1988, Preprint of the Institute for Theoretical Physics of Academy of Sciences of USSR, 87, 3

Gallagher, A. J., Bergemann, M., Collet, R., et al. 2020, A&A, 634, A55

Gallino, R., Arlandini, C., Busso, M., et al. 1998, ApJ, 497, 388

Gebran, M., Monier, R., & Richard, O. 2008, A&A, 479, 189

Ghezzi, L., Cunha, K., Smith, V. V., et al. 2010, ApJ, 720, 1290

Gilmore, G., Randich, S., Asplund, M., et al. 2012, The Messenger, 147, 25

Gonzalez, G., Carlson, M. K., & Tobin, R. W. 2010, MNRAS, 403, 1368

Gratton, R., Bragaglia, A., Carretta, E., et al. 2019, A&A Rev., 27, 8

Gray, D. F. 1992, The observation and analysis of stellar photospheres., Vol. 20

Gray, D. F. 2005, The Observation and Analysis of Stellar Photospheres

Grevesse, N., Scott, P., Asplund, M., & Sauval, A. J. 2015, A&A, 573, A27

Gurtovenko, E., Ratnikova, V., & de Jager, C. 1974, Sol. Phys., 37, 43

Gurtovenko, E. A. & Sheminova, V. A. 2015, arXiv e-prints, arXiv:1505.00975

Gustafsson, B., Edvardsson, B., Eriksson, K., et al. 2008, A&A, 486, 951

Hannaford, P., Lowe, R. M., Grevesse, N., Biemont, E., & Whaling, W. 1982, ApJ, 261, 736

Harutyunyan, A., Rainer, M., Hernandez, N., et al. 2018, in Society of Photo-Optical Instrumentation Engineers (SPIE) Conference Series, Vol. 10706, Proc. SPIE, 1070642

Heil, M., Käppeler, F., Uberseder, E., Gallino, R., & Pignatari, M. 2008, Phys. Rev. C, 77, 015808

Heiter, U., Lind, K., Bergemann, M., et al. 2020, arXiv e-prints, arXiv:2011.02049

Heiter, U., Lind, K., Bergemann, M., et al. 2019, A&A, submitted

Heiter, U., Soubiran, C., Netopil, M., & Paunzen, E. 2014, A&A, 561, A93

Helled, R., Bodenheimer, P., Podolak, M., et al. 2014, in Protostars and Planets VI, ed. H. Beuther, R. S. Klessen, C. P. Dullemond, & T. Henning, 643

Herwig, F., Pignatari, M., Woodward, P. R., et al. 2011, ApJ, 727, 89

Hunter, A. A., Macgregor, A. B., Szabo, T. O., Wellington, C. A., & Bellgard, M. I. 2012, Source code for biology and medicine, 7, 1

Iwamoto, K., Brachwitz, F., Nomoto, K., et al. 1999, ApJS, 125, 439

Jacobson, H. R. & Friel, E. D. 2013, AJ, 145, 107

Jacobson, H. R., Friel, E. D., Jílková, L., et al. 2016, A&A, 591, A37

James, D. J., Melo, C., Santos, N. C., & Bouvier, J. 2006, A&A, 446, 971

Jofré, E., Petrucci, R., Saffe, C., et al. 2015a, A&A, 574, A50

Jofré, P., Heiter, U., & Soubiran, C. 2019, ARA&A, 57, 571

Jofré, P., Heiter, U., Soubiran, C., et al. 2015b, A&A, 582, A81

Jofré, P., Heiter, U., Soubiran, C., et al. 2015c, A&A, 582, A81

Jofré, P., Heiter, U., Tucci Maia, M., et al. 2018, Research Notes of the American Astronomical Society, 2, 152

Jofré, P., Heiter, U., Worley, C. C., et al. 2017, A&A, 601, A38

Jones, S., Côté, B., Röpke, F. K., & Wanajo, S. 2019, ApJ, 882, 170

Jones, S., Ritter, C., Herwig, F., et al. 2016, MNRAS, 455, 3848

Käppeler, F., Gallino, R., Bisterzo, S., & Aoki, W. 2011, Reviews of Modern Physics, 83, 157

Karakas, A. I. & Lattanzio, J. C. 2014, PASA, 31, e030

Kaufer, A., Stahl, O., Tubbesing, S., et al. 1999, The Messenger, 95, 8

King, J. R. & Schuler, S. C. 2005, PASP, 117, 911

King, J. R., Soderblom, D. R., Fischer, D., & Jones, B. F. 2000, ApJ, 533, 944

Kobayashi, C., Karakas, A. I., & Lugaro, M. 2020, ApJ, 900, 179

Kobayashi, C., Umeda, H., Nomoto, K., Tominaga, N., & Ohkubo, T. 2006, ApJ, 653, 1145

Korotin, S. A., Andrievsky, S. M., Hansen, C. J., et al. 2015, A&A, 581, A70

Kurucz, R. L. 2011, Canadian Journal of Physics, 89, 417

Laming, J. M. 2015, Living Reviews in Solar Physics, 12, 2

Landi Degl'Innocenti, E. 1982, Sol. Phys., 79, 291

Lanzafame, A. C., Frasca, A., Damiani, F., et al. 2015, A&A, 576, A80

Lawler, J. E., Bonvallet, G., & Sneden, C. 2001, Astrophys. J., 556, 452, (LBS)

Lawler, J. E., Guzman, A., Wood, M. P., Sneden, C., & Cowan, J. J. 2013, ApJS, 205, 11

Lawler, J. E., Sneden, C., Cowan, J. J., Ivans, I. I., & Den Hartog, E. A. 2009, Astrophys. J. Suppl. Ser., 182, 51, (LSCI)

Lawler, J. E., Sneden, C., Nave, G., et al. 2017, ApJS, 228, 10

Limongi, M. & Chieffi, A. 2018, ApJS, 237, 13

Lind, K., Asplund, M., Barklem, P. S., & Belyaev, A. K. 2011, A&A, 528, A103

Lindegren, L., Hernández, J., Bombrun, A., et al. 2018, A&A, 616, A2

Linsky, J. L., Bushinsky, R., Ayres, T., Fontenla, J., & France, K. 2012, ApJ, 745, 25

Ljung, G., Nilsson, H., Asplund, M., & Johansson, S. 2006, A&A, 456, 1181

Lodders, K. 2003, ApJ, 591, 1220

Lodders, K. 2019, arXiv e-prints, arXiv:1912.00844

Lodders, K., Palme, H., & Gail, H. P. 2009, Landolt Börnstein, 4B, 712

López-Santiago, J., Montes, D., Crespo-Chacón, I., & Fernández-Figueroa, M. J. 2006, ApJ, 643, 1160

Lorenzo-Oliveira, D., Freitas, F. C., Meléndez, J., et al. 2018, A&A, 619, A73

Lovis, C., Dumusque, X., Santos, N. C., et al. 2011, arXiv e-prints, arXiv:1107.5325

Luck, R. E. 2017, AJ, 153, 21

Luck, R. E. 2018, AJ, 155, 111

Lugaro, M., Campbell, S. W., Van Winckel, H., et al. 2015, A&A, 583, A77

Lugaro, M., Karakas, A. I., Stancliffe, R. J., & Rijs, C. 2012, ApJ, 747, 2

Magrini, L., Randich, S., Kordopatis, G., et al. 2017, A&A, 603, A2

Magrini, L., Sestito, P., Randich, S., & Galli, D. 2009, A&A, 494, 95

Magrini, L., Spina, L., Randich, S., et al. 2018, A&A, 617, A106

Magrini, L., Vescovi, D., Casali, G., et al. 2021, arXiv e-prints, arXiv:2101.04429

Maiorca, E., Magrini, L., Busso, M., et al. 2012, ApJ, 747, 53

Maiorca, E., Randich, S., Busso, M., Magrini, L., & Palmerini, S. 2011, ApJ, 736, 120

Malavolta, L., Nascimbeni, V., Piotto, G., et al. 2016, A&A, 588, A118

Maldonado, J., Eiroa, C., Villaver, E., Montesinos, B., & Mora, A. 2015, A&A, 579, A20

Maldonado, J., Micela, G., Baratella, M., et al. 2020, A&A, 644, A68

Mamajek, E. E. & Hillenbrand, L. A. 2008, ApJ, 687, 1264

Marfil, E., Tabernero, H. M., Montes, D., et al. 2020, MNRAS, 492, 5470

Marigo, P., Girardi, L., Bressan, A., et al. 2017, ApJ, 835, 77

Marsden, S. C., Petit, P., Jeffers, S. V., et al. 2014, MNRAS, 444, 3517

Martínez-Arnáiz, R., Maldonado, J., Montes, D., Eiroa, C., & Montesinos, B. 2010, A&A, 520, A79

Masana, E., Jordi, C., & Ribas, I. 2006, A&A, 450, 735

Masseron, T., García-Hernández, D. A., Santoveña, R., et al. 2020a, Nature Communications, 11, 3759

Masseron, T., García-Hernández, D. A., Zamora, O., & Manchado, A. 2020b, ApJ, 904, L1

Matteucci, F., Raiteri, C. M., Busson, M., Gallino, R., & Gratton, R. 1993, A&A, 272, 421

Mayor, M., Pepe, F., Queloz, D., et al. 2003, The Messenger, 114, 20

McWilliam, A. 1998, AJ, 115, 1640

Meléndez, J. 2004, ApJ, 615, 1042

Meléndez, J., Asplund, M., Gustafsson, B., & Yong, D. 2009, ApJ, 704, L66

Meléndez, J., Ramírez, I., Karakas, A. a. I., et al. 2014, ApJ, 791, 14

Mermilliod, J. C., Grenon, M., & Mayor, M. 2008, A&A, 491, 951

Mermilliod, J. C., Mayor, M., & Udry, S. 2009, A&A, 498, 949

Minchev, I., Chiappini, C., & Martig, M. 2013, A&A, 558, A9

Mishenina, T., Korotin, S., Carraro, G., Kovtyukh, V. V., & Yegorova, I. A. 2013, MNRAS, 433, 1436

Mishenina, T., Pignatari, M., Carraro, G., et al. 2015, MNRAS, 446, 3651

Modigliani, A., Mulas, G., Porceddu, I., et al. 2004, The Messenger, 118, 8

Monier, R. 2005, A&A, 442, 563

Montes, D., López-Santiago, J., Gálvez, M. C., et al. 2001, MNRAS, 328, 45

Nayakshin, S. 2017, PASA, 34, e002

Naylor, T. & Jeffries, R. D. 2006, MNRAS, 373, 1251

Netopil, M., Paunzen, E., Heiter, U., & Soubiran, C. 2016, A&A, 585, A150

Nissen, P. E. 2015, A&A, 579, A52

Noyes, R. W., Hartmann, L. W., Baliunas, S. L., Duncan, D. K., & Vaughan, A. H. 1984, ApJ, 279, 763

Oliva, E., Origlia, L., Baffa, C., et al. 2006, in Society of Photo-Optical Instrumentation Engineers (SPIE) Conference Series, Vol. 6269, Proc. SPIE, 626919

Origlia, L., Dalessandro, E., Sanna, N., et al. 2019, A&A, 629, A117

Osorio, Y., Barklem, P. S., Lind, K., et al. 2015, A&A, 579, A53

Pasquini, L., Avila, G., Blecha, A., et al. 2002a, The Messenger, 110, 1

Pasquini, L., Avila, G., Blecha, A., et al. 2002b, The Messenger, 110, 1

Pignatari, M., Gallino, R., Heil, M., et al. 2010, ApJ, 710, 1557

Pollack, J. B., Hubickyj, O., Bodenheimer, P., et al. 1996, Icarus, 124, 62

Poretti, E., Boccato, C., Claudi, R., et al. 2016, Mem. Soc. Astron. Italiana, 87, 141

Rainer, M., Harutyunyan, A., Carleo, I., et al. 2018, in Society of Photo-Optical Instrumentation Engineers (SPIE) Conference Series, Vol. 10702, Proc. SPIE, 1070266

Ramírez, I., Allende Prieto, C., & Lambert, D. L. 2007, Astronomy and Astrophysics, 465, 271

Ramírez, I., Allende Prieto, C., & Lambert, D. L. 2013, ApJ, 764, 78

Randich, S., Gilmore, G., & Gaia-ESO Consortium. 2013, The Messenger, 154, 47

Rauscher, T., Heger, A., Hoffman, R. D., & Woosley, S. E. 2002, ApJ, 576, 323

Reddy, A. B. S. & Lambert, D. L. 2015, MNRAS, 454, 1976

Reddy, A. B. S. & Lambert, D. L. 2017, ApJ, 845, 151

Reddy, A. B. S. & Lambert, D. L. 2019, MNRAS, 485, 3623

Reddy, A. B. S., Lambert, D. L., & Giridhar, S. 2016, MNRAS, 463, 4366

Reid, N., Hawley, S. L., & Mateo, M. 1995, MNRAS, 272, 828

Reiners, A., Shulyak, D., Anglada-Escudé, G., et al. 2013, A&A, 552, A103

Roberts, L. F., Woosley, S. E., & Hoffman, R. D. 2010, ApJ, 722, 954

Roederer, I. U., Karakas, A. I., Pignatari, M., & Herwig, F. 2016, ApJ, 821, 37

Romano, D., Karakas, A. I., Tosi, M., & Matteucci, F. 2010, A&A, 522, A32

Romano, D. & Matteucci, F. 2007, MNRAS, 378, L59

Romano, D., Matteucci, F., Zhang, Z.-Y., Ivison, R. J., & Ventura, P. 2019, MNRAS, 490, 2838

Rosén, L., Kochukhov, O., Hackman, T., & Lehtinen, J. 2016, A&A, 593, A35

Sacco, G. G., Morbidelli, L., Franciosini, E., et al. 2014, A&A, 565, A113

Santos, N. C., Israelian, G., & Mayor, M. 2004, A&A, 415, 1153

Santos, N. C., Melo, C., James, D. J., et al. 2008, A&A, 480, 889

Schuler, S. C., Hatzes, A. P., King, J. R., Kürster, M., & The, L.-S. 2006, AJ, 131, 1057

Schuler, S. C., King, J. R., Fischer, D. A., Soderblom, D. R., & Jones, B. F. 2003, AJ, 125, 2085

Schuler, S. C., King, J. R., Hobbs, L. M., & Pinsonneault, M. H. 2004, ApJ, 602, L117

Schuler, S. C., Plunkett, A. L., King, J. R., & Pinsonneault, M. H. 2010, PASP, 122, 766

Schuler, S. C., Vaz, Z. A., Katime Santrich, O. J., et al. 2015, ApJ, 815, 5

Scott, P., Asplund, M., Grevesse, N., Bergemann, M., & Sauval, A. J. 2015, A&A, 573, A26

Shchukina, N., Sukhorukov, A., & Trujillo Bueno, J. 2016, A&A, 586, A145

Shchukina, N. & Trujillo Bueno, J. 2015, A&A, 579, A112

Shchukina, N. G., Sukhorukov, A. V., & Trujillo Bueno, J. 2015, in IAU Symposium, Vol. 305, Polarimetry, ed. K. N. Nagendra, S. Bagnulo, R. Centeno, & M. Jesús Martínez González, 368–371

Sheminova, V. A. 2019, Kinematics and Physics of Celestial Bodies, 35, 129

Sheminova, V. A. & Solanki, S. K. 1999, A&A, 351, 701

Shen, Z. X., Jones, B., Lin, D. N. C., Liu, X. W., & Li, S. L. 2005, ApJ, 635, 608

Shetrone, M., Bizyaev, D., Lawler, J. E., et al. 2015, ApJS, 221, 24

Shi, J. R., Gehren, T., Zeng, J. L., Mashonkina, L., & Zhao, G. 2014, ApJ, 782, 80

Shkolnik, E. L. & Barman, T. S. 2014, AJ, 148, 64

Silaj, J. & Landstreet, J. D. 2014, A&A, 566, A132

Skumanich, A. 1972, ApJ, 171, 565

Smiljanic, R., Korn, A. J., Bergemann, M., et al. 2014, A&A, 570, A122

Sneden, C., Cowan, J. J., & Gallino, R. 2008, ARA&A, 46, 241

Sneden, C. & Lambert, D. L. 1982, ApJ, 259, 381

Sneden, C., Lucatello, S., Ram, R. S., Brooke, J. S. A., & Bernath, P. 2014, ApJS, 214, 26

Sneden, C. A. 1973, PhD thesis, THE UNIVERSITY OF TEXAS AT AUSTIN.

Sobeck, J. S., Kraft, R. P., Sneden, C., et al. 2011, AJ, 141, 175

Soderblom, D. R. & Mayor, M. 1993, AJ, 105, 226

Sousa, S. G., Santos, N. C., Adibekyan, V., Delgado-Mena, E., & Israelian, G. 2015, A&A, 577, A67

Souto, D., Cunha, K., Smith, V. V., et al. 2018, ApJ, 857, 14

Sozzetti, A., Torres, G., Charbonneau, D., et al. 2007, ApJ, 664, 1190

Spina, L., Meléndez, J., Karakas, A. I., et al. 2018, MNRAS, 474, 2580

Spina, L., Nordlander, T., Casey, A. R., et al. 2020, ApJ, 895, 52

Spina, L., Randich, S., Magrini, L., et al. 2017, A&A, 601, A70

Spina, L., Randich, S., Palla, F., et al. 2014a, A&A, 568, A2

Spina, L., Randich, S., Palla, F., et al. 2014b, A&A, 567, A55

Spina, L., Ting, Y. S., De Silva, G. M., et al. 2021, MNRAS, 503, 3279

Steffen, M., Caffau, E., & Ludwig, H. G. 2013, Memorie della Societa Astronomica Italiana Supplementi, 24, 37

Sukhbold, T., Ertl, T., Woosley, S. E., Brown, J. M., & Janka, H. T. 2016, ApJ, 821, 38

Sung, H., Bessell, M. S., & Chun, M.-Y. 2004, AJ, 128, 1684

Tabernero, H. M., Marfil, E., Montes, D., & González Hernández, J. I. 2019, A&A, 628, A131

Tabernero, H. M., Montes, D., González Hernández, J. I., & Ammler-von Eiff, M. 2017, A&A, 597, A33

Takeda, Y. & Honda, S. 2020, AJ, 159, 174

Talwar, R., Adachi, T., Berg, G. P. A., et al. 2016, Phys. Rev. C, 93, 055803

Terndrup, D. M., Pinsonneault, M., Jeffries, R. D., et al. 2002, ApJ, 576, 950

Teske, J. K., Cunha, K., Schuler, S. C., Griffith, C. A., & Smith, V. V. 2013, ApJ, 778, 132

The, L.-S., El Eid, M. F., & Meyer, B. S. 2007, ApJ, 655, 1058

Travaglio, C., Galli, D., Gallino, R., et al. 1999, ApJ, 521, 691

Travaglio, C., Hillebrandt, W., & Reinecke, M. 2005, A&A, 443, 1007

Tsantaki, M., Santos, N. C., Sousa, S. G., et al. 2019, MNRAS, 485, 2772

Tsantaki, M., Sousa, S. G., Adibekyan, V. Z., et al. 2013, A&A, 555, A150

Turner, D. G. 2012, Astronomische Nachrichten, 333, 174

Turrini, D., Codella, C., Danielski, C., et al. 2021, arXiv e-prints, arXiv:2108.11869

Unsöld, A. 1932, ZAp, 4, 339

Valenti, J. A. & Fischer, D. A. 2005, ApJS, 159, 141

van Leeuwen, F. 2009, A&A, 497, 209

Velichko, A. B., Mashonkina, L. I., & Nilsson, H. 2010, Astronomy Letters, 36, 664

Venuti, L., Prisinzano, L., Sacco, G. G., et al. 2018, A&A, 609, A10

Vescovi, D., Cristallo, S., Busso, M., & Liu, N. 2020, ApJ, 897, L25

Viana Almeida, P., Santos, N. C., Melo, C., et al. 2009, A&A, 501, 965

Vidotto, A. A., Gregory, S. G., Jardine, M., et al. 2014, MNRAS, 441, 2361

Wanajo, S., Janka, H.-T., & Müller, B. 2011, ApJ, 726, L15

West, A. A., Weisenburger, K. L., Irwin, J., et al. 2015, ApJ, 812, 3

Woosley, S. E. & Weaver, T. A. 1995, ApJS, 101, 181

Wright, N. J., Drake, J. J., Mamajek, E. E., & Henry, G. W. 2011, ApJ, 743, 48

Yana Galarza, J., Meléndez, J., Lorenzo-Oliveira, D., et al. 2019, MNRAS, 490, L86

Yong, D., Carney, B. W., & Friel, E. D. 2012, AJ, 144, 95

Yong, D., Lambert, D. L., Allende Prieto, C., & Paulson, D. B. 2004, ApJ, 603, 697

Zacharias, N., Monet, D. G., Levine, S. E., et al. 2004, in American Astronomical Society Meeting Abstracts, Vol. 205, American Astronomical Society Meeting Abstracts, 48.15

Zhao, G., Mashonkina, L., Yan, H. L., et al. 2016, ApJ, 833, 225